FUNCTIONAL STUDIES OF THE HUMAN 25-HYDROXYVITAMIN D_3- 24-HYDROXYLASE, CYP24A1

BY

Martin John Kaufmann

A thesis submitted to the Department of Biochemistry in conformity
with the requirements for the degree of
Doctor of Philosophy

Queen's University
May 2010

ABSTRACT

This thesis focuses on the cytochrome P450 CYP24A1, which catabolizes 1α,25-dihydroxyvitamin D_3 (1α,25-$(OH)_2D_3$) via two pathways commencing with C24-, or C23-hydroxylation and culminating in calcitroic acid or 1α,25-$(OH)_2D_3$-26,23-lactone respectively. In my thesis, I set out to identify the molecular determinants of the unique multicatalytic activity of human (h) CYP24A1, using a combination of techniques including homology modeling, site-directed mutagenesis and enzyme activity assays. In total, 42 hCYP24A1 mutants were stably transfected into V79-4 cells, and the metabolism of 1α,25-$(OH)_2D_3$ and 9 analogs or prodrugs were studied using HPLC and LC-MS-based techniques. Overall, we observed that mutations at sites in contact with the side-chain of 1α,25-$(OH)_2D_3$ above the heme in the homology model, affected the regioselectivity of the protein, and mutations at more distal sites along the substrate cavity affected the access of the substrate or intermediates. Of these mutations, A326G and V391L were of particular interest. Ala326, in the centre of the I-helix in contact with the side chain of 1α,25-$(OH)_2D_3$, is a major determinant of the regioselectivity difference between opossum (C23-hydroxylating) and human (C24-hydroxylating) enzymes. When Ala326 was mutated to Gly, as it is in opossum, hCYP24A1 was converted from a C24-hydroxylase, to a C23-hydroxylase, forming 1α,25-$(OH)_2D_3$-26,23-lactone. We propose that A326G permits the side chain to enter the substrate binding site more deeply, thus positioning C23 as opposed to C24 above the heme for hydroxylation. Another mutation, V391L in the β3a sheet, drastically changed the substrate specificity of CYP24A1 towards the prodrug 1α-hydroxyvitamin D_3 (1α-OH-D_3), which is not metabolized by the wild-type enzyme. V391L converted hCYP24A1 into a 1α-OH-D_3-25-hydroxylase, forming 1α,25-$(OH)_2D_3$ which was subsequently catabolized via C24-hydroxylation by the same enzyme. The downstream catabolism of 1α,25-$(OH)_2D_3$ formed from 1α-OH-D_3 was engineered to proceed via C23-hydroxylation, by introducing a V391L/A326G double mutant. We propose that altered steric contact at C21 is responsible for enabling C25-hydroxylation by V391L. Taken together, we have successfully developed an approach that has identified key structural and functional insights into the mechanism of action of hCYP24A1 that can be potentially applied to study other cytochrome P450 enzymes.

CO-AUTHORSHIP

The data that I present in this thesis focuses on my attempts to identify the molecular determinants of human CYP24A1 activity. My work includes contributing to the selection of some of the CYP24A1 mutants, design and generation of many of the expression constructs and, generation of a stable cell expression system that I used to express 42 CYP24A1 mutants. I characterized the effect of all 42 mutations on the catabolism of 1α,25-$(OH)_2D_3$, and selected up to 20 mutants to study the metabolism of up to 9 analogs or prodrugs of 1α,25-$(OH)_2D_3$, using HPLC and LC-MS. The multi-sequence alignment, homology modeling/substrate docking, as well as the site directed mutagenesis was conducted by Dr. David Prosser, Post Doctoral Fellow, Department of Biochemistry, Queen's University. Research technicians Ms. Valarie Byford and Ms. Shelly West conducted the sodium periodate cleavage analysis of the metabolites 1α,24,25-$(OH)_3D_3$, and 1α,23,25-$(OH)_3D_3$, and the real time PCR analysis of cyp24a1 mRNA analysis respectively.

.

ACKNOWLEDGEMENTS

I would like to thank my family, Janice, Erich, Debbie & Michael Kaufmann, and Paul Offinga for their love and support throughout my time at university.

I would like to thank my supervisor, Dr. Glenville Jones for his dedicated scientific guidance, without which this work could not have been possible. I would also like to thank Dr. Jones for giving me numerous opportunities to participate in research activities outside of the laboratory, in the form of attending academic conferences and pursuing collaborations with other investigators. My main collaborator on this project, Dr. David Prosser, I thank for sharing his insights on the structure of CYP24A1 and for engaging me in many intriguing scientific conversations over the years. Ms. Valarie Byford was especially integral to my technical development in the laboratory, in addition to providing a friendly and interactive workplace. Ms. Shelly West, in addition to providing technical support also contributed to a fun and interactive atmosphere that has been a pleasure to take part in.

I would also like to acknowledge the support of my collaborators, Drs. P.H. Jellinck, and Poh-Gek Forkert for giving me the opportunity to work on their stimulating research projects, as well as the contributions of former laboratory members, Drs. Sonoko Masuda, James Chithalen, and Yu-Ding Guo, to my scientific development in the laboratory.

TABLE OF CONTENTS

ABSTRACT ii

CO-AUTHORSHIP iii

ACKNOWLEDGEMENTS iv

LIST OF FIGURES viii

LIST OF TABLES x

LIST OF ABBREVIATIONS vii

CHAPTER 1: INTRODUCTION & LITERATURE REVIEW

1.1 Overview 1

1.2 Vitamin D: Activation, mechanism of action, and role in human health 1

1.3 Role of CYP24A1 in vitamin D metabolism 8

1.4 Vitamin D Analogs 11

1.5 Cytochrome P450 structure and function 14

1.6 Thesis objectives 17

CHAPTER 2: MATERIALS AND METHODS

2.1 Cell culture 19

2.2 Preparation of pcDNA5/FRT-based CYP24A1 expression constructs 20

2.3 Transfection of V79-4 cells with pFRT-*lac*Zeo 22

2.4 β-galactosidase assay 24

2.5 Southern blot analysis 25

2.6 Transfection of pFRT/*lac*Zeo-containing V79-4 cells with pcDNA5/FRT-CYP24A1 28

2.7 Incubation of CYP24A1-expressing cells with vitamin D substrates 30

2.8 Extraction of vitamin D metabolites 31

2.9 High performance liquid chromatography 33

2.10 Sodium periodate cleavage and high performance liquid chromatography-mass spectrometry 34

2.11 Mathematical and statistical treatment of data 36

CHAPTER 3: Ala326 IS A CRITICAL DETERMINANT OF CYP24A1 REGIOSELECTIVITY

3.1 Introduction 39

3.2 Results 40

3.2.1 Catabolism of 1α,25-$(OH)_2D_3$ and 25-OH-D_3 in cultured cell models of CYP24A1 40

3.2.2 Catabolism of 1α,25-$(OH)_2D_3$ and 25-OH-D_3 by Ala326Gly-modified CYP24A1 42

3.2.3 Characterization of the catabolites of 1α,25-$(OH)_2D_3$ and 25-OH-D_3 49

3.3 Summary 56

CHAPTER 4: MUTAGENESIS AND ACTIVITY STUDIES OF THE SUBSTRATE-BINDING POCKET OF CYP24A1

4.1 Introduction 60

4.2 Results 62

4.2.1 Catabolism of 1α,25-$(OH)_2D_3$ by Leu148-modified CYP24A1 62

4.2.2 Catabolism of 1α,25-$(OH)_2D_3$ by Ile131-modified CYP24A1 67

4.2.3 Catabolism of 1α,25-$(OH)_2D_3$ by M246L-modified CYP24A1 71

4.2.4 Catabolism of 1α,25-$(OH)_2D_3$ by Met252- and Met253-modified CYP24A1 74

4.2.5 Catabolism of 1α,25-$(OH)_2D_3$ by Ser390-, Val391- and Met416-modified CYP24A1 79

4.3 Summary 82

CHAPTER 5: METABOLISM OF PRODRUGS AND ANALOGS OF 1α,25-$(OH)_2D_3$ BY SELECTED CYP24A1 MUTANTS

5.1 Introduction 89

5.2 Results 90

5.2.1 Metabolism of 25-OH-D_3 and 1α-OH-D_3 by selected CYP24A1 mutants 90

5.2.2 Metabolism of 1α,25-$(OH)_2D_3$ and 1α-OH-D_2 by selected CYP24A1 mutants 95

5.2.3 Metabolism of 1α,25-$(OH)_2DHT_3$ and 1α-OH-DHT_3 by selected CYP24A1 mutants 114

5.3 Summary 115

CHAPTER 6: DISCUSSION

6.1 Lessons learned from mutagenesis and activity studies of hCYP24A1 119

6.2 The crystal structure of rCYP24A1 122

6.3 The mechanism of action of CYP24A1 132

6.4 Physiological implications and strategies for vitamin D analog design 134

REFERENCES 139

APPENDIX 157

A4.2.6 Catabolism of 1α,25-$(OH)_2D_3$ by Gly499- and Leu501-modified CYP24A1 175

A5.2.4 Metabolism of 20-CH_3-1α,25-$(OH)_2D_3$, 20-epi-1α,25-$(OH)_2D_3$, and 16-ene-1α,25-$(OH)_2D_3$ by selected CYP24A1 mutants 181

LIST OF FIGURES

Figure 1.1 Activation of vitamin D_3 to 1α,25-$(OH)_2D_3$ 5

Figure 1.2 Current understanding of the activation, mechanism of action, and catabolism of vitamin D 6

Figure 1.3 Catabolism 1α,25-$(OH)_2D_3$ by CYP24A1 10

Figure 2.1 Overview of the Flp-In transfection method 22

Figure 2.2 Screening of zeocin-resistant foci by β-galactosidase and Southern blot assays 29

Figure 2.3 Selected vitamin D substrates 32

Figure 3.1 Comparative metabolism of 1α,25-$(OH)_2D_3$ in V79-CYP24, OK, and transiently transfected V79-4 cells 45

Figure 3.2 Comparative metabolism of 25-OH-D_3 in V79-CYP24, OK, and transiently transfected V79-4 cells 46

Figure 3.3 Comparative metabolism of 1α,25-$(OH)_2D_3$ in V79-4 cells stably transfected with wild-type or A326G-modified hCYP24A1 51

Figure 3.4 Substrate concentration-dependent distribution of the products of 1α,25-$(OH)_2D_3$ 53

Figure 3.5 Multi-sequence alignment and homology modeling analysis of wild-type and A326G-modified hCYP24A1 54

Figure 3.6 LC-MS-based characterization of the products of 1α,25-$(OH)_2D_3$ in CYP24A1-tranfected cells 57

Figure 3.7 LC-MS, LC-MS/MS and sodium periodate cleavage analysis of the putative metabolites 1α,24*R*,25-$(OH)_3D_3$, and 1α,23*S*,25-$(OH)_3D_3$ 59

Figure 4.1 1α,25-$(OH)_2D_3$-docked homology model of human CYP24A1 61

Figure 4.2 HPLC analysis of the metabolism of 1α,25-$(OH)_2D_3$ by L148A-modified CYP24A1 65

Figure 4.3 HPLC analysis of the metabolism of 1α,25-$(OH)_2D_3$ by L148F-modified CYP24A1 66

Figure 4.4 HPLC analysis of the metabolism of 1α,25-$(OH)_2D_3$ by I131A-modified CYP24A1 69

Figure 4.5 HPLC analysis of the metabolism of 1α,25-$(OH)_2D_3$ by I131F-modified CYP24A1 70

Figure 4.6 HPLC analysis of the metabolism of 1α,25-$(OH)_2D_3$ by M246L-modified CYP24A1 73

Figure 4.7 HPLC analysis of the metabolism of 1α,25-$(OH)_2D_3$ by M252L-modified CYP24A1 77

Figure 4.8 HPLC analysis of the metabolism of 1α,25-$(OH)_2D_3$ by M252T- and M2523T-modified CYP24A1 78

Figure 4.9 HPLC analysis of the metabolism of 1α,25-$(OH)_2D_3$ by S390G- modified CYP24A1 85

Figure 4.10 HPLC analysis of the metabolism of 1α,25-$(OH)_2D_3$ by V391L- modified CYP24A1 86

Figure 4.11 HPLC analysis of the metabolism of 1α,25-$(OH)_2D_3$ by M416T- modified CYP24A1 87

Figure 5.1 HPLC analysis of the metabolism of 1α,25-$(OH)_2D_3$ and 25-OH-D_3 by selected CYP24A1 mutants 96

Figure 5.2 HPLC analysis of the metabolism of 1α,25-$(OH)_2D_3$ and 1α-OH-D_3 by selected CYP24A1 mutants 97

Figure 5.3 Activation and catabolism of the prodrug 1α-OH-D_3 by V391L-modified CYP24A1 101

Figure 5.4 HPLC analysis of the metabolism of 1α,25-$(OH)_2DHT_3$ and 1α-OH-DHT_3 by selected CYP24A1 mutants 104

Figure 5.5 HPLC analysis of the metabolism of 1α,25-$(OH)_2D_3$ and 1α,25-$(OH)_2D_2$ by selected CYP24A1 mutants 109

Figure 5.6 HPLC analysis of the metabolism of 1α,25-$(OH)_2D_3$ and 1α-OH-D_2 by selected CYP24A1 mutants 110

Figure 6.1 Comparison of a rat CYP24A1 crystal structure with the homology model of hCYP24A1 125

Figure A4.1 Distribution of the catabolites of 1α,25-$(OH)_2D_3$ formed by Leu148 mutants 162

Figure A4.2 Distribution of the catabolites of 1α,25-$(OH)_2D_3$ formed by Ile131 mutants 165

Figure A4.3 Distribution of the catabolites of 1α,25-$(OH)_2D_3$ formed by M246L and M416T mutants 167

Figure A4.4 Distribution of the catabolites of 1α,25-$(OH)_2D_3$ formed by Met252 and Met253 mutants 170

Figure A4.5 Distribution of the catabolites of 1α,25-$(OH)_2D_3$ formed by S390G and V391L mutants 172

Figure A4.6 HPLC analysis of the metabolism of 1α,25-$(OH)_2D_3$ by G499V-modified CYP24A1 177

Figure A4.7 HPLC analysis of the metabolism of 1α,25-$(OH)_2D_3$ by L501I-modified CYP24A1 178

Figure A4.8 HPLC analysis of the metabolism of 1α,25-$(OH)_2D_3$ by L501V-modified CYP24A1 179

Figure A4.9 Distribution of the catabolites of 1α,25-$(OH)_2D_3$ formed by G499V and Leu501 mutants 181

Figure A5.1 HPLC analysis of the metabolism of 1α,25-$(OH)_2D_3$ and 20-CH_3-1α,25-$(OH)_2D_3$ by selected CYP24A1 mutants 184

Figure A5.2 HPLC analysis of the metabolism of 1α,25-$(OH)_2D_3$ and 20-epi-1α,25-$(OH)_2D_3$ by selected CYP24A1 mutants 185

Figure A5.3 HPLC analysis of the metabolism of 1α,25-$(OH)_2D_3$ and Δ^{16}-1α,25-$(OH)_2D_3$ by selected CYP24A1 mutants 189

LIST OF TABLES

Table 3.1 Regioselectivity differences in CYP24A1-containing cells 45

Table 3.2 Quantitative analysis of the metabolism of 1α,25-$(OH)_2D_3$ by wild-type and A326G-modified hCYP24A1 50

Table 3.3 Characterization of the products of 1α,25-$(OH)_2D_3$ and 25-OH-D_3 56

Table 4.1 Summary of the mutations made to the substrate binding pocket of hCYP24A1 88

Table 5.1 Quantitative comparison of the metabolism of 1α,25-$(OH)_2D_3$, 25-OH-D_3 and 1α-OH-D_3 by selected CYP24A1 mutants 96

Table 5.2 Quantitative comparison of the metabolism of 1α,25-$(OH)_2D_3$, 1α-OH-D_3, 1α,25-$(OH)_2D_2$, 1α-OH-D_3 and 1α,25-$(OH)_2DHT_3$ & 1α-OH-DHT_3 by selected CYP24A1 mutants and CYP27A1. 102

Table 5.3 Quantitative comparison of the metabolism of 1α,25-$(OH)_2D_3$, 1α,25-$(OH)_2D_2$, and 1α-OH-D_2 by selected CYP24A1 mutants 111

Table 5.4 Comparison of the metabolism of 1α,25-$(OH)_2D_3$ and selected analogs or prodrugs by mutant CYP24A1 proteins 117

Table A2.1 Cultured cell models of vitamin D metabolism 157

Table A2.2 Summary of cell lines made, rtPCR and enzyme activity studies 158

Table A2.3 Summary of chromatographic systems used in this thesis 159

Table A2.4 List of optimized mass spectrometer settings 159

Table A4.1 Quantitative analysis of the metabolism of 1α,25-$(OH)_2D_3$ by Leu148-modified hCYP24A1 160

Table A4.2 Quantitative analysis of the metabolism of 1α,25-$(OH)_2D_3$ by Ile131-modified hCYP24A1 163

Table A4.3 Quantitative analysis of the metabolism of 1α,25-$(OH)_2D_3$ by M246L-modified hCYP24A1 166

Table A4.4 Quantitative analysis of the metabolism of 1α,25-$(OH)_2D_3$ by Met252- and Met253-modified hCYP24A1 168

Table A4.5 Quantitative analysis of the metabolism of 1α,25-$(OH)_2D_3$ by S390G-modified hCYP24A1 171

Table A4.6 Quantitative analysis of the metabolism of 1α,25-$(OH)_2D_3$ by V391L-modified hCYP24A1 173

Table A4.7 Quantitative analysis of the metabolism of 1α,25-$(OH)_2D_3$ by M416T-modified hCYP24A1 174

Table A4.8 Quantitative analysis of the metabolism of 1α,25-$(OH)_2D_3$ by G499V- and Leu501-modified hCYP24A1 180

Table A5.1 Quantitative comparison of the metabolism of 1α,25-$(OH)_2D_3$, 20-CH_3-1α,25-$(OH)_2D_3$ and 20-epi-1α,25-$(OH)_2D_3$ by selected CYP24A1 mutants 186

Table A5.2 Quantitative comparison of the metabolism of 1α,25-$(OH)_2D_3$, and Δ^{16}- 1α,25-$(OH)_2D_2$ by selected CYP24A1 mutants 191

LIST OF ABBREVIATIONS

Vitamin D compounds

25-OH-D_3	25-hydroxyvitamin D_3
1α-OH-D_3	1α-hydroxyvitamin D_3
1α,25-$(OH)_2D_3$	1α,25-dihydroxyvitamin D_3
1α-OH-DHT_3	1α-hydroxydihydrotachysterol$_3$
1α,25-$(OH)_2DHT_3$	1α,25-dihydroxydihydrotachysterol$_3$

Analysis of vitamin D metabolites

CID	collision-induced dissociation
ES^+	electrospray positive (mode)
GAA	glacial acetic acid
HIM	hexane/isopropanol/methanol (solvent system)
HPLC	high performance liquid chromatography
GAA	glacial acetic acid
LC-MS	liquid chromatography mass spectrometry
LC-MS/MS	liquid chromatography tandem mass spectrometry
MRM	multiple reaction monitoring
$[M+H]^+$	molecular ion
$[M+H-H_2O]^+$	primary dehydration product
$[M+H-2H_2O]^+$	secondary dehydration product
RT	retention time
PDA	photodiode array (detector / detection)
W/M/GAA	water/methanol/glacial acetic acid (solvent system)
W/A/GAA	water/acetonitrile/glacial acetic acid

General laboratory reagents

ab	antibiotic/antimycotic
amp	ampicillin
BSA	bovine serum albumin
dATP	deoxyadenosine triphosphate
DMEM	Dulbecco's Modified Eagle Medium
DMSO	dimethyl sulphoxide
DPPD	1,2-dianilinoethane (antioxidant)
EDTA	ethylenediaminitetraacetic acid
FBS	fetal bovine serum
LB	Luria Bertani (medium and plates)
MEM	minimum essential medium
ONPG	orthonitrophenol-β-D-galactopyranoside
PBS	phosphate buffered saline
PVP	polyvinylpyrolidone
SDS	sodium dodecyl sulphate
SOB	super optimal broth
SOC	super optimal broth with catabolite repression
SSC	sodium chloride/sodium citrate (buffer)
SSPE	sodium chloride/sodium phosphate/EDTA (buffer)
TAE	tris/acetate/EDTA buffer
TCA	trichloroacetic acid

Other

ATCC	American Type Culture Collection
CPM	counts per minute
DBP	vitamin D-binding protein
DRIP	vitamin D receptor-interacting protein
FAD	flavin adenine dinucleotide
FGF23	fibroblast growth factor 23
FMN	flavin adenine mononucleotide
FRT	Flp recombinase target
OD	optical density
OK	opossum kidney (cells)
PTC	proximal tubule cell
PTH	parathyroid hormone
RMSD	root mean squared deviation
rtPCR	real time polymerase chain reaction
RXR	retinoid X receptor
SNP	single nucleotide polymorphism
SRS	substrate recognition sites
TNF	tumor necrosis factor
VDR	vitamin D receptor
VDRE	vitamin D responsive element
UV	ultraviolet

CHAPTER 1: INTRODUCTION AND LITERATURE REVIEW

1.1 OVERVIEW

Vitamin D_3 is a lipid-soluble seco-steroid acquired via ultraviolet light-induced synthesis in the skin or from dietary sources [1-3]. Vitamin D_3 was originally discovered by Mellanby in 1920 as a factor abundant in cod liver oil that could prevent rickets in dogs [4]. Many years passed until it was recognized that vitamin D_3 undergoes two successive hydroxylations at C-25 and C-1, forming the metabolite 1α,25-dihydroxyvitamin D_3 (1α,25-$(OH)_2D_3$), which carries out the biological functions attributed to vitamin D_3 [5]. In the late 1960s, the discovery of the vitamin D receptor (VDR) confirmed that 1α,25-$(OH)_2D_3$ could carry out its biological actions via a genomic mechanism [6-8]. The broad tissue expression profile of the VDR and the finding that over 300 genes could be regulated by 1α,25-$(OH)_2D_3$ lead to the realization that 1α,25-$(OH)_2D_3$ participates in a wide variety of biological actions, including the differentiation of specialized cell types, in addition to its classical role in calcium/phosphate homeostasis [9]. The clinical potential of 1α,25-$(OH)_2D_3$ has been investigated extensively by the generation of a myriad vitamin D analogs in an attempt to alter the potency and specificity of function relative to the parent compound 1α,25-$(OH)_2D_3$. In addition, these analogs serve as important probes to study the structure/function relationships in VDR-mediated signal transduction, as well as the cytochrome P450-mediated activation of vitamin D_3 and degradation of 1α,25-$(OH)_2D_3$ [10]. Originally, the kidney was believed to be the major site of 1α,25-$(OH)_2D_3$ production, however it is now recognized that many other sites can generate 1α,25-$(OH)_2D_3$ from its precursor 25-hydroxyvitamin D_3 (25-OH-D_3), thus regulating the vitamin D biological signal in a paracrine/autocrine manner [11]. Recent epidemiological and interventional studies have revealed an inverse relationship between vitamin D deficiency and the incidence/progression of serious diseases including certain cancers and autoimmune conditions, which have emphasized the importance of adequate vitamin D intakes [11,12].

1.2 VITAMIN D: ACTIVATION, MECHANISM OF ACTION, AND ROLE IN HUMAN HEALTH

The first step in the activation of vitamin D_3, 25-hydroxylation, is believed to be catalyzed in the liver by the mitochondrial P450 CYP27A1, and the microsomal enzyme CYP2R1 [13] (Figure 1.1).

CYP27A1 is a bifunctional enzyme also involved in 27-hydroxylation of cholesterol in bile acid biosynthesis [14]. Even though CYP27A1 was the first of the major vitamin D_3-25-hydroxylases to be cloned and characterized [15,16], evidence accumulated over the years suggesting that CYP27A1 may not be the only physiological vitamin D_3-25-hydroxylase. This evidence includes: (1) The detection *in vivo* of the metabolite 25-OH-D_2 upon administration of vitamin D_2, despite contrary *in vitro* studies suggesting that CYP27A1 cannot 25-hydroxylate vitamin D_2, arguing for the presence of another 25-hydroxylase [16]. (2) A perfused rat liver model of 25-hydroxylation revealed kinetics consistent with two enzymes, including a low-affinity high-capacity enzyme (CYP27A1), and an unidentified high-affinity low-capacity form, which was presumably more likely to metabolize physiological concentrations of vitamin D_3 [17]. (3) Clinical findings among patients with the inherited cholesterol metabolism disorder, cerebrotendenous xanthomatosis, in which CYP27A1 is mutated do not exhibit major differences in circulating 25-OH-D_3 levels [18], which supported more recent results from the CYP27A1 knockout mouse that demonstrated a clear role for this enzyme in cholesterol metabolism - but did not result in altered levels of vitamin D metabolites [19,20]. In 2003, Mangelsdorf and Russell identified microsomal CYP2R1 as a vitamin D_3- & D_2-25-hydroxylase and exhibited similar properties as the elusive 'microsomal 25-hydroxylase' first proposed over 30 years earlier [21,22]. CYP2R1 is likely to be an important physiological enzyme since a dysfunctional CYP2R1 has been shown to cause vitamin D-dependent rickets, and does not exhibit any sex and species differences unlike several other candidate 25-hydroxylases.

The metabolite 25-OH-D_3, is the major circulating form of vitamin D (25-200nM [23]) due it its relatively high binding affinity to the DBP when compared to other vitamin D metabolites (5×10^8 M[24,25]), and its circulating concentration is the accepted nutritional indicator of vitamin D status [12]. The second activation step: 1α-hydroxylation, is catalyzed by CYP27B1 in the proximal tubule cells (PTCs) of the kidney [26-28]. It was originally thought that the unbound free form of 25-OH-D_3 diffused across the cell membrane to gain access to the PTCs from the glomerular filtrate [29,30]. However, the vast excess of circulating DBP (only 2-5% is bound to 25-OH-D_3 [31]) and the high DBP binding affinity of 25-OH-D_3, leaving only 0.003% in the 'free' form, argued for the presence of an additional transport mechanism to explain estimates of the daily conversion of 25-OH-D_3 to 1α,25-$(OH)_2D_3$ [32]. Eventually, the endocytic receptors megalin and cubilin were implicated in the endocytosis of DBP-25-OH-D_3

complexes which are degraded by lysosomes [33-35]. The released 25-OH-D_3 becomes 1α-hydroxylated by CYP27B1 to form the active hormone 1α-25-$(OH)_2D_3$ (Figure 1.1, 1.2). Unlike CYP2R1 and CYP27A1 which are not tightly regulated by vitamin D metabolites, CYP27B1 is downregulated by its product, 1α,25-$(OH)_2D_3$ [36]. The importance of CYP27B1 in the formation of 1α,25-$(OH)_2D_3$ was demonstrated with a CYP27B1 knockout mouse, which possessed a similar phenotype to patients with vitamin D-dependent rickets type I, a rare form of rickets caused by inactivating mutations to CYP27B1 [27,37-40], characterized by undetectable serum 1α,25-$(OH)_2D_3$, hypocalcemia, and the bone mineralization defects rickets and osteomalacia [41-43].

The metabolite 1α,25-$(OH)_2D_3$, carries out the functions attributed to vitamin D by binding to the nuclear VDR in target tissues (Figure 1.2). Tight association of 1α,25-$(OH)_2D_3$ with the VDR results in (1) enhanced dimerization with the retinoid X receptor (RXR) (2) enables phosphorylation of the VDR, and (3) alters the conformation of the AF/2 domain to 'close' the ligand binding domain of the VDR resulting in the dissociation of a co-repressor/ histone deacetylase complex. The VDR/RXR heterodimer is able to recognize and bind to a specific vitamin D responsive element (VDRE) on the promoter of vitamin D-dependent genes [9,44,45]. The consensus VDRE comprises a direct hexameric repeat of AGGTCA separated by a 3-nucleotide spacer. A host of transcriptional coactivators including SRC-1, CBP/p300, receptor coactivator-63 (NCoA-62) bind the VDR/RXR heterodimer and promote histone acetylation. The coactivators SRC-1 and CBP/p300 become autoacetylated and dissociate from the complex. This enables the recruitment of a transcriptional mediator complex including the vitamin D receptor interacting protein (DRIP)-205 which binds to the AF/2 domains of the VDR/RXR heterodimer. The mediator complex delivers TFIIB to RNA polymerase II resulting in the expression of the vitamin D-dependent gene. Over 300 genes have been identified to be directly or indirectly regulated by 1α,25-$(OH)_2D_3$ including those involved in calcium/phosphate homeostasis, cell differentiation & proliferation, regulation of the immune system, and regulation of the cardiovascular system. The diverse range of actions of 1α,25-$(OH)_2D_3$ support the almost ubiquitous expression of the VDR [9,44,45].

In response to low plasma calcium levels, the calcium-sensing receptor (CaSR) in the parathyroid gland controls the secretion of parathyroid hormone (PTH) which upregulates renal CYP27B1 via a cyclic AMP/phosphatidyl inositol 4,5-bisphosphate mechanism, resulting in the enhanced production of 1α,25-

$(OH)_2D_3$. The hormone 1α,25-$(OH)_2D_3$ upregulates the calcium channels TRPV5 and TRPV6, as well as the intracellular transport calbindin proteins in the kidney and intestine, resulting in the renal reabsorption, and intestinal uptake of calcium from the diet [9,44,46]. 1α,25-$(OH)_2D_3$ also stimulates indirectly, the differentiation of bone-resorbing pre-osteoclasts into osteoclasts through the expression of RANK-ligand, as a means to increase plasma calcium levels. Negative feedback regulation occurs via the downregulation of CYP27B1 by 1α,25-$(OH)_2D_3$, inhibition of PTH synthesis via the calcium sensing receptor, and via the secretion of calcitonin from the CT cells of the thyroid gland to halt calcium mobilization from the skeleton. Intestinal phosphate absorption, and renal phosphate reabsorption are stimulated by 1α,25-$(OH)_2D_3$ via regulation of genes such as the sodium/phosphate co-transporter proteins. Low phosphate levels can upregulate CYP27B1 independently of calcium. Phosphate homeostasis is negatively regulated by fibroblast growth factor 23 (FGF-23) in the bone in response to 1α,25-$(OH)_2D_3$. FGF23 expression by osteocytes results in (1) downregulation of the renal sodium phosphate cotransporter resulting in phosphate loss in the urine (2) downregulation of 1α,25-$(OH)_2D_3$ synthesis via CYP27B1, and (3) upregulation of CYP24A1 expression, which catabolizes 1α,25-$(OH)_2D_3$ [9,44,46,47].

One of the first pieces of evidence that vitamin D could have potentially important roles outside of calcium/phosphate homeostasis, was the observation that 1α,25-$(OH)_2D_3$ could induce the differentiation of myeloid leukemia cells to macrophages, and highlighted the potential importance of 1α,25-$(OH)_2D_3$ (and analogs) to treat hyperproliferative disorders [48,49]. The anti-cancer effects of 1α,25-$(OH)_2D_3$ have since been reported in several *in vitro* and *in vivo* cancer models involving the prostate [50,51], breast [52,53] colon [54,55], and leukemia [56,57]. One mechanism involved in the anticancer effects of 1α,25-$(OH)_2D_3$ is the arrest of the cell cycle at the G_0-G_1 transition. 1α,25-$(OH)_2D_3$ has been shown to upregulate p21 and p27 cyclin-dependent kinase inhibitors, resulting in the dephosphorylation of the retinoblastoma protein which inhibits the transcription of E2F required for cell cycle progression [58,59]. Other mechanisms of cell cycle arrest, involve the upregulation of HOXA10 [60], and by regulating the dephosphorylation of p70S6 kinase, implicated in arresting the G_1-S phase transition in breast and colon cancer cells respectively [61]. Alteration to growth factor signaling is another route whereby 1α,25-$(OH)_2D_3$ and its analogs have been observed to inhibit cell growth [62]. Several mechanisms whereby 1α,25-$(OH)_2D_3$ can induce apoptosis in cancer cells have been identified, and include (1) modulation of the relative amounts of anti-

Figure 1.1: Activation of vitamin D_3 to 1α,25-$(OH)_2D_3$. At least three cytochrome P450-containing enzymes are believed to be involved in the activation of vitamin D_3. Even though CYP27A1 was the first major hepatic vitamin D_3-25-hydroxylase to be cloned and characterized, it is now widely accepted that CYP2R1 is more likely to be the major physiological vitamin D_3-25-hydroxylase due to its high-affinity, low-capacity kinetic properties [13,63]. Furthermore, an inactivating L99P mutation in CYP2R1 has been linked to a form of rickets, although this has yet to be confirmed in a CYP2R1 knockout mouse model [21]. Taken together with the kinetic studies, the L99P mutation in CYP2R1 is the only inactivating mutation of a vitamin D_3-25-hydroxylase linked to rickets, suggesting that CYP2R1 plays a major physiological role. Other enzymes possessing vitamin D_3-25-hydroxylases have been identified including CYP2C11, CYP3A4, CYP2D11, CYP2D25, CYP2J2 and CYP2J3, however these enzymes may not be physiologically significant vitamin D_3-25-hydroxylases for a variety of reasons including broad substrate specificity, low vitamin D_3 binding affinity, and species & expression patterns inconsistent with the 25-OH-D_3 requirements of the animal. The renal enzyme CYP27B1, is the only enzyme known 1α-hydroxylate 25-OH-D_3, forming the biologically-active metabolite, 1α,25-$(OH)_2D_3$. Extra-renal sites of CYP27B1 expression have also been identified [13].

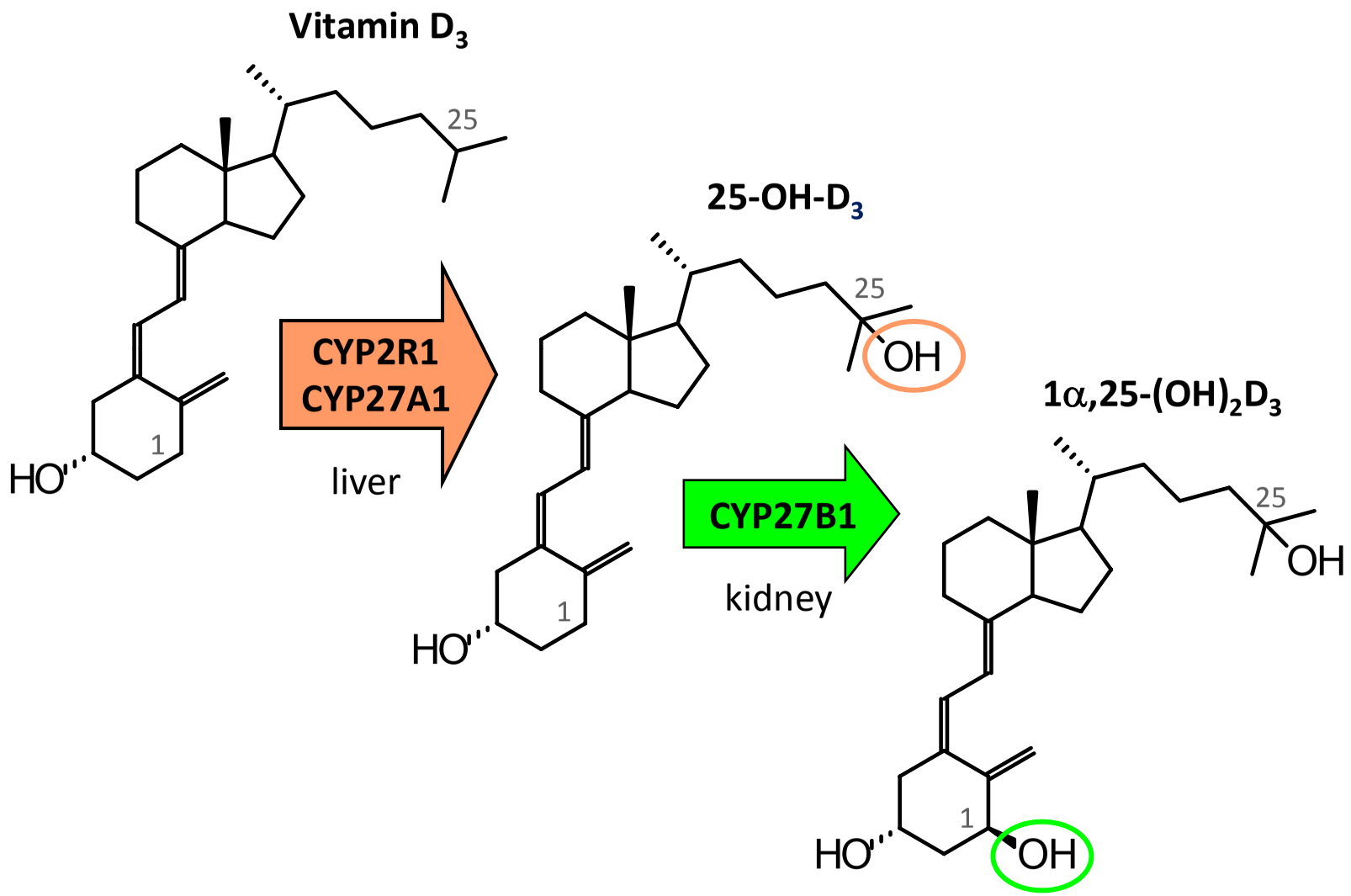
Vitamin D3
25
1
HO
CYP2R1
CYP27A1
liver
25-OH-D3
25
OH
1
HO
CYP27B1
kidney
1α,25-(OH)2D3
25
OH
1
HO
OH

Figure 1.2: Current understanding of the activation, mechanism of action, and catabolism of vitamin D. Several key proteins are involved in the mechanism of action of vitamin D including the plasma vitamin D-binding protein (DBP), the enzymes involved in the activation of vitamin D_3 (CYP2R1 and CYP27A1), the genomic signal transduction cascade (VDR, RXR, coactivators), as well as a self-regulating catabolic enzyme (CYP24A1). A model of a hepatocyte (top left) depicts the major site of 25-hydroxylation of vitamin D_3, catalyzed by mitochondrial CYP27A1 and microsomal CYP2R1. The metabolite 25-OH-D_3 is the most abundant DBP-bound circulating form of vitamin D, and is widely accepted as the major nutritional indicator of vitamin D status. In the proximal tubule cells of the kidney (top right), the cell surface receptors megalin and cubilin mediate the endocytosis of DBP-bound 25-OH-D_3, where CYP27B1 catalyzes the formation of the active form, 1α,25-$(OH)_2D_3$. It is believed that the free, unbound fraction of 1α,25-$(OH)_2D_3$ diffuses across the target cell membrane (bottom right), where it is able to activate a genomic response upon binding the VDR which forms a heterodimer with RXR leading to a complex sequence of events culminating in the upregulation of vitamin D-dependent genes containing specific VDREs. Examples of genes containing VDREs include the cell cycle regulator p21, the bone matrix protein osteopontin, as well as the cytochrome P450 CYP24A1 which catalyzes the catabolism of 1α,25-$(OH)_2D_3$. Extra-renal 1α-hydroxylating target cells (bottom left) containing CYP27B1 and megalin/cubilin are able to access the circulating pool of 25-OH-D_3 to locally produce and utilize1α,25-$(OH)_2D_3$ via a similar genomic mechanism described for a typical target cells. Reproduced with permission of the author [64].

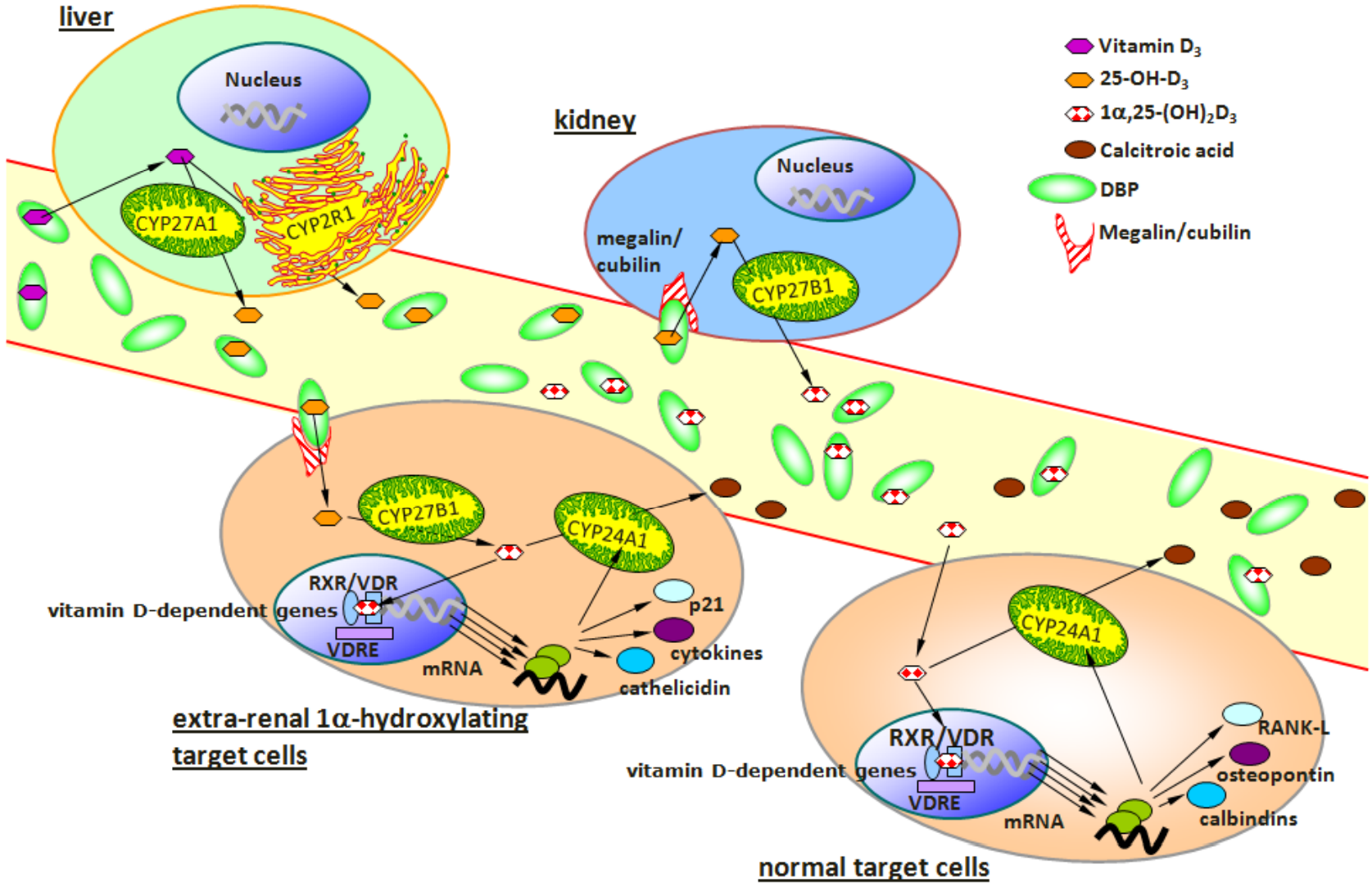
liver
Nucleus
CYP27A1
CYP2R1
kidney
Nucleus
megalin/
cubilin
CYP27B1
Vitamin D3
25-OH-D3
1α,25-(OH)2D3
Calcitroic acid
DBP
Megalin/cubilin
CYP27B1
CYP24A1
RXR/VDR
vitamin D-dependent genes
VDRE
mRNA
p21
cytokines
cathelicidin
extra-renal 1α-hydroxylating
target cells
CYP24A1
RXR/VDR
vitamin D-dependent genes
VDRE
mRNA
RANK-L
osteopontin
calbindins
normal target cells

6a

apoptotic Bcl2 and proapoptotic Bax [65,66] (2) the activation of proapoptotic μ-calpain by increasing the cellular calcium concentration [67](3) and by interacting with other signaling pathways that may lead to apoptosis, including via IGF and TNF [68,69]. Results obtained from the VDR knockout mouse, suggest that 1α,25-$(OH)_2D_3$ could play a role in the differentiation of specialized cell types. For example, keratinocytes from the VDR knockout animals exhibited uncontrolled hyperplasia, and a reduction in the expression of the keratinocyte differentiation markers involucrin and loricin, and were more prone to carcinogen-induced tumorigenesis when compared to the wild-type animals [70-72]. Markers of terminal ketatinocyte differentiation were also reduced in the CYP27B1 knockout animals, implying a role for 1α,25-$(OH)_2D_3$ in keratinocyte differentiation [73]. Similarly, ras-transformed keratinocytes (HPK1A-ras) lacking CYP27B1 *in vitro*, did not respond to treatment with 25-OH-D_3 in terms of growth inhibition and an increase in differentiation markers [74]. Tumors produced from HPK1A-ras cells injected into nude mice, did not respond to 25-OH-D_3 treatment when CYP27B1 was ablated, which highlights the importance of locally-produced 1α,25-$(OH)_2D_3$ in the autocrine/paracrine regulation of keratinocyte proliferation and differentiation [74]. Many other cell types including the breast, prostate, colon, macrophage, and smooth muscle cells are now recognized to express CYP27B1 [11,75]. The number of tissues observed to contain CYP27B1, as well as megalin & cubilin emphasize the growing number of tissues able to access the circulating pool of 25-OH-D_3 and convert it to biologically-active 1α,25-$(OH)_2D_3$.

The active vitamin D metabolite has also been implicated as an important modulator of the immune system. The differentiation and maturation of dendritic cells are inhibited by 1α,25-$(OH)_2D_3$ and analogs, and exhibit reduced CD40, CD80 and CD86 expression [76]. The production of cytokines IL2 and TGF-B1 are regulated by 1α,25-$(OH)_2D_3$, in addition to enhanced immunoglobin synthesis has been reported in activated T cells [77,78]. It is well established that 1α,25-$(OH)_2D_3$ can induce the differentiation of monocytes to macrophages, however an important reason for the observation that macrophages can produce 1α,25-$(OH)_2D_3$ from 25-OH-D_3 has only recently been uncovered [79]. When infected with tuberculosis, toll-like receptors respond to enhance the expression of the VDR and CYP27B1 enabling the production of 1α,25-$(OH)_2D_3$, and the subsequent VDR-dependent expression of antimicrobial cathelicidin, which kills tuberculosis [80,81]. With respect to the cardiovascular system, 1α,25-$(OH)_2D_3$ has been shown to be an important anti-hypertensive agent, in part via decreasing renin production [82]. 1α,25-

$(OH)_2D_3$ has also been proposed to contribute to reduced risk of atherosclerosis and congestive heart failure by reducing the proliferation of myocardial and smooth muscle cells [83]. Studies have also revealed that ultraviolet B-induced increases in 25-OH-D_3 levels (>80 nM) resulted in decreases in low-density lipoprotein levels and increased high-density lipoprotein levels [84], and the chance of myocardial events was 53-80% greater among participants with low circulating levels of 25-OH-D_3 (<55 nM) [11,85].

Recent epidemiological evidence has linked the risk of acquiring and dying from breast, colon and prostate cancer (among others) with vitamin D deficiency, as well as the risk of vitamin D deficiency by living in regions of higher latitude [11,86-89]. Similar associations have been made with autoimmune disorders including type I diabetes, Crohns's disease, multiple sclerosis and rheumatoid arthritis, which emphasize the diverse role of vitamin D in many pathological states, however the molecular bases for these observations are not completely understood [90,91]. Because vitamin D deficiency may not be directly involved in the incidence of a serious illness, or might play a single role in a multifactorial disease, the extraskeletal importance of vitamin D in human health, and the development & modulation of serious illnesses has only recently been recognized via epidemiological and intervention studies. It has been estimated that 1 billion people worldwide are vitamin D deficient or insufficient (<80 nM 25-OH-D_3) due to poor sun exposure (or living in northern latitudes), poor supplementation of foodstuffs, and the poor natural abundance of vitamin D in food sources [12]. The Institute of Medicine is reassessing current recommended daily allowance values in light of these new observations [92].

1.3 THE ROLE OF CYP24A1 IN THE CATABOLISM OF 1α,25-$(OH)_2D_3$

Another VDRE-containing gene encodes the 25-hydroxyvitamin D_3-24-hydroxylase, or CYP24A1, which catalyzes the catabolism of 1α,25-$(OH)_2D_3$ in vitamin D target cells (Figure 1.2, 1.3). The discovery of the 24-hydroxylase activity attributed to CYP24A1, came with the identification of the metabolite 24,25-$(OH)_2D_3$ [93]. Pioneering work using subcellular fractions of the chicken kidney [94], in addition to reconstitution studies using purified enzyme components, revealed that CYP24A1 was a mitochondrial cytochrome P450 [95]. The hypothesis was rapidly emerging that CYP24A1 could play an important role in regulating the inactivation of 1α,25-$(OH)_2D_3$, given that: (1) CYP24A1 expression had been detected in the classical vitamin D target tissues (bone, intestine, kidney)[96], (2) The CYP24A1-

catalyzed product of 1α,25-$(OH)_2D_3$, 1α,24,25-$(OH)_3D_3$, was found to be 10-fold less biologically active than its precursor [97], and (3) 24-hydroxylation of 1α,25-$(OH)_2D_3$ could be induced by 1α,25-$(OH)_2D_3$ itself. The perfused rat kidney was critical in confirming earlier results that 24,25-$(OH)_2D_3$, or 1α,24,25-$(OH)_3D_3$, could be metabolized to products containing 24-oxo and/or 23-hydroxyl groups [98-100], but also revealed that these intermediates could be further metabolized to newly identified truncated products, a 1α,23-alcohol (tetranor-1α,23-$(OH)_2D_3$) and a 1α,23-acid (calcitroic acid) [101,102]. The temporal order of these products, originally established in the perfused rat kidney, led a number of groups to postulate that a 1α,25-$(OH)_2D_3$-inducible C-24 oxidation pathway functions in vitamin D target cells to convert 1α,25-$(OH)_2D_3$ to the inactive excretory form, calcitroic acid [103,104] (Figure 1.3). The catabolism of 1α,25-$(OH)_2D_3$ has now been studied in a number of different cell lines derived from vitamin D target tissues including kidney, bone, intestine, keratinocyte and breast [96]. The cloning of CYP24A1 in 1991 by Okuda's group set the stage for metabolic analyses conducted using the recombinant protein by a number of groups which concluded that CYP24A1 is a multicatalytic enzyme responsible for the catalysis of the sequential metabolic steps that had previously been observed in the perfused rat kidney and the cultured cell models listed above [105-109]. An alternative 4-step pathway commencing with C23-hydroxylation, and culminating in 1α,25-$(OH)_2D_3$-26,23-lactone has also been identified [110]. The degree to which each pathway (C24- or C23-hydroxylation) occurs, appears to be species-dependent, with human CYP24A1 catabolizing 1α,25-$(OH)_2D_3$ via mainly C24-hydroxylation with some C23-hydroxylation; whereas species including rat and guinea pig catabolize 1α,25-$(OH)_2D_3$ almost exclusively via C24- or C23-hydroxylation respectively [111,112] (Figure 1.3).

Even though the precise steps in C-24 oxidation had been delineated, and the participation of CYP24A1 in this process had been determined, the physiological role of this pathway was not fully appreciated until the generation of a CYP24A1 knockout mouse by St-Arnaud's group. The workers found that a striking 50% of the mice died from hypercalcemia and nephrocalcinosis, and that the surviving animals developed an unmineralized bone matrix; the result of either the lack of a bone mineralizing hormone produced by CYP24A1, or due to a lack of catabolism of excess 1α,25-$(OH)_2D_3$ [113,114]. The latter explanation seemed to be the most likely, since crossing the animals with a VDR knockout mouse resulted in a normal bone phenotype and were therefore rescued from the deleterious effects of an

Figure 1.3: Catabolism of 1α,25-$(OH)_2D_3$ by CYP24A1. The mitochondrial cytochrome P450 CYP24A1 catalyzes the regio- and stereo-specific degradation of 1α,25-$(OH)_2D_3$ in target cells via two pathways commencing with either C24*R*- or C23*S*-hydroxylation and culminating in calcitroic acid (excreted in the bile), or 1α,25-$(OH)_2D_3$-26,23-lactone respectively. The cloning of CYP24A1 in the early 1990s, and subsequent enzyme kinetic analysis confirmed that CYP24A1 could catalyze all of the steps involved in the degradation of 1α,25-$(OH)_2D_3$. Catabolic pathway selection appears to be species dependent, where rat and guinea pig CYP24A1 have been reported to catalyzes only C24 or C23 hydroxylation, whereas human CYP24A1 can degrade 1α,25-$(OH)_2D_3$ via both pathways (with a preference for C24). CYP24A1 knockout mice exhibit hypercalcemia and an unmineralized bone matrix, suggesting that CYP24A1 plays an important physiological role in attenuating the 1α,25-$(OH)_2D_3$ biological signal by catabolizing this metabolite in target cells. CYP24A1 has also been shown to catabolize 25-OH-D_3 via similar intermediates, as denoted by a substitution at C1 in the pathway scheme [96].

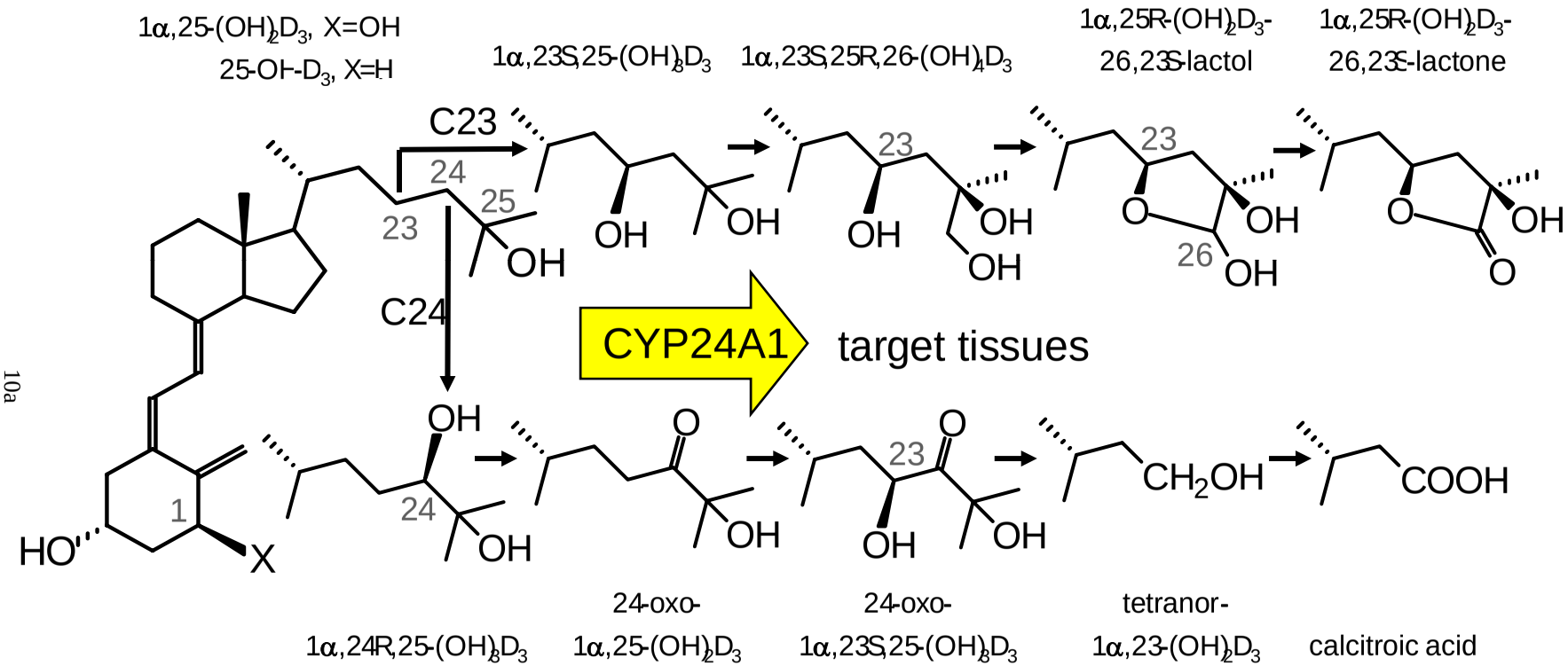
1α,25-(OH)2D3, X=OH
25-OH-D3, X=H
1α,23S,25-(OH)3D3
1α,23S,25R,26-(OH)4D3
1α,25R-(OH)2D3-26,23S-lactol
1α,25R-(OH)2D3-26,23S-lactone
C23
C24
CYP24A1
target tissues
1α,24R,25-(OH)3D3
24-oxo-1α,25-(OH)2D3
24-oxo-1α,23S,25-(OH)3D3
tetranor-1α,23-(OH)2D3
calcitroic acid

un-catabolized excess of 1α,25-$(OH)_2D_3$ [114]. This study helped rationalize two earlier pieces of work: that (1) 1α,25-$(OH)_2D_3$-intoxicated rats exhibited a similar bone phenotype to that observed in the CYP24A1-null mouse [115], and (2) the treatment of cultured bone cells with the general cytochrome P450 inhibitor ketoconazole, enhanced the hormonal action of 1α,25-$(OH)_2D_3$ [116]. More recent studies conducted using the CYP24A1 knockout mouse revealed severely impaired clearance of 1α,25-$(OH)_2D_3$ from the bloodstream after a bolus dose of 1α,25-$(OH)_2D_3$, and the inability of cultured primary keratinocytes from these mice to catabolize 1α,25-$(OH)_2D_3$ to calcitroic acid [117]. Collectively, these results suggest that the main physiological role of CYP24A1 is to regulate the hormonal action of 1α,25-$(OH)_2D_3$ by catalyzing its inactivation in target cells [106]. However, the question of whether CYP24A1 plays a bone anabolic role has re-emerged by work which suggests that fracture repair in CYP24A1-null animals occurs more slowly than the wild type animals, presumably due to the lack of a 24-hydroxylated metabolite [118].

1.4 VITAMIN D ANALOGS

The discovery of the antiproliferative properties of 1α,25-$(OH)_2D_3$, has led to the development of analogs of 1α,25-$(OH)_2D_3$. The main goal of analog design, is to generate a compound of increased biological potency while at the same time attempting to separate the calcium homeostatic and antiproliferative functions of 1α,25-$(OH)_2D_3$, such that an analog could be used to treat a hyperproliferative disorder without a hypercalcemic side effect. Vitamin D analogs now number in the thousands and represent modifications to every part of the 1α,25-$(OH)_2D_3$ molecule including the A,C,D rings, the cis-triene system, and the side chain [10,119]. It is believed that vitamin D analogs mimic the mechanism of action of 1α,25-$(OH)_2D_3$, whereby their differential interaction with activating enzymes, DBP, VDR and CYP24A1, results in an altered biological function in comparison to 1α,25-$(OH)_2D_3$ [106]. Many side-chain modified analogs of 1α,25-$(OH)_2D_3$, exhibit markedly reduced DBP-binding affinities, and this is believed to confer a target cell advantage over 1α,25-$(OH)_2D_3$. For example 20-epi-1α,25-$(OH)_2D_3$, an analog with no measurable binding affinity for the DBP, exhibited a 10-fold greater activity in a growth hormone gene transactivation study in the absence of serum compared to 1α,25-$(OH)_2D_3$, however when

serum was included in the medium, transactivation by the analog was 30-fold greater than that observed for 1α,25-$(OH)_2D_3$ [120]. According to this concept, even analogs with similar or slightly reduced VDR-binding affinities can yield potent biological effects, due in-part to poor binding affinity for the DBP. However, a reduction of DBP affinity opens up the possibility for transport of the analog on alternative carriers including lipoproteins or albumin, which could lead to an altered tissue distribution [121,122]. Furthermore, the 'target cell advantage' described above, turned out to be a target cell 'catch-22' for the analog MC903 (Calcipotriol), which is so rapidly catabolized by liver enzymes [50] and CYP24A1 in target cells [51] that it is inactive *in vivo* if administered systemically, despite a VDR-binding affinity similar to that of 1α,25-$(OH)_2D_3$ [123,124]. MC903 is marketed as a successful treatment of psoriasis, a hyperproliferative skin disorder, and is effective as a topical as opposed to systemic treatment because it can deliver its biological effect before becoming catabolized [106].

Early bone resorption assays used to characterize the function of vitamin D analogs, suggested that the potency of an analog depended on its VDR-binding affinity. In contrast to this hypothesis, many analogs possess inferior binding affinities to the VDR but are more potent than 1α,25-$(OH)_2D_3$ [119]. For example, the analog 16,23E-diene-26,27-hexafluoro-25-OH-D_3 binds the VDR with a 400-fold lower affinity than 1α,25-$(OH)_2D_3$, and is able to inhibit the growth of HL-60 cells 2-3-fold more effectively than 1α,25-$(OH)_2D_3$ [119,125]. In general, it is believed that analogs can increase the stability of the VDR-RXR-VDRE complex [126-128], and enhance co-activator binding, resulting in improved transactivation ability, despite a potentially reduced VDR binding affinity of the analog [129]. Perhaps the most desirable and yet elusive characteristic of certain vitamin D analogs is their ability to work selectively to achieve either a calcium homeostatic or antiproliferative effect. Some analogs, including KH1060 exhibit a 2000-fold specificity factor towards differentiative activity as opposed to calcemic activity [119]. One possibility is that the analog-VDR-RXR complex could preferentially bind a certain VDRE subtype. For example, the analog EB1089 has been shown to activate a VDRE characterized by an inverted palindromic sequence separated by 9 non-specific nucleotides, adopted by genes involved in cell cycle regulation [130], whereas 1α,25-$(OH)_2D_3$ does not appear to exhibit a preference for any VDRE sub-type [106,131]. Some analog-VDR-RXR complexes have been shown to recruit specific co-activators which could dictate the subset of vitamin D-dependent genes induced by a particular analog [125,132]. Another possibility is that the effect

of the target gene depends on the duration of the signal of the analog, whereby a calcemic effect requires a prolonged signal as opposed to a differentiative effect, which may only require a short pulse to cause a change in the cell cycle [133]. This model for analog selectivity is in somewhat contradiction to those described above because it suggests that a non-calcemic analog is also capable of transactivating a calcemic gene [133], however it does highlight the importance of DBP binding affinity and catabolism by CYP24A1 in affecting the half-life of the analog.

CYP24A1 is the main degredatory enzyme for 1α,25-$(OH)_2D_3$, and it appears as though this enzyme is also capable of catabolizing many analogs of 1α,25-$(OH)_2D_3$. Analogs including MC903, 22-oxa-1α,25-$(OH)_2D_3$ and EB1089 have been shown to be catabolized to products similar to those of the C-24 oxidation pathway in an inducible manner in vitamin D target cells [124,134,135]. Similarly, analogs that have been specifically designed to block 24-hydroxylation by CYP24A1, and as a result are hydroxylated at C-26 for example, strongly implies the involvement of CYP24A1 in their metabolism [125]. Recently we have studied the catabolism of 20-epi- and 20-CH_3-1α,25-$(OH)_2D_3$, and found that both of these analogs can be efficiently converted to side-chain truncated carboxylic acids, similar to calcitroic acid, which further attests to the role of CYP24A1 in the catabolism of analogs [136]. A recent study of non-steroidal analogs of 1α,25-$(OH)_2D_3$ containing CYP24A1-resistant modifications including 23-yne, 20-epi, and distal carbon fluorination, revealed an increase in the differentiation of colon cancer cells correlated with an increase in VDR/co-activator interactions relative to 1α,25-$(OH)_2D_3$ [137]. In the presence of a specific CYP24A1 inhibitor, the activity of 1α,25-$(OH)_2D_3$ began to approach the activity of the analogs, whereas the activity of the analogs exhibited no major changes [137]. This work demonstrates a contribution of altered catabolism by CYP24A1, within a context of altered DBP-binding, and VDR-binding and transactivation towards the overall differential activity of analogs relative to 1α,25-$(OH)_2D_3$. Taken together, vitamin D analogs represent a diverse set of compounds of potential clinical value in the treatment of hyperproliferative disorders or those relating to calcium homeostasis, however they have also proven to be very valuable tools used to study the mechanism of action of 1α,25-$(OH)_2D_3$.

1.5 CYTOCHROME P450 STRUCTURE AND FUNCTION

The term 'Cytochrome P450' entitles a superfamily of heme-thiolate enzymes named after their characteristic maximal absorption at 450nm when bound to carbon monoxide [138,139]. Although the most common reaction catalyzed by cytochrome P450 enzymes is the stereo- and regiospecific oxidation of hydrocarbons, a wide range of reactions attributed to catalysis by P450s have been identified including dealkylation, dehydration, dehydrogenation, isomerization, dimerization, carbon-carbon bond cleavage and reduction [140]. Cytochrome P450s can be found in most species ranging from bacteria to humans, and participate in anabolic/catabolic reactions involving a myriad of both endogenous and xenobiotic substrates including drugs, environmental pollutants, steroids, prostaglandins and fatty acids [141]. A nomenclature system has been devised to classify these enzymes on the basis of amino acid identity, phylogenetic criteria and gene organization. For example the designation as a cytochrome P450 'CYP' is followed by a number, representing at least 265 'families' with each member sharing 40% amino acid identity, followed by a letter to designate subfamilies possessing at least 55% amino acid identity, followed by a numeral which indicates the gene number. Alleles are also included for certain human P450 genes. Higher order classification of P450s involve groups of families or 'clans' that diverged from a single common ancestor, named after the lowest member family number. The human P450 genome comprises at least 60 genes subdivided into 18 families and 43 subfamilies, including families 2, 24, and 27 which include the main vitamin D metabolizing CYPs described above: CYP2R1, CYP24A1, CYP27A1 and CYP27B1 [142,143].

The cytochrome P450 catalytic mechanism requires the transfer of two reducing equivalents ($2e^-$) from NAD(P)H to the P450 heme iron, via one or two cofactors. Firstly, substrate binding displaces a water molecule bound to the heme, followed by the acceptance of a single reducing equivalent from the cofactor. The binding of molecular dioxygen and the receipt of a second reducing equivalent, results in the breakage of the molecular dioxygen bond. One oxygen atom is released as a water molecule, in the presence of two protons, leaving the highly reactive iron-oxo intermediate from which the oxygen atom is transferred to the substrate. The general P450 reaction mechanism is shown in the following equation, where RH denotes the substrate to become hydroxylated: $RH + O_2 + 2H^+ + 2e^- \rightarrow ROH + H_2O$ [141,144]. The two main classes of eukaryotic P450s, mitochondrial and microsomal P450s, differ in the number and type of cofactors used to transfer reducing equivalents from NADPH to the P450 component. For

mitochondrial CYPs, a hydride ion from NADPH is transferred to the flavin adenine dinucleotide (FAD) prosthetic group of ferredoxin reductase, forming a two-electron reduced form. Subsequently, a pool of ferredoxin molecules (iron-sulphur proteins), receives single electron reducing equivalents from ferredoxin reductase which are ultimately transferred to the heme iron of the P450. Mitochondrial CYPs (including CYP24A1) are located on the matrix side of the inner mitochondrial membrane, and contain an amino terminal mitochondrial targeting sequence which becomes cleaved [145,146]. Alternatively, microsomal enzymes (including CYP2R1) receive their two reducing equivalents directly from NADPH-P450 reductase, containing both an FAD as well as a flavin adenine mononucleotide (FMN) prosthetic group without the need for ferredoxin intermediates [13,141]. Microsomal CYPs are associated with the endoplasmic reticulum, and also possess an amino terminal targeting sequence, which does not become cleaved [147-149].

Despite amino acid sequence identities down to 15-20% in some cases, P450s possess a remarkably conserved tertiary structure, roughly comprising 13 alpha helicies and 5 beta sheet structures that form a globular to triangular scaffold around a buried heme prosthetic group ranging in size from 480-560 amino acids [141,150]. The regions of greatest structural conservation are located closest to the heme and contain the three absolutely conserved residues found in P450s that are consistent with a common catalytic mechanism including a Cys residue (Cys462 in CYP24A1) within the consensus sequence Phe-X-X-Gly-X-X-X-Cys-X-Gly, which forms the characteristic fifth iron coordinating ligand on the proximal side of the heme [151]. This 'Cys loop' is located in between a coiled 'meander region' and the L-helix. Commonly referred to as the 'ERR triad', the conserved Glu-X-X-Arg in the K-helix (residues 383-386 in CYP24A1) forms a tripartite salt bridge with Arg439 in the meander region within a network of highly conserved hydrogen bonds [152-154]. The ERR triad is believed to stabilize the heme via binding with the Cys loop, as well as stabilize the surface on the proximal side of the heme proposed to participate in co-factor binding [152,155]. The oxygen binding site motif comprising Gly/Ala-Gly-X-Asp/Glu-Thr (including Thr 330 in CYP24A1) on the distal side of the heme located in the I-helix is also highly conserved [156].

The most variable regions of P450s include substrate recognition sites (SRS) that extend away from the proximal side of the heme that collectively form the substrate binding pocket. The amino acid

residues contained within the SRSs are major determinants of the properties of individual CYPs including substrate specificity, reaction kinetics and regioselectivity [157,158]. As the crystal structures of the mammalian microsomal CYPs began to emerge starting in 2000, it became apparent that many of the proposed SRSs originally identified on the basis of prokaryotic CYP crystal structures were similar to those observed from the microsomal ones [141]. To date, the structures of 25 P450s have been crystalographically determined. In general, the substrate recognition sites identified by Gotoh and colleagues comprise: the B′ and flanking regions, the C-terminal end of the F-helix, the N-terminal ends of the G and I helicies, the β3 region, and the centre of the β5 sheet [159]. A successful strategy used to identify important determinants of characteristic P450 activity has been to reciprocally substitute amino acid residues between two highly similar but functionally unique isoforms, with the objective of identifying the residues responsible for the differences observed between the compared isoforms. For example, the androgen 15α-hydroxylase activity of CYP2A4 and the coumarin 7α-hydroxylase of CYP2A5 could be 'swapped' between these 98% identical enzymes by making reciprocal amino acid substitutions [157,160]. This work highlighted the concept that relatively few, strategically-placed substrate contact residues are responsible for drastically different enzymatic properties. Wade and colleagues have more recently extended the identification of SRSs, with the classification of putative substrate access/product egress channels based on molecular dynamics simulations using existing P450 crystal structures [161,162]. The most common secondary structures defining the access/egress channels include the F and G helicies (as well as the F-G loop) which span the substrate binding pocket. The pw2a channel, defines a route from the heme via the B′-helix/B-B′ loop/B-C loop and the β1 sheet to the F-G loop. Pathway pw2b defines access/egress via the B-B′ loop and the β1 and β3 sheets. Pathway pw2c involves a channel along the length of the I-helix, between helicies I and G, as well as the B′-helix and the B-C loop. Solvent and water channels have also been proposed [162]. Taken together, the cytochromes P450 represent a diverse superfamily of heme-thiolate enzymes which share a common mechanism of oxygen activation to catalyze hydroxylation of a broad range of substrates. A group of microsomal and mitochondrial P450s are involved in regulating the formation (CYP2R1, CYP27A1, CYP27B1) and degradation of the active vitamin D metabolite 1α,25-$(OH)_2D_3$ (CYP24A1).

1.6 THESIS OBJECTIVES

Prior to the work to be presented in this thesis, the complex multi-step catabolism of 1α,25-$(OH)_2D_3$ by hCYP24A1 had been well studied in various mammalian cell lines and bacterial expression systems using a variety of techniques including photodiode array (PDA) spectrophotometry, radioflow chromatography and liquid chromatography mass spectrometry. Investigators were intrigued by the fact that a single enzyme could catalyze each of 5 or 4 sequential steps in each of two distinct catabolic pathways commencing with either C24- or C23-hydroxylation respectively, resulting in products of reduced biological activity. CYP24A1 had also been shown to be involved in the catabolism of a wide range of 1α,25-$(OH)_2D_3$ analogs. The overall objective of research in our laboratory is to identify the molecular determinants of the multi-catalytic activity of human(h) CYP24A1. Given that the crystallographic determination of the structure of the mitochondrial CYPs continued to remain elusive, Dr. David Prosser from our group used a homology modeling-based approach to study the three-dimensional protein structure of hCYP24A1 [151]. Most importantly, the homology model containing a docked 1α,25-$(OH)_2D_3$ molecule was used to select putative substrate-contact residues for site-directed mutagenesis studies in order to address how these residues contribute to hCYP24A1 activity [151]. A homology modeling approach appeared particularly feasible for P450s, which share a canonical P450 fold, and based on observations that the newly emerging microsomal P450 crystal structures shared similar SRSs with the prokaryotic CYP crystal structures. The mutagenesis strategy was also guided by limited differences in protein sequence observed between hCYP24A1 (primarily a C24-hydroxylase) and opossum CYP24A1 (primarily a C23-hydroxylase [164]) located within the putative substrate-binding pocket predicted to be determinants of the regioselectivity of CYP24A1. In order to study the structure and function of CYP24A1 I set out to:

1. Design and implement a mammalian cell expression system to express selected CYP24A1 mutants (Chapter 2).
2. Develop an assay to study the multistep catabolism of 1α,25-$(OH)_2D_3$ by human CYP24A1 (Chapters 2 & 3).
3. Compare the catabolism of 1α,25-$(OH)_2D_3$ by human wild type CYP24A1 and the mutant CYP24A1 proteins (Chapters 3 & 4).

4. Compare the catabolism of selected analogs & prodrugs of 1α,25-$(OH)_2D_3$ using wild type and selected mutant CYP24A1 proteins (Chapter 5).
5. To attempt to rationalize the observed metabolism of 1α,25-$(OH)_2D_3$ and its analogs using existing homology models of the vitamin D-related cytochrome P450s (Chapters 3-6).

CHAPTER 2: MATERIALS AND METHODS

2.1 CELL CULTURE

Cultured cell models of vitamin D metabolism studied in this thesis include: V79-4 (American Type Culture Collection (ATCC), Manassas VA, USA; CCL-93) [163], V79-CYP24 (courtesy of Cytochroma Inc, Markham ON, Canada) [164], Opossum Kidney (OK) (ATCC CRL-1840) [165,166], HPK1A-ras (courtesy of Dr. R. Kremer, McGill University, Montreal PQ, Canada)[167,168], LLCPK1(ATCC CL-101) [169] and HEK-293 (ATCC CRL-1573) [170] (Table A2.1). A set of CYP24A1-expressing cell lines was also generated using the Flp-In transfection protocol [171](Invitrogen; described below; Figure 2.1). Firstly, a host cell line termed MK3 was generated, and subsequently transfected with plasmids encoding for wild-type human CYP24A1 and 42 single point or double mutants. All cells were maintained in 100mm cell culture dishes in a humidified atmosphere of 5% CO_2 in air at 37 °C. The culture medium compositions of the cell lines studied are described in the Appendix in Table A2.1. Dulbecco's Modified Eagle Medium (DMEM), Medium 199 antibiotic/antimycotic solution (100×), trypsin (0.25%), sodium pyruvate (100mM), hygromycin B (50 mg/ml), and zeocin (100 mg/ml) were purchased from Invitrogen. Minimum essential medium (MEM) Eagle containing non-essential amino acids, and ethylenediaminetetraacetic acid (EDTA), and dimethyl sulphoxide (DMSO) were purchased from Sigma. Fetal bovine serum (FBS) was purchased from Hyclone Laboratories (Logan UT, USA), Phosphate buffered saline (PBS) consisted of the following components in distilled-deionized (dd) H_2O: 0.54 mM potassium chloride (KCl), 0.14 mM KH_2PO_4, 13.7 mM sodium chloride (NaCl), and 10 mM sodium phosphate dibasic (Na_2HPO_4-$7H_2O$). Trypsin-EDTA solution was composed of 10% (v/v) and 5 mM EDTA in PBS.

At approximately 90% confluence, the cells were subcultured by trypsinization. Media was aspirated and the cell monolayer was rinsed with 3 ml of PBS, and aspirated. 1 ml of trypsin-EDTA solution was added to the plate, and tilted to ensure even distribution over the surface of the plate. The plate was incubated at room temperature for several minutes. Highly adherent cell lines such as HPK1A-ras and OK cells were incubated at 37 °C during trypsinization. When the cells became separated from the plate, 0.5 ml of the appropriate medium was added, and the solution was transferred to a 1.5 ml microfuge tube, and centrifuged at 2000×*g* for 3 min.

The supernatant was discarded, and the cell pellet was re-suspended in the appropriate medium and diluted 1/20 (1/12 for HPK1A-ras cells) into new plates containing 8-10 ml of the appropriate medium. Alternatively, in the preparation of frozen stocks, the cell pellet was resuspended in 900 μl of medium and transferred to a sterile cryovial containing 100 μl of DMSO, and stored in liquid nitrogen.

2.2 PREPARATION OF pcDNA5/FRT-BASED CYP24A1 EXPRESSION CONSTRUCTS

Wild-type human CYP24A1 and the adjacent V_5/His epitope tag, was subcloned from pcDNA3.1-V_5/His B (Invitrogen) into the *Nhe1*/*Bcl*II restriction sites in pcDNA5/FRT (Invitrogen, Figure 2.1). A second construct was generated in which only the V_5/His component was subcloned into the *Xho*1/*Bcl*II restriction sites in pcDNA5/FRT. The 13 CYP24A1 mutants W75L, I131A, I131F, W134F, L148A, L148F, M246L, M252L, M252T, S390G, V391L, G499V, L501I, were subcloned from pcDNA3.1-V_5/His B into the *Nhe1*/*Xho*1 restriction sites in pcDNA5/FRT containing the V_5/His epitope tag. All other mutants studied in this thesis were generated by site-directed mutagenesis using pcDNA5/FRT-CYP24A1-V_5/His as the template. The site-directed mutagenesis reactions were conducted by other laboratory members including Dr. David Prosser, Mr. Brendan O'Leary and Mr. Kenward Vong, using a Quick Change site directed mutagenesis kit (Strategene; La Jolla CA, USA).

The following is a typical procedure describing the excision of an insert encoding for a CYP24A1 mutant in pcDNA3.1-V_5/His B and subsequent ligation into pcDNA5/FRT-V_5/His. Approximately 15 μg of pcDNA5/FRT-V_5/His and 20 μg of the pcDNA3.1-V_5/His B construct were digested in separate tubes with 50 units of *Nhe*1 in the appropriate restriction enzyme buffer at 37°C for 1.5 h. The digestion reactions were ethanol precipitated by adding 0.2 volumes of 10 M ammonium acetate and 2 volumes of ethanol, and stored at –20°C for 40 min. DNA was isolated by centrifugation at 13 000×*g* for 30 min. The supernatant was discarded, and 2 volumes of 70% ethanol were added to the tube and re-centrifuged to wash the pellet. The wash was removed and the pellet was air dried at room temperature for 20 min. Each DNA pellet was redisolved in the appropriate buffer, and digested with 50 units of *Xho*1 for 1.5 h at 37 °C. The digested pcDNA5/FRT-V_5/His was treated with 4 μl of calf intestinal alkaline phosphatase and incubated for an additional 30 min at 37 °C. The DNA fragments were separated on a 1.2% agarose gel at 100 V for approximately 1.2 h. The gel was stained in 0.5 μg/ml ethidium bromide for 10 min and

destained in water for an additional 10 min. The gels were observed under UV light, and bands corresponding to the *Nhe1*/*Xho*1-digested pcDNA5/FRT-V_5/His and the insert encoding for the CYP24A1 mutant under preparation, were excised with a clean scalpel. DNA was extracted from the gel slices with a gel purification kit (Qiagen) according to the manufacturer's instructions. Each DNA type was typically extracted over 2 columns, where each column was eluted in 50 µl of the supplied elution buffer. The 100 µl solution from each DNA type was re-extracted to concentrate the sample, and eluted in 35 µl of sterile water. The DNA preparation typically resulted in host and insert DNA working solutions of 50 ng/µl and 30-40 ng/µl respectively.

A set of ligation reactions were prepared, varying such factors as the amount of host DNA (12.5, 25 and 50 ng) insert DNA (7.5, 15 and 30 ng), and T4 DNA ligase (Invitrogen) (1, 2 and 5 units). The DNA was added to a tube containing 1.5 µl of 10×ligation buffer and the amount water required to achieve a final volume of 15 µl. The tubes were mixed gently, placed on ice for 2 min, and transferred to a 12 °C bath. T4 DNA ligase was added, and the tubes were incubated overnight at 12 °C. A 0.5-5 µl volume of ligation reaction was used to transform subcloning efficiency DH5α chemically competent *E. coli* cells (Invitrogen). For each transformation, the selected volume of ligation reaction was transferred into 65 µl of pre-thawed DH5α cells, and the mixture was stirred. The cell-DNA mixture was incubated on ice for 30 min, promptly heat shocked for 90 s in a 42 °C bath, and incubated on ice for 2 min. A 500 µl volume of 37 °C super optimal broth with catabolite repression (SOC medium) was added to the tube and incubated in a 37 °C shaker for 1 h. SOC medium was prepared immediately before use by supplementing super optimal broth (SOB) medium to contain 0.2 M glucose. SOB medium comprised a solution of 2% (w/v) tryptone, 0.5% yeast extract, 0.05% NaCl in water, and supplemented with filter-sterilized 10 mM $MgCl_2$ and 10 mM $MgSO_4$ after autoclaving. A 250 µl amount of transformation solution was plated on Luria-Bertani (LB) agar plates supplemented with 100 µl/ml of ampicillin (amp), and incubated overnight at 37 °C. LB plates were prepared by combining 10 g/l tryptone, 5 g/l yeast extract, 10 g/l NaCl, pH 7.0. 15 g/l agar was added and the solution was autoclaved. The solution was supplemented with 100 µl/ml of ampicillin when cooled to below 60 °C and poured into 100 mm plates and allowed to solidify at room temperature, before storing at 4 °C.

Single colonies were isolated and grown overnight in 2 ml of LB/amp medium, and DNA was purified using a mini-scale plasmid purification kit (Qiagen). LB/amp medium was prepared as described above, without the addition of agar. Purified DNA was subjected to diagnostic digests with *Nhe*1 or *Xho*1 to confirm the purity of the DNA, a double *Nhe1*/*Xho*1 digest to confirm the presence of the insert, and a single *Age*1 digest to confirm the presence of the V_5/His tag. Selected clones that satisfied the diagnostic digests were submitted for sequencing analysis to confirm the presence of the intended mutation (Cortec DNA Services Laboratory, Kingston ON, Canada). Sequencing-confirmed clones were streaked onto fresh LB/amp agar plates and a single colony was isolated and grown in a 3 ml LB/amp culture for 8 h. The 3 ml culture was used to inoculate 500 ml of LB/amp, which was incubated in a 37 °C shaker overnight. DNA was purified using a maxi-scale plasmid purification kit (Qiagen) and stored in TE buffer at –20 °C. DNA purity and concentration was determined by spectrophotometry (See Mathematical and Statistical Treatment of Data). The plasmids pcDNA5/FRT-CYP24A1-V_5/His and pcDNA5/FRT-V_5/His were prepared using a similar procedure as described above, except that parent vector pcDNA 3.1-V_5/His and host vector pcDNA5/FRT were initially propagated using a DNA adenine methylase/DNA cytosine methylase deficient strain of chemically competent *E. coli* (SCS110, Stratagene) to facilitate digestion with the methylation-sensitive enzyme *Bcl*II.

2.3 TRANSFECTION OF V79-4 CELLS WITH pFRT/*lac*ZEO

V79-4 Cells were stably transfected with the plasmid pFRT/*lac*Zeo (Invitrogen), containing a Flp recombinase target (FRT) site (Figure 2.1). An appropriate amount of plasmid was linearized with *Sca* I (Fermentas), and re-purified using a gel extraction kit (Qiagen) according to the manufacturer's instructions. V79-4 cells were plated at a density of 1.5×10^4 cells per well in 6-well plates and allowed to recover overnight. The cells were transfected with 0.2, 0.5, 1, 2, and 4 μg of linearized pFRT/*lac*Zeo in triplicate wells using Lipofectamine and Plus transfection reagents (Invitrogen). The appropriate amount of DNA was diluted into 115 μl of transfection medium per well (DMEM supplemented only with 2.25 g/l glucose). A 10 μl amount of Plus reagent was added, the solution was mixed gently and incubated at room temperature for 15 min. In a separate tube, 10 μl of Lipofectamine reagent was added to another 115 μl of transfection medium and gently mixed. The Lipofectamine solution was combined with the DNA-Plus

Figure 2.1: Overview of the Flp-In transfection method (Invitrogen). Firstly, pFRT/*lac*Zeo containing a flp recombinase target (FRT) site for targeted genomic integration was transfected into V79-4 cells. A zeocin-resistant clone containing a single pFRT/*lac*Zeo integration of high β-galactosidase activity, was selected as the Flp-In host cell line (MK3). Secondly, MK3 cells were transfected with pcDNA5/FRT-V_5/His, an expression plasmid containing CYP24A1 in the presence of pOG44, encoding for the Flp recombinase. Transient expression of pOG44 catalyzes homologous recombination between the FRT site on pcDNA5/FRT-V_5/His and the FRT site at the integration site of pFRT/*lac*Zeo in the MK3 cells, which should result in reproducible targeted integration of CYP24A1 constructs into the same integration site in the genome. Successful recombinants were selected on the basis of hygromycin B resistance [171].

solution, mixed gently, and incubated at room temperature for 15 min. The medium was aspirated from the cells and the cells were rinsed twice with transfection medium, and 1ml of fresh transfection medium was added to each well. The 250 μl DNA/Plus/Lipofectamine solution was added to each well, and gently mixed into the transfection medium. The cells were incubated for 3 h in a 37 °C incubator. The transfection medium was aspirated and replaced with 2ml of culture medium (DMEM supplemented with 10% FCS, 1% antibiotic/antimycotic and 2.25 g/l glucose). All of the transfection specifications are described on a per well basis, however a 750 μl DNA/Plus/Lipofectamine stock solution containing 3× the amount of each component was prepared for triplicate transfections.

The day after transfection, the medium was replaced with fresh medium. Two days following transfection, the cells were split so that they were approximately 15-20% confluent. Three days following the transfection, the culture medium was replaced with medium containing 375 μg/ml zeocin. Stable transfectants were selected in the zeocin-containing medium for 13-17 days until well-defined foci were observed, and all non-transfected V79-4 cells were dead. Before starting the transfection, we conducted a zeocin sensitivity study, in which 15-20% confluent V79-4 cells were incubated in medium containing 100-1000 μg/ml zeocin. All V79-4 cells cultured in medium containing at least 350 μg/ml zeocin, died within 10-13 days of selection. Thirty six zeocin-resistant foci from the plates transfected with 1 μg of pFRT/*lac*Zeo were isolated and transferred to 12-well plates, and sequentially expanded into 6-well plates, 60 mm plates, and then into 100 mm plates. The V79-4 cell lines stably transfected with pFRT/*lac*Zeo were maintained in 100 mm plates in medium containing 375 μg/ml zeocin for approximately 7 weeks, at which time zeocin was gradually removed from the culture medium. Of the 36 zeocin-resistant foci selected for expansion, 10 did not survive continued propagation in medium containing zeocin. The remaining 26 cell lines were screened by β-galactosidase and Southern blot assays described below.

2.4 β-GALACTOSIDASE ASSAY

A β-galactosidase assay kit (Invitrogen) was used to compare the levels of transcriptional activity at the site(s) of integration of pFRT/*lac*Zeo, in the cell lines derived from zeocin-resistant foci (Figure 2.2A). Approximately 3×10^6 transfected cells were harvested from 60mm plates by trypsinization, and the cell suspension was centrifuged at 2000×g. Each pellet was re-suspended in 60 μl of 1×lysis buffer. The

cell suspension was flash frozen in a dry ice/ethanol solution and thawed in a 37 °C water bath. Two additional freeze/thaw cycles were conducted, for a total of three freeze/thaw cycles. Insoluble cell material was pelletted by centrifugation at 13 000×*g*, and the supernatant was transferred to a clean microfuge tube and stored at –20 °C. The β-galactosidase assay was conducted on a 96-well plate scale using a microtiter plate reader. A 50 µl amount of 1×cleavage buffer with β-mercaptoethanol, and 17 µl of orthonitrophenol-β-D-galactopyranoside (ONPG) was added to each well of the microtiter plate, according to the manufacturer's instructions. The cell lysates were thawed on ice, and 2, 4 and 8 µl volumes of each lysate were added to duplicate wells. The plates were covered and incubated for 30 min at 37 °C, and the absorbance was subsequently read at 420 nm. Three volumes of lysate were tested to confirm linearity of the OD_{420} readings. A microtiter scale Bradford Assay was also conducted in triplicate using 1.6 µl of lysate, to determine the total protein concentration, and to calculate the specific β-galactosidase activity for each cell line. A lysate from non-transfected V79-4 cells was used as a negative control, and a source of purified β-galactosidase (Sigma) was used as a positive control (Figure 2.2A & data not shown). See Mathematical and Statistical Treatment of Data.

2.5 SOUTHERN BLOT ANALYSIS

Generation and labeling of the probe. The putative host cell lines derived from zeocin-resistant foci were studied by southern blot analysis to confirm genomic integration of pFRT/*lac*Zeo, and to assess the number of integration sites. A 363 bp fragment (bp 3315-3678) contained within the *lac*Z open reading frame (bp 675-3722) in pFRT/*lac*Zeo was selected as the template for the probe to be used in the southern blotting analysis. In a typical template preparation, 30×1µg digestions of pFRT/*lac*Zeo were carried out in 15µl volumes containing 10 units of *Pvu*II in the appropriate restriction enzyme buffer for 1.5 h. Each 15 µl digestion was supplemented with 3 µl of 5×orange G gel loading dye and subjected to electrophoresis on a 1.8% (w/v) agarose gel at 100 V for 1.25 h. The gel was stained in 0.5 µg/ml ethidium bromide for 10 min, destained in ddH_2O for 10 min and observed under ultraviolet light. Digestion of pFRT/*lac*Zeo with *Pvu*II generated 5 fragments including the target 363 bp probe template, which was excised from the gel with a clean scalpel. The gel-embedded DNA was purified over 4 gel extraction columns (Qiagen)

according to the manufacturer's instructions. Each column was eluted with 50 µl of the supplied elution buffer (EB), resulting in a 200 µl working solution of approximately 5ng/µl of the template DNA. The purified 363 bp fragment from pFRT/*lac*Zeo was stored at –20°C.

On the day of the Southern blot analysis, the template was labeled with [α-^{32}P]deoxyadenosine triphosphate (dATP) (3000 Ci/mmol, 10 mCi/ml; PE Biosciences, Boston MA, USA) using a DECAprime II (Ambion, Austin TX, USA) random priming kit. A 25 ng amount of the template DNA was diluted to 11.5 µl with sterile water, and denatured by incubating in boiling water for 7 min. The DNA was subsequently frozen in dry-ice/ethanol, thawed, and centrifuged to collect the sample. A 5 µl amount of 5× -dATP reaction buffer and 5 µl of [α-^{32}P]dATP were added on ice to the DNA/Decamer mixture. A 1 µl volume (5 units) of exonuclease-free Klenow was subsequently added, the reaction mixture was gently mixed and incubated for 20 min at 37°C. At the end of the incubation period, 1 µl of 0.5 M EDTA was added to stop the reaction.

Trichloroacetic acid (TCA) precipitation was used to determine the specific activity of the probe. A 2 µl amount of the reaction mixture was added to 150 µl of a 1 mg/ml solution of yeast tRNA. 50 µl of this solution was counted, and another 50 µl was transferred to a tube containing 2 ml of cold 10% TCA and mixed thoroughly. The TCA solution was incubated on ice for 10 min. The TCA-precipitated DNA was collected using vacuum filtration onto a GF/B glass fiber filter (Whatman). Two 1 ml rinses of the precipitation tube with 1 ml of 10% TCA were passed through the filter, followed by an additional rinse with 3 ml of 95% ethanol. The glass fiber filter was subjected to liquid scintillation counting, and the specific activity of the probe was determined. The specific activities of the probe preparations used throughout the Southern blotting assays ranged from 0.91 to 2.81×10^9 cpm/µg (See Mathematical and Statistical Treatment of Data).

Unincorporated nucleotides were removed from the probe synthesis reaction by passing the reaction solution through a Micro Bio-spin chromatography column (BioRad, Hercules CA, USA) containing 2 ml of Sephadex G50 (Amersham) resin. The sample was placed at the top of the column and centrifuged at 2000×g for 8 s. The eluate containing the purified probe was heat denatured at 90 °C for 10 min immediately before use.

Genomic DNA preparation and digestion. Approximately 5×10^6 cells from each zeocin-resistant cell line were harvested from p100 plates by trypsinization, and genomic DNA was extracted using an EasyDNA tissue kit (Qiagen) according to the manufacturer's instructions. DNA was recovered from the extraction columns in two 200 µl elutions in buffer AE. A 10 µg amount of DNA derived from each cell line was diluted in an appropriate volume of sterile water and 10× restriction enzyme buffer, and stored at 4 °C for 2-3 h with periodic stirring. 50 units of *Hind*III or *Bam*HI was added and the digestion reactions were transferred to a 37 °C bath. After 20 min, a second aliquot of restriction enzyme was added, and the digestion was continued overnight at 37 °C. The DNA fragments were ethanol precipitated and re-dissolved in 25 µl of TE buffer and supplemented with 5 µl of 5× orange G loading dye. The fragments were separated on a 10×15cm, 0.7%(w/v) agarose gel in TAE buffer at 100 V for approximately 1.25 h. A 500 µg amount of λ *Hind*III fragments was used as molecular weight markers, and 10 µg of digested DNA from non-transfected V79-4 cells was used as a negative control.

Southern transfer, hybridization and detection. The gel was denatured in alkaline transfer buffer (0.4 M NaOH, 1 M NaCl) with gentle shaking for 15 min. The transfer buffer was replaced and denaturation was continued for an additional 15 min. The gel was inverted, and the DNA was transferred to a positively charged nylon membrane (Hybond XL, GE Healthcare) by capillary action on a standard Southern blotting apparatus for 18-24 h, using the alkaline transfer buffer described above. The membrane was soaked in neutralization buffer (0.5 M Tris-Cl (pH 7.2), 1M NaCl) for 5 min, and transferred to a tray containing 6×sodium chloride/sodium citrate buffer (SSC; for 20×: 3 M NaCl, 0.3 M $C_6H_5Na_3O_7$-$2H_2O$, pH 7.0) until wetted from beneath. The membrane was submerged in the 6×SSC for 2 min. The membrane was prehybrizided for 30 min in a roller bottle in a 68 °C hybridization chamber using 70 µl of prehybridization solution per 1 cm^2 of membrane. The prehybridization solution contained 5×sodium chloride/sodium phosphate EDTA buffer (SSPE), 5×Denhardt's reagent, 0.5% (w/v) sodium dodecyl sulphate (SDS), and 100 µl/ml yeast tRNA. A 20× stock of SSPE buffer contained 3 mM NaCl, NaH_2PO_4-H_2O, 20 mM EDTA, 10 M NaOH. A 50× stock of Denhardt's reagent contained 0.5% (w/v) ficoll-400, 0.5% polyvinylpyrolidone (PVP) and 0.1% bovine serum albumin fraction V (BSA; Roche, Mannheim, Germany).

The prehybridization solution was decanted from the roller bottle and replaced with the same volume of hybridization fluid, comprising prehybridization fluid and freshly-denatured probe. The roller bottle was returned to the hybridization chamber and the membrane was hybridized overnight at 68 °C. Typically, 8.35×10^4-4.65×10^5 cpm/cm^2 of membrane was used for southern hybridization. The hybridization solution was removed, and membrane was transferred to a tray containing a low stringency wash buffer (2×SSC, 0.1%(w/v) SDS) and rinsed briefly. Two 10-min washes were done with gentle shaking at room temperature using the low stringency buffer. A medium stringency buffer (0.5×SSC, 0.1%SDS) was used for two subsequent 15-min washes at room temperature. Three 10-min washes were completed using a high stringency wash buffer (0.5×SSC, 0.1% SDS) at 65 °C. The membrane was rinsed briefly with 0.1% SSC, wrapped in a single layer of plastic wrap, and exposed to X-ray film (Hyperfilm MP; GE Biosciences, Buckinghamshire UK) for 24-48 h at -70°C. The number of integration sites of pFRT/*lac*Zeo in each cell line was determined by the number of hybridizing bands observed, since *Hind*III or *Bam*H1 cut at only a single location on pFRT/*lac*Zeo outside of the probed *lac*Z-zeocin gene (Figure 2.2 B,C).

2.6 TRANSFECTION OF pFRT/*lac*Zeo-CONTAINING V79-4 CELLS WITH pcDNA5/FRT-CYP24A1

The cell line derived from zeocin-resistant focus No. 3, stably transfected with pFRT/*lac*Zeo (termed MK3 cells) was selected as the host cell line to be transfected with the pcDNA5/FRT-based constructs containing CYP24A1 mutants, on the basis of β-galactosidase and Southern blot assays described above, which indicated that the FRT integraton cassette on pFRT*lac*Zeo was integrated into a single site of relatively high transcriptional activity in this cell line. The expression vector pcDNA5/FRT and a plasmid encoding for the Flp recombinase, pOG44 (Invitrogen) were co-transfected into MK3 cells (Figure 2.1). The transient expression of pOG44 was sufficient to mediate the homologous recombination of CYP24A1 in pcDNA5/FRT into the FRT site, stably integrated into the MK3 cells. Successful recombination events were selected on the basis of hygromycin B resistance.

MK3 cells were plated at a density of 2.0×10^4 cells per well in 6-well plates and allowed to recover overnight. The cells were co-transfected with 0.4 μg of pcDNA5/FRT-CYP24A1 and 3.6 μg of

Figure 2.2: Screening of zeocin-resistant foci by β-galactosidase and Southern blot assays. Thirty-six zeocin-resistant foci derived from pFRT*lac*Zeo-transfected V79-4 cells were isolated and expanded. Ten of the foci did not survive prolonged exposure to zeocin. The relative transcriptional activity at the site(s) of integration was assessed by a β-galactosidase reporter assay (A). Data points represent the mean of duplicate measurements taken from each of 2, 4 and 8µl volumes of lysate to confirm linearity of the signal. Error bars are the standard error of the mean (n=6). The foci were then screened by Southern blotting in order to establish the number of integration sites of pFRT*lac*Zeo as indicated by the number of hybridizing bands (B,C), using a probe directed against the lacZ-zeocin gene, where *Hind*III was used to digest the genomic DNA. The representative Southern blot in B surveys the distribution of the number of integration sites determined, as summarized for all zeocin-resistant clones by colour coding in part A. Seventeen of the 26 clones were determined to be single integrants. Four of the single integrants expressing relatively high levels of β-galactosidase were selected for additional Southern blotting with a second enzyme (*Bam*H1) in order to confirm integration at a single site (B). A hybridizing band for foci No. 18 and 22 was not consistently observed (ND). Zeocin-resistant foci No. 3 (MK3) which consistently yielded a single hybridizing band with each of two enzymes, and possessed a high β-galactosidase activity, was selected as the host cell line to receive the pcDNA5/FRT-based expression constructs encoding for the mutant CYP24A1 proteins under investigation in this thesis. No hybridizing band was observed for non-transfected V79-4(V4) cells.

pOG44 using Lipofectamine and Plus reagents as described above. One well was transfected for each of the 43 CYP24A1 constructs under investigation (Table 2.2). The day after transfection, the medium was replaced with fresh medium. Two days following transfection, the plates of cells were diluted so that they were approximately 15-20% confluent. Three days following the transfection, the culture medium was replaced with medium containing 92.5 μg/ml hygromycin B. Stable transfectants were selected in the hygromycin-containing medium for 13 days until well-defined foci were observed, and all non-transfected MK3 cells were dead. Prior to starting the transfection, we conducted a hygromycin B sensitivity study, in which 15-20% confluent MK3 cells were incubated in medium containing 10-200 μg/ml hygromycin B. All MK3 cells cultured in medium containing at least 85 μg/ml hygromycin B, died within 10-13 days of selection. The hygromycin B-resistant foci within each well were pooled and re-plated into 6-well plates, and sequentially expanded into 60 mm plates, and then into 100 mm plates. All of the cell lines were maintained in 100 mm plates in culture medium containing 92.5 μg/ml hygromycin B. The relative CYP24A1 mRNA expression levels among the hygromycin-resistant cell lines was determined by real time polymerase chain reaction (rtPCR) in collaboration with research technician, Mrs. Shelly West (Table A2.2).

2.7 INCUBATION OF CYP24A1-EXPRESSING CELLS WITH VITAMIN D SUBSTRATES

In preparation for incubation of stably transfected MK3 cells with vitamin D substrates (Table 2.2), 2.4×10^6 cells were plated into 60 mm dishes and allowed to recover for 24-48 h. The medium was aspirated and the cells were rinsed with PBS. A 2 ml amount of incubation medium was dispensed into each plate, and supplemented with 1 μl of a 100 mM stock solution of the antioxidant 1,2-dianilinoethane (DPPD, ICN Biomedical Aurora OH, USA). The incubation medium comprised the standard culture medium, with the exception that 1% (v/v) bovine serum albumin (BSA, Roche, Mannheim Germany) was substituted for FBS (Table A2.1), and supplemented with the appropriate amount of $1\alpha,25\text{-}(OH)_2D_3$ (courtesy of Dr. A.-M. Kissmeyer, Leo Pharmaceutical Products, Ballerup Denmark) or 25-OH-D_3 (Fluka). The volume of the added substrate (in ethanol), was adjusted by evaporation and re-constitution so that the total volume of ethanol in the incubation medium did not exceed 0.1%. In a typical analytical assay,

1.5×10^5 counts per minute (cpm) of [1β-^{3}H]1α,25-$(OH)_2D_3$ (44 Ci/mmol; prepared by Dr. G. Jones) or [26,27-^{3}H] 25-OH-D_3 (30 Ci/mmol, Amersham, Buckinghamshire UK) per 60 mm plate was added so that metabolism could be studied simultaneously by PDA and radiochromatography detection. Assays to study the effects of CYP24A1 point (or double) mutants were conducted at 4 substrate concentrations in parallel with wild-type: 0.30 μM + 1.5×10^5 cpm, 1.5 μM + 1.5×10^5 cpm, 3.5 μM + 1.5×10^5 cpm, and 9.0μM + 1.5×10^5 cpm (incubated for 24 h). Non-transfected MK3 cells and plates devoid of cells, were used as negative controls. At the end of the incubation period, the plates were observed for signs of cell death and contamination.

The metabolism of up to 9 prodrugs or analogs of 1α,25-$(OH)_2D_3$ was studied in up to 20 selected mutant CYP24A1-containing cell lines (Figure 2.3, Table A2.2). The incubation conditions were similar to those described above, with the exception that tritium-labeled analogs were not available, incubations were conducted only at a 9 μM substrate concentration, and that the incubation time was extended from 24 to 36 hours. The selected analogs under investigation included: 20-CH_3-1α,25-$(OH)_2D_3$ (courtesy of Dr. H. Wiesinger; Schering, Berlin, Germany), 20-epi-1α,25-$(OH)_2D_3$, 1α –hydroxydehydrotachysterol$_3$ (1α-OH-DHT_3), 1α,25 –dihydroxydehydrotachysterol$_3$ (1α,25-$(OH)_2DHT_3$) (all courtesy of Drs. M. Calverley and A.-M. Kissmeyer, Leo, Ballerup, Denmark), 16-ene-1α,25-$(OH)_2D_3$ (courtesy of Dr. S. Reddy, Brown University, Providence RI, USA), 1α,25-$(OH)_2D_2$, 1α-hydroxyvitamin-D_2 (1α-OH-D_2), 1α-OH-D_3 (all courtesy of Dr. J. Knutson, Genzyme, Madison WI, USA), (25-hydroxyvitamin-D_3) 25-OH-D_3 (Fluka).

2.8 EXTRACTION OF VITAMIN D METABOLITES

Vitamin D metabolites were extracted from the incubation medium using a modification of the method of Bligh and Dyer [172], where methylene chloride was substituted for chloroform in the extraction procedure described below [173]. The incubation medium was transferred to extraction tubes at the end of the incubation time point. A 5.0 ml amount of methanol was added to the tube, followed by the addition of 2 μg of the internal recovery standard 1α-OH-D_3 or vitamin D_3 (used when 25-OH-D_3 was used as a substrate). Two 2.5 ml aliquots of methylene chloride were subsequently added, with vortexing after the addition of each aliquot. The extraction was completed with the addition of 2.5 ml of a saturated potassium chloride solution. The mixture was vortexed and centrifuged at 1500×*g* for 10 min, in order to achieve

Figure 2.3: Selected vitamin D substrates. The metabolism of selected prodrugs and analogs of 1α,25-$(OH)_2D_3$ were studied in a subset of mutant CYP24A1-expressing cell lines (Table A2.2). Modifications to the structure of 1α,25-$(OH)_2D_3$ are highlighted in red. 1α,25-dihydroxylated analogs are shaded in yellow, whereas prodrug forms lacking either the 25-hydroxyl or 1α-hydroxyl groups are shaded in green or red respectively. Analysis of the metabolism of the tritium-labeled species [1β-^{3}H]1α,25-$(OH)_2D_3$ and [26,27-^{3}H]25-OH-D_3 were also studied. Molecular weights (Mw) of the selected substrates are listed.

optimal separation of the organic and aqueous phases. The organic phase was evaporated to dryness at 37 °C with nitrogen gas, and re-dissolved in 400 µl 100% ethanol and stored at 4 °C, in preparation for HPLC analysis described below. A 500 µl aliquot of the aqueous phase was combined with 5 ml of Ready Flow III liquid scintillation cocktail (Beckman, Fullerton CA, USA), and counted, using a LS 6500 liquid scintillation counter, in order to study the overall conversion of radioactivity into water-soluble metabolites. The remaining aqueous phase was re-extracted with 5 ml of methylene chloride, in the presence of 0.1% (v/v) glacial acetic acid, and the resulting organic phase was dried and stored in 400 µl of 100% ethanol in preparation for reversed-phase HPLC analysis described below. It should be noted that analysis of the aqueous phase was not conducted when metabolism of vitamin D analogs was studied.

2.9 HIGH PERFORMANCE LIQUID CHROMATOGRAPHY

High performance liquid chromatography (HPLC) analysis was conducted using an Alliance 2695 separations module (Waters, Milford MA, USA) connected with a model 996 photodiode array (PDA) detector (Waters) and a LB 509 radio-chromatography detector in-line (Berthold, Carlsbad CA, USA), using HPLC grade solvents (Caledon Laboratories, Georgetown ON, Canada). The organic phase from the Bligh and Dyer extraction described above, was evaporated to dryness at 37 °C under a stream of pre-purified nitrogen and re-dissolved in 115 µl of 91/7/2 (% vol) hexane/isopropanol/methanol (H/I/M). A 5µl amount was combined with 5ml of Ready Flow III liquid scintillation cocktail (Beckman), and counted as described above. The remaining 110 µl was subjected to HPLC analysis using an isocratic solvent system of 91/7/2 H/I/M on Zorbax Sil (3 µm, 6.2×150 mm; Agilent, La Jolla CA, USA) at a solvent flow rate of 1 ml/min (HPLC system A, Table A2.3). Ready Flow III scintillation cocktail was supplied to the radioactivity detector at a rate of 2 ml/min via a LB5035 (Berthold) external HPLC pump. It should be noted that when 25-OH-D_3 was used as a substrate, samples were re-dissolved in 96/3/1 H/I/M and subjected to HPLC analysis using the same solvent as the mobile phase.

The organic phase derived from the aqueous phase re-extract described above, was dried and re-dissolved in 110 µl of 50% acetontirile/water and subjected to reversed-phase HPLC analysis using an acetonitrile (A)/water (W)/ 10% glacial acetic acid (GAA)-based linear gradient solvent system on Zorbax SB-C18 (5 µm, 4.6×150 mm; Agilent). The gradient was started at 69/30/1 (% vol) A/W/10% GAA and

brought to 0/99/1 A/W/10% GAA over 30 minutes, at a flow rate of 1 ml/min (HPLC system B, Table A2.3). Ready Flow III scintillation cocktail was supplied to the radioactivity detector at 3ml/min.

HPLC analysis was conducted in parallel with the following synthetic standards where appropriate: 1α,25-$(OH)_2D_3$, 25-OH-D_3, 24,25-$(OH)_2D_3$, 1α,24,25-$(OH)_3D_3$, tetranor-1α,23-$(OH)_2D_3$, calcitroic acid, and 1α,25-$(OH)_2D_3$-26,23-lactone. An aliquot of the internal standard 1α-OH-D_3 or vitamin D_3 was also run, and compared to the amount of internal standard present in each sample, in order to assess recovery from extraction (see Mathematical and Statistical Treatment of Data). When the tritium (^{3}H-) labeled substrates [1β-^{3}H]1α,25-$(OH)_2D_3$ or [26,27-^{3}H]25-OH-D_3 were used, a 3.0×10^4-6.0×10^4 cpm amount of radioactivity was analyzed on HPLC prior to the samples, and the fraction was collected and subjected to liquid scintillation counting in order to calibrate the peak area measurements taken from the radio-chromatograms. All quantitation of metabolites by HPLC was based upon UV_{265} measurements taken by PDA spectrophotometry, and/or by ^{3}H-measurements taken by in-line radio-chromatography detection (see Mathematical and Statistical Treatment of Data) The putative identity of each metabolite peak was assigned on the basis of a combination of criteria including:

1. The presence of the characteristic vitamin D cis-triene chromophore (λ_{max}=265, λ_{min}=228, UV_{max}/UV_{min}=1.75, ε=18 300).
2. Co-chromatography with synthetic standards.
3. Co-chromatography with metabolites generated from ^{3}H-labeled substrates.
4. Molecular weight, as determined by mass-spectrometry (described below).
5. Sensitivity to sodium m-periodate treatment (described below).

2.10 SODIUM PERIODATE CLEAVAGE AND HIGH PERFORMANCE LIQUID CHROMATOGRAPHY-MASS SPECTROMETRY

Incubation of vitamin D substrates in the appropriate cell lines were repeated without radioactivity, and subjected to HPLC analysis described above. Fractions possessing the characteristic vitamin D cis-triene chromophore were collected, in preparation for liquid chromatography-mass spectrometry (LC-MS) analysis. The fractions containing the putative metabolites 1α,23*S*,25-$(OH)_3D_3$ and 1α,24*R*,25-$(OH)_3D_3$ were treated with sodium m-periodate cleavage prior to the LC-MS analysis. Approximately 800 ng of 1α,23*S*,25-$(OH)_3D_3$ or 1α,24*R*,25-$(OH)_3D_3$ were dried and re-dissolved in 40 μl

methanol. A 20 µl volume of 5% (w/v) sodium periodate (BDH, Poole, UK), was added to each metabolite, vortexed, wrapped in foil, and incubated at room temperature in the dark for 1hr. The reaction products were dried, re-dissolved in 91/7/2 H/I/M and purified by HPLC on Zorbax Sil, as described above. Purified metabolites left untreated treated were used as controls.

Putative catabolic products of 1α,25-$(OH)_2D_3$, 25-OH-D_3, and the products of periodate treated metabolites were dried and re-dissolved in 30 µl 50% (v/v) methanol/water and subjected to LC-MS analysis using an Alliance 2695 separations module connected in-line with a Quattro Ultima triple-quadrupole mass spectrometer (Waters) in electrospray ionization positive mode (ES^+). The initial HPLC analysis was carried out using a linear gradient solvent system starting at 39/60/1 (% v/v/v) water (W)/methanol (M)/1% glacial acetic acid (GAA) in water and brought to 0/99/1 W/M/1 % GAA over 30 minutes (HPLC System C). All of the chromatographic systems used in this thesis are summarized in Table A2.3.

MS1 or scanning ion mode was used to determine the molecular weight of putative metabolite fractions, where all ions within a selected mass/charge (m/z) range of 50-600 were detected over the 30 min duration of the chromatographic run. Mass spectra were combined over the region of the chromatogram corresponding to the elution of the metabolite of interest. In general, the MS1 mass spectra contained several characteristic ions including molecular ions $[M+H]^+$, dehydration products $[M+H-H_2O]^+$, $[M+H-2H_2O]^+$, and adducts, which formed the basis for molecular weight determination. Optimized mass spectrometer settings are listed in Table A2.4 [136]. Fragment ion analysis, and multiple reaction monitoring (MRM) data modes were used to a lesser extent in this thesis. In fragment ion mode, a parent ion was selected from the MS1 analysis for entry into the collision cell for collision-induced dissociation (CID) with argon gas. The instrument was set to scan for fragment ions from m/z 50-450. Typically, a relatively abundant molecular ion $[M+H]^+$ or dehydration product $[M+H-H_2O]^+$ was selected as the parent ion. In MRM mode, the third hexapole was used as a mass filter, to monitor the production of a single selected fragment ion, generated in the collision cell from a single selected parent ion. Typically, a fragment ion corresponding to the dehydration product of a cis-triene cleavage, was selected as ion to be monitored by MRM. It should be noted that the LC-MS settings summarized in Table 2.4 apply to all of

the data acquisition modes, with the exception of the collision energy and the collision gas flow, which were activated only during fragment ion and MRM analysis [136].

2.11 MATHEMATICAL AND STATISTICAL TREATMENT OF DATA

Concentration of DNA. The concentration of DNA preparations (*c*) was determined using Beer's law and UV spectrophotometry, given that a 50μg/ml solution of double stranded DNA in water equals 1 absorbance unit at 260nm (1 A_{260} unit). DNA concentrations were confirmed by agarose gel electrophoresis. A DNA stock solution was considered pure when $A_{260}/A_{280} \geq 1.8$. Concentrated DNA solutions were diluted in water as appropriate to achieve A_{260} readings between 0.1 and 1.

$$c(\mu g \cdot ml^{-1}) = A_{260} \times (\text{dilution factor}) \times 50\ \mu g \cdot ml^{-1}$$

β-galactosidase Specific Activity. Total β-galactosidase activity was expressed as the amount of ONPG hydrolyzed, as determined by OD_{420} readings, given that the final reaction volume was 200μl, and the extinction coefficient is 4500nl/nmol·cm**.**

$$\text{nmol of ONPG hydrolyzed} = OD_{420} \times 2.00 \times 10^5 nl \div 4500 nl/nmol \cdot cm \times 1cm$$

The total protein content of the cell lysates were determined using the method of Bradford, from which the specific activity could be determined. β-galactosidase specific activity was determined in duplicate for 3 volumes of lysate, in order to confirm linearity of the assay.

$$\text{specific activity} = \text{nmol of ONPG hydrolyzed} \cdot \text{mg protein}^{-1} \cdot 30\ \text{minutes}^{-1}$$

Probe Specific Activity. An Ambion DECAprime II random priming kit was used to label the probe used in the Southern blot assay described above. The specific activity of the probe was determined using the following steps:

$$\%\ \text{nucleotide incorporation} = \text{TCA precipitable cpm} \div \text{total cpm} \times 100\%$$

$$\text{Amount of labeled nucleotide incorporated(pmol)} = \%\ \text{nucleotide incorporation} \times \text{vol. isotope(5 μl)} \times [\text{isotope}](10\ \mu Ci/\mu l) \div \text{isotope specific activity (3 μCi/pmol)}$$

The total mass of the synthesized product was determined assuming that the incorporation of all four nucleotides were equal, using the average molecular mass of the nucleotides (330 g/mol).

$$\text{Mass of synthesized product} = \text{amount of labeled nucleotide incorporated(pmol)} \times 330\ g/mol \times 4$$

Total DNA (ng) = Mass of synthesized product + 25 ng template DNA

Probe specific activity = total TCA precipitable cpm·total DNA ng^{-1}

***rtPCR relative quantification*.** Relative mRNA expression levels among the constructs encoding for mutant CYP24A1 proteins were determined using rtPCR, where Ct represents the cycle threshold. All constructs were compared relative to wild-type.

$Ct_{CYP24A1}$-Ct_{GAPDH} = ΔCt

$\Delta Ct_{mutant\ CYP24A1}$ - $\Delta Ct_{wild\text{-}type\ CYP24A1}$=ΔΔCt

Relative quantification(RQ) = $2^{-\Delta\Delta Ct}$

***Concentration of vitamin D compounds*.** The concentration of vitamin D substrates and standards were determined using Beer's law and spectrophtometry, based upon the molar extinction coefficient (ε) of 18 300, taken at λ_{max}=265 nm. The path length b=1 cm, and the concentration and absorbance are denoted by *c* and *A* respectively. The molecular weight of the compound of interest is denoted by Mw:

***c*(mg·ml^{-1}) = A_{265}×(dilution factor)÷18 300 M^{-1}cm^{-1}×1cm×Mw (g·mol^{-1})**

Quantitation of PDA-based HPLC data. The amount of a metabolite was based upon the area units (AU) under the HPLC peak at 265 nm, using the experimentally-determined conversion factor 2178 AU_{265}·min^{-1}·ng at a flow rate of 1 ml/min.

Amount of metabolite (ng)=AU_{265} ÷ 2178 AU_{265}·min·ng^{-1}·ml^{-1} × 1ml·min^{-1}

Quantitation of ^{3}H-based HPLC data. The amount of ^{3}H-labeled metabolite was based upon the area units under the HPLC peak (mV), which was calibrated by determining the amount of radioactivity in a collected fraction of known AU (AU·dpm^{-1}) denoted by the conversion factor C, and given the specific activity of the isotope (dpm·ng^{-1}), denoted by S. The value of C was determined prior to each sample set, and varies depending on the solvent system used due to quenching. PDA and mV peaks were integrated manually at the base of each peak, where a baseline-drop option was selected to estimate the area under the curve measurements for peaks that were not completely resolved. All chromatography and peak integration was completed using the Empower chromatography manager (Waters).

Amount of metabolite (ng) = C AU_{mv}·dpm^{-1}× S dpm·ng^{-1}

Recovery from extraction. The synthetic compounds 1α-OH-D_3 or vitamin D_3 was added to the incubation samples prior to extraction as an internal standard used to assess recovery from extraction (IS_{added}). Metabolite quantities were corrected for recovery by normalizing the amounts to the internal standard, based upon the amount of internal standard recovered ($IS_{recovered}$).

corrected amt. of metabolite = IS_{added} ÷ $IS_{recovered}$ ×amt. of metabolite

The relatively small amount of metabolites in the aqueous phase were not corrected for recovery since the internal standards are lipid soluble and are not observed in the HPLC analysis of the aqueous phase re-extracts.

Total CYP24A1 Activity. A weighted summation approach [174] was used to estimate CYP24A1 total enzyme activity based upon the amounts of metabolite detected on HPLC. The amounts of individual metabolites detected were weighted for their relative position in the C24 or C23 hydroxylation pathway, and added together, as shown below for the C24 and C23 pathways:

$CYP24A1_{C24}$ activity = 1α,24,25-$(OH)_3D_3$+[2×24-oxo-1α,25-$(OH)_2D_3$]+[3×24-oxo-1α,23,25-$(OH)_3D_3$]+[4×tetranor-1α,23-$(OH)_2D_3$]+[5×calcitroic acid] pmol·2.4×$10^6$$cells^{-1}$·$24h^{-1}$

$CYP24A1_{C23}$ activity = 1α,23,25-$(OH)_3D_3$+[2×1α,23,25,26-$(OH)_4D_3$]+[3×1α,25-$(OH)_3D_3$-23,26-lactol] +[4×1α,25-$(OH)_3D_3$-23,26-lactone] pmol·2.4×$10^6$$cells^{-1}$·$24h^{-1}$

Total CYP24A1 activity = $CYP24A1_{C24}$ activity + $CYP24A1_{C23}$ activity

Catabolic pathway preference of the mutant CYP24A1 proteins under investigation is given by:

CYP24A1 activity ratio = **$CYP24A1_{C24}$ activity÷ $CYP24A1_{C23}$ activity**

Statistical Analysis. Amounts of individual metabolites, total activities, and activity ratios were determined from triplicate HPLC chromatograms, and expressed as the mean. Experimental variability is expressed as the standard error of the mean (SEM). Where necessasy, statistical significance was determined by the Student's t-test application in Prism (GraphPad Software Inc, La Jolla, CA, USA)

CHAPTER 3: Ala326 IS A CRITICAL DETERMINANT OF CYP24A1 REGIOSELECTIVITY

3.1 INTRODUCTION

CYP24A1 is a multi-catalytic enzyme [108], capable of catalyzing all of the steps in each of two degradatory pathways commencing with either C24- or C23-hydroxylation of 1α,25-$(OH)_2D_3$, which culminates in either calcitroic acid [104,175] or 1α,25-$(OH)_2D_3$-26,23-lactone respectively [110,176,177]. The physiological role of CYP24A1 is to attenuate the 1α,25-$(OH)_2D_3$ biological signal by catalyzing the degradation of 1α,25-$(OH)_2D_3$ in an inducible manner in vitamin D target cells [96]. Because the identification of some of the key catabolites of 25-OH-D_3, namely 24*R*,25-$(OH)_2D_3$ [93,178] and 23*S*,25-$(OH)_2D_3$ [179], predated confirmation of the specific involvement of CYP24A1 in their formation, it remained unclear that a single enzyme was responsible for C24- and C23-hydroxylase activity towards 25-OH-D_3. In the mid 1980s, it was shown that 24- and 23-hydroxylase activities co-purified, and that the production of 24*R*,25-$(OH)_2D_3$ and 23*S*,25-$(OH)_2D_3$ in kidney mitochondria was induced when the animals were pre-treated with 1α,25-$(OH)_2D_3$ [180]. This result implied that a single 1α,25-$(OH)_2D_3$-inducible enzyme could be responsible for the previously reported C24- and C23-hydroxylase activities, which by the late 1980's, were recognized to comprise only the first of 5 or 4 steps in the respective C24 and C23-hydroxylation pathways [104,110,175-177]. The definitive answer came with the cloning of CYP24A1 in the early 1990's from different species [105,181,182], which opened up the possibility of studying CYP24A1 activity in isolation, which led to the conclusion that CYP24A1 can indeed catalyze the catabolism of 25-OH-D_3 via C24- and C23-hydroxylation. This observation was confirmed more recently at the physiological level, when primary keratinocytes cultured from CYP24A1-null mice were found to lack the ability to convert 1α,25-$(OH)_2D_3$ to either calcitroic acid or 1α,25-$(OH)_2D_3$-26,23-lactone [117]. The degree to which CYP24A1 catabolizes its substrate via either C24 or C23-hydroxylation is species dependent, with rat CYP24A1 almost exclusively preferring the C24 pathway [183,184], and guinea pig CYP24A1 preferring the C23 pathway [111,185]. Even though human CYP24A1, the focus of this thesis, prefers the C24 pathway, some degradation of substrate proceeds through the C23 pathway.

We set out to identify the molecular determinants of the C24 and C23-hydroxylation activity of human CYP24A1 by (1) surveying the catabolism of 1α,25-$(OH)_2D_3$ in several cultured cell models containing different species of CYP24A1 showing extremes of either C24- or C23-hydroxylation (2)

comparing the amino acid sequences among different CYP24A1 species and evaluating their importance in effecting the observed regioselectivity differences within the context of a homology model of human CYP24A1 and (3) conducting site-directed mutagenesis at predicted substrate-contact points and studying the effect of the mutations on CYP24A1 activity using transient and stable transfection systems.

3.2 RESULTS

3.2.1 CATABOLISM OF 1α,25-$(OH)_2D_3$ AND 25-OH-D_3 IN CULTURED CELL MODELS OF CYP24A1

We selected several cell lines including LLCPK1 (pig), HEK-293 (human), OK (opossum), HPKA1-ras (human) and V79-CYP24 (Chinese hamster cells containing human CYP24A1)(Table 2.1) in which to study the catabolism of 1α,25-$(OH)_2D_3$ and 25-OH-D_3 in order to identify any species-based differences in CYP24A1 activity among these common cell lines. The cell lines LLCPK1, HEK-293, HPK1A-ras, and V79-CYP24 were all observed to catabolize 1α,25-$(OH)_2D_3$ and 25-OH-D_3 via mainly the C24-hydroxylation pathway, however, OK cells, containing opossum CYP24A1, was found to catabolize the selected substrates via the C23-hydroxylation pathway (data not shown). The OK and V79-CYP24 cells were selected as examples of C23- and C24-hydroxylating CYP24A1 homologs, and cell culture and incubation conditions were optimized in order to study the extremes of catabolic pathway preference in more detail.

When the catabolism of 1 μM 1α,25-$(OH)_2D_3$ was studied in the presence of a tritiated tracer, 0.003 μM [1β-^{3}H]1α,25-$(OH)_2D_3$ in V79-CYP24 cells (Figure 3.1 A), the major metabolites observed included the terminal pathway products tetranor-1α,23-$(OH)_2D_3$ (peak 5) and calcitroic acid (peak 6, aqueous phase chromatography not shown) in the C24-hydroxylation pathway, and 1α,25-$(OH)_2D_3$-26,23-lactone (peak 10) in the C23-hydroxylation pathway. When the catabolism of 10 μM 1α,25-$(OH)_2D_3$ was studied (Figure 3.1 A), the proximal C24 pathway intermediates were maximally produced, including 1α,24*R*,25-$(OH)_3D_3$ (peak 2) 24-oxo-1α,25-$(OH)_2D_3$ (peak 3) and 24-oxo-1α,23,25-$(OH)_3D_3$ (peak 4), noting that relatively minor amounts of tetranor-1α,23-$(OH)_2D_3$ were detected at this condition. In the C23 pathway, the only product observed was 1α,23*S*,25-$(OH)_3D_3$ (peak 7). Given the relatively low amounts of

1α,23*S*,25-$(OH)_3D_3$ observed at 10 μM or 1α,25-$(OH)_2D_3$-26,23-lactone observed at 1 μM, it appeared that the C24 pathway was the preferred route of catabolism by the human enzyme. A similar pattern of catabolism was observed for 25-OH-D_3 (Figure 3.2 A), except that the analysis was somewhat limited by the lack of radioactivity of the metabolites tetranor-23-OH-D_3 (peak 5a) and calcioic acid (peak 6a, aqueous phase chromatography not shown) due to the loss of the [26,27-^{3}H] label during the side-chain cleavage step. Three approaches were used to express pathway preference as a C24/C23 hydroxylation ratio (Table 3.1), including (1) simply taking the ratio of 1α,24*R*,25-$(OH)_3D_3$ (peak 2)/ 1α,23*S*,25-$(OH)_3D_3$ (peak 7) (or peak 2a/7b) at 10μM, (2) taking the ratio of the total amount of product detected in each pathway, or (4) in a manner similar to (2) except that the amount of each individual product is weighted for its relative position in the pathway, in order to estimate the total enzyme activity. Over the assay conditions and calculations used, the C24/C23 ratios ranged from 6.66-24.19 in V79-CYP24 cells when 1α,25-$(OH)_2D_3$ was used as a substrate and 2.82-8.09 when the catabolism of 25-OH-D_3 was considered (Table 3.1)[186]. Interestingly, it appeared as though 25-OH-D_3 had a 2.4-fold greater capacity to be C23-hydroxylated by human CYP24A1, as determined from the peak 2a/7b ratios. This information could not be gleaned from the total product or total activity ratios, since the values were confounded by the lack of radioactivity associated with the side-chain cleaved products of 25-OH-D_3 (Table 3.1). Furthermore, 23,25-$(OH)_2D_3$ (peak 7b) seemed to give rise to a minor amount of 23-oxo-25-OH-D_3 (peak 7c), of which an analogous 1α-hydroxylated product was not detected.

When the catabolism of 0.5 μM 1α,25-$(OH)_2D_3$ was studied in OK cells (Figure 3.1C), the major metabolite observed was determined to be 1α,25-$(OH)_2D_3$-26,23-lactone (peak 10), with a minor amount of calcitroic acid in the aqueous phase, suggesting that the C23 pathway is the major 1α,25-$(OH)_2D_3$ degradatory route for opossum CYP24A1 [186]. This observation was confirmed at 5 μM 1α,25-$(OH)_2D_3$ where the proximal C23-pathway intermediate 1α,23*S*,25-$(OH)_3D_3$ (peak 7) dominated the chromatogram (Figure 3.1C), as opposed to 1α,24*R*,25-$(OH)_3D_3$ (peak 2) in V79-CYP24 cells containing human CYP24A1 (Figure 3.1A). This striking shift in regioselectivity was also observed when 25-OH-D_3 was used as a substrate (Figure 3.2C), where 25-OH-D_3-26,23-lactone (peak 10a) and 23,25-$(OH)_2D_3$ (peak 7a) were the major catabolites at 0.5 and 5μM 25-OH-D_3 respectively, similar to the metabolites previously detected in OK cell extracts by Yamada's laboratory [166]. In V79-CYP24 cells we noted that between the

proximal pathway oxo-containing metabolites, 24-oxo-25-OH-D_3 (3a) was a major component, and 23-oxo-25-OH-D_3 (7c) was the minor component, since these products were likely formed from 1α,24*R*,25-$(OH)_3D_3$ and 1α,23*S*,25-$(OH)_3D_3$ respectively. However, in the context of the C23-hydroxylating opossum CYP24A1, 23-oxo-25-OH-D_3 (7c) formed the major component when compared to 24-oxo-25-OH-D_3 (3a) (Figure 3.2C). We quantitated the regioselectivity of opossum CYP24A1 using the various formulae, which gave C24/C23 ratios ranging from 0.04-0.44 for 1α,25-$(OH)_2D_3$, as compared to 6.66-24.19 for human CYP24A1, or 0.01-0.1 for 25-OH-D_3, as compared with 2.82-8.09 for human CYP24A1 (Table 3.1); corresponding to a 14-600-fold change in regioselectivity between human and opossum CYP24A1 for 1α,25-$(OH)_2D_3$ or a 28-809-fold change for 25-OH-D_3. Other investigators have recently focused on studying the regioselectivity differences between human and rat CYP24A1 (almost exclusively a C24-hydroxylase), and have reported a C23/C24 hydroxylation ratio of 0.01 (equivalent of a C24/C23 ratio of 100) for rat CYP24A1 or 0.27 (C24/C23 ratio of 3.7) for the human enzyme, when 1α,25-$(OH)_2D_3$ was used as a substrate [112].

3.2.2 CATABOLISM OF 1α,25-$(OH)_2D_3$ AND 25-OH-D_3 BY Ala326Gly-MODIFIED CYP24A1

A CYP24A1 sequence alignment analysis (Conducted by Dr. David Prosser) revealed that human CYP24A1 differed from the South American opossum, *Monodelphis domesticus*, at only 80 amino acids. Within the context of a CYP24A1 homology model, 30 of the differences were immediately ruled out as potential determinants of the regioselectivity differences between the human and opossum CYP24A1s, since they are located in the highly variable membrane-binding region at the N-terminus [186]. We focused specifically on 'oposumizing' three residues in human CYP24A1 including N448H, and Q471H, and A326G since they were possible substrate-contact residues in the homology model which, when mutated, could potentially alter the regioselectivity of human CYP24A1 [186].

We tested this hypothesis by transiently transfecting the mutant cyp24a1-containing constructs into V79-4 cells, and incubating the cells with 1α,25-$(OH)_2D_3$ or 25-OH-D_3 using similar assay conditions to those presented above, except the substrate concentration was reduced to either 0.003 μM ([1β-^{3}H]1α,25-$(OH)_2D_3$/[26,27-^{3}H]25-OH-D_3 only) or 0.750 μM (including 0.003 μM [1β-^{3}H]1α,25-$(OH)_2D_3$/[26,27-^{3}H]25-OH-D_3) to attempt to achieve a similar distribution of products observed in the cell

line studies, using the inherently lower expression levels associated with transient transfection. The wild type-containing V79-4 cells gave very similar patterns of metabolism to those observed in V79-CYP24 cells, with either substrate (Figure 3.1B as compared with A; or Figure 3.2B as compared with A), giving C24/C23 ratios ranging from 6.17-8.69 for 1α,25-$(OH)_2D_3$ or 3.70-4.89 for 25-OH-D_3 (Table 3.1). A predictably dissimilar level of CYP24A1 expression and a compensatory reduction in total substrate concentration resulted in a dramatically reduced total enzyme activity (not shown), however, monitoring the fixed amount of tritiated tracer permitted an almost identical distribution of products between human wild-type CYP24A1 either stably or transiently expressed in V79-4 cells, which could not have been measured by UV_{265} measurements alone at all of the substrate concentrations studied. When metabolism by N448H, and Q471H were studied, identical CYP24A1 activities and distribution of products were observed as compared with wild type (not shown), suggesting that these two residues are not responsible for the regioselectivity difference observed between human and opossum CYP24A1 [186].

When the catabolism of 1α,25-$(OH)_2D_3$ by A326G was studied, we observed a remarkable preference for catabolism via the C23-hydroxylation pathway. The organic phase chromatograms were characterized by 1α,25-$(OH)_2D_3$-26,23-lactone (peak 10) and a minor amount of tetranor-1α,23-$(OH)_2D_3$ (peak 5) at 0.003 μM, and mainly 1α,23,25-$(OH)_3D_3$ (peak 7) at 0.750 μM (Figure 3.1D), with an analogous pattern of metabolism observed for 25-OH-D_3 (Figure 3.2D). Furthermore, the pattern of metabolism observed in the A326G-containing cells strikingly resembled that observed in OK cells for both 1α,25-$(OH)_2D_3$ (Figure 3.1C) and 25-OH-D_3 (Figure 3.2C). The hydroxylation ratios for A326G ranged from 0.11-0.57 for 1α,25-$(OH)_2D_3$ (as compared with 0.04-0.44 in OK cells) or 0.05-0.1 (as compared with 0.01-0.1 in OK cells)(Table 3.1), representing a 20-74-fold change in ratio for 1α,25-$(OH)_2D_3$ or a 52-98-fold change for 25-OH-D_3. This result suggested that Ala326 is a major determinant of the regioselectivity difference observed between human and opossum CYP24A1 [186].

We went on to generate V79-4-based stable cell lines containing the human wild-type and the A326G-mutated enzyme using the Flp-In stable transfection system to facilitate a more quantitative comparison between these enzymes (see Chapter 2.2-2.6; Figure 2.1). Metabolism of 1α,25-$(OH)_2D_3$ was studied in the wild-type and A326G cells over four substrate concentrations 0.3, 1.5, 3.5 and 9 μM, each containing a fixed amount (0.003 μM [1β-^{3}H]1α,25-$(OH)_2D_3$)(Figure 3.3). The superior CYP24A1

expression levels of the stable cell lines facilitated the use of higher substrate concentrations to achieve some of the same metabolite distributions observed in the transient transfection assays, permitting UV_{265}, in addition to ^{3}H measurements to be taken for most of the metabolites detected (Table 3.2). For the wild-type enzyme at 0.3 μM, tetranor-1α,23-$(OH)_2D_3$ (peak 5) was the major product (Figure 3.3A) and calcitroic acid was maximally produced (Table 3.2). At 1.5 μM, there was a slight increase in the relative amount of tetranor-1α,23-$(OH)_2D_3$ detected at the expense of calcitroic acid in the aqueous phase (chromatography not shown; see Table 3.2), and a minor amount of the preceding intermediate, 24-oxo-1α,23,25-$(OH)_3D_3$ (peak 4) was observed. The 3.5 μM concentration point (panel E) was characterized by accumulation of the more proximal pathway intermediates 24-oxo-1α,23,25-$(OH)_3D_3$ (peak 4), 24-oxo-1α,25-$(OH)_2D_3$ (peak 3) and 1α,24,25-$(OH)_3D_3$ (peak 2), and at 9 μM (panel G), the major components were unreacted 1α,25-$(OH)_2D_3$ (peak 1) and the initial pathway products 1α,24,25-$(OH)_3D_3$ (peak 2) and 24-oxo-1α,25-$(OH)_2D_3$ (peak 3). The relative amounts of each product is plotted over the various assay conditions in Figure 3.4A. At each substrate concentration point, the C23 pathway intermediates represented a minor component of the total amount of product, as plotted in Figure 3.4C, where at 9 μM, 91 and 9% of the total product were C24 or C23 pathway products respectively (C24/C23 activity ratio of 8.9; Table 3.2). When A326G was considered, 1α,25-$(OH)_2D_3$-26,23-lactone (peak 10) was the major product at 0.3 μM (Figure 3.3B). At 1.5 μM (panel D), the penultimate C23 pathway product, 1α,25-$(OH)_2D_3$-26,23-lactol (peak 9), was maximally produced, in addition to the accumulation of 1α,23,25-$(OH)_3D_3$ (peak 4), which formed the major product at 3.5 and 9 μM (panels F&H). Also, the metabolite 23-oxo-1α,25-$(OH)_2D_3$ (peak 7a) became maximally produced at 3.5-9 μM. The distribution of the products over the substrate concentrations tested is plotted in Figure 3.4B. Consistent with the transient transfection assay [186], A326G preferred the C23-hydroxylation pathway as the main catabolic route, where at 9 uM, 5 and 95% of the total products were C24 or C23 pathway products respectively (C24/C23 activity ratio of 0.03), as compared to 91 and 9% (ratio of 8.9) for the wild type, representing a complete switchover between characteristic human and opossum CYP24A1 activities resulting from a single A326G mutation. The stable cell line work enabled us to purify enough material to characterize peaks 7a and 9 (determined to be 23-oxo-1α,25-$(OH)_2D_3$ and 1α,25-$(OH)_2D_3$-26,23-lactol), which were detected but could not be

Figure 3.1: Comparative metabolism of 1α,25-$(OH)_2D_3$ in V79-CYP24, OK, and transiently transfected V79-4 cells. Optimized substrate concentrations were used to study the metabolism of 1α,25-$(OH)_2D_3$ in V79-CYP24 cells (A; 10 μM, or 1 μM) and V79-4 cells transiently transfected with human wild-type CYP24A1 (B, 0.750 μM or 0.003 μM). Patterns of metabolism were compared to those observed in OK cells (C; 5μM, or 0.500 μM) and V79-4 cells transiently transfected with A326G-modified CYP24A1(D; 0.750 μM or 0.003 μM). Triplicate chromatograms are overlayed on each plot. The aqueous phase chromatography is not shown. The chromatography work in this figure delineates the different routes of catabolism of 1α,25-$(OH)_2D_3$ exhibited by the wild type CYP24A1 (C24) as compared with opossum & A326G-modified CYP24A1 (C23). The pathway scheme emphasizes the analagous catabolic routes for both 1α,25-$(OH)_2D_3$ (Figure 3.2) and 25-OH-D_3. The regioselectivity differences among the CYP24A1-containing cells compared in this figure are presented in Table 3.1.

Figure 3.2: Comparative metabolism of 25-OH-D_3 in V79-CYP24, OK, and transiently transfected V79-4 cells. Optimized substrate concentrations were used to study the metabolism of 25-OH-D_3 in V79-CYP24 cells (A, 10 μM, or 1 μM) and V79-4 cells transiently transfected with human wild-type CYP24A1 (B; 0.750 μM or 0.003 μM). Patterns of metabolism were compared to those observed in OK cells (C; 5μM, or 0.500 μM) and V79-4 cells transiently transfected with A326G-modified CYP24A1(D, 0.750 μM or 0.003 μM). Triplicate chromatograms are overlayed on each plot. The aqueous phase chromatography is not shown. The pathway scheme emphasizes the analagous catabolic routes for both 1α,25-$(OH)_2D_3$ (Figure 3.1) and 25-OH-D_3. The regioselectivity differences among the CYP24A1-containing cells compared in this figure are presented in Table 3.1. Peak 7c, identified as 23-oxo-25-OH-D_3, is not shown on the catabolic pathway scheme.

characterized in the transient transfection experiments (21.5 & 27.2 min peaks in Figure 3.1D respectively).

The wild type gave a total enzyme weighted activity measurement of 2580 pmol/2.4×10^6 cells/24 h, whereas A326G gave a measurement of 560 pmol/2.4×10^6 cells/24 h, corresponding to 21% of the total wild-type activity at 9 μM (Table 3.2), suggesting that A326G caused a reduction in total enzyme activity, in addition to a drastic change in regioselectivity. Some of the difference in total activity may have been due to differences in expression levels between the two enzymes, since A326G gave a relative quantification of 0.438 on rtPCR (relative to the wild type, 1.000)(Table A2.2). However, it should be noted that all three expression systems including established cell lines (V79-CYP24 vs. OK), the transient and stably transfected cells, showed reduced enzyme activities when opossum CYP24A1 or A326G were compared to the human wild type enzyme (27, 47 and 21% respectively), and exhibited similar changes in regioselectivity (Table 3.2), suggesting that the metabolic patterns observed are mainly the result of the type of cyp24a1 expressed, and not the differences in transfection/*in situ* cell system or assay condition used.

The residues alanine and glycine are conserved in 58 and 42% of the 31 CYP24A1 sequences considered, where glycine is present at position 326 in 3 species of opossums (Figure 3.5A), and guinea pig, reported by our group and others [166,186], as preferentially C23-hydroxylating 25-OH-D_3 or 1α,25-$(OH)_2D_3$. It remains to be seen whether other species of CYP24A1 containing glycine at position 326, including xenopus, lamprey and seven species of bony fish, also preferentially C23-hydroxylate vitamin D substrates, as opposed to human, rat, pig and mouse [180], containing alanine at position 326 [186], which have been determined to preferentially C24 hydroxylate vitamin D substrates. In a study of the regioselectivity differences between human and rat CYP24A1, Hamamoto *et al*., mutated the rat residues Thr416 and Ile500 to the corresponding residues in human [112], T416M and I500T, and observed only a modest change from their reported C23/C24 hydroxylation ratio in the rat (ratio 0.01) towards the human (0.27), where the mutants gave ratios of 0.08 and 0.16 respectively. Also, since these residues did not differ consistently between human and other species, it was unlikely the amino acid differences at positions 416 and 500 were the major sources of the regioselectivity differences reported between human and rat CYP24A1 [186]. Ala326 is located in the centre of the I-helix, and abuts the 25-hydroxylated side-chain of 1α,25-$(OH)_2D_3$ in a homology model of CYP24A1, with a distance of 4.00 Å between from the Ala326

methyl carbon in the wild-type enzyme and the C26, and a distance of 3.55 Å between the C24*R*-hydrogen and the heme iron (as compared to 5.2 Å for the C23*S*-hydrogen)(Figure 3.5B)[186]. Carbon 24 of the 1α,25-$(OH)_2D_3$ molecule was docked in the CYP24A1 model based upon the average heme-triangulated position of hydroxylation susceptible carbons (substrates) and heme-ligating atoms (from inhibitors) determined from 67 crystal structure of cytochrome P450s [186]. Alternatively, based upon our experimental results, we docked C23 into a model of CYP24A1, containing the A326G substitution, placing the C23*S*-hydrogen 3.95 Å from the heme iron (as compared to 6.10 Å for the C24*R*-hydrogen), and C26 only 3.48 Å from the Gly326 α-carbon (Figure 3.5C). We interpret this result to suggest that Ala326 abuts the side-chain of 1α,25-$(OH)_2D_3$, and controls the depth of penetration of the side-chain into the substrate-binding pocket, such that a substitution with Gly permits the side chain to slide further into the pocket, placing the C23*S* hydrogen, rather than the C24*R*-hydrogen into an optimal position for hydroxylation [186].

3.2.3 CHARACTERIZATION OF THE CATABOLITES OF 1α,25-$(OH)_2D_3$ AND 25-OH-D_3

The identities of the peaks in the chromatography analysis described above, have been assigned using a combination of criteria, including (1) possession of the characteristic vitamin D cis triene chromophore, (2) the presence of a corresponding ^{3}H-peak, (3) co-chromatography with synthetic standards & relative retention times on multiple chromatographic systems (4) sensitivity to sodium m-periodate treatment and (5) characteristic ions on LC-MS, as summarized in Table 3.3.

The most basic criteria used for the identification of an HPLC peak as a *de facto* product of 25-OH-D_3 or 1α,25-$(OH)_2D_3$ is that the peak must contain the characteristic vitamin D chromophore (indicated in Table 3.3 as a retention time using UV_{265}) and/or an equivalent peak on the ^{3}H-radiochromatograms, corresponding to the parallel metabolism of *in situ* ^{3}H-labelled [1β-^{3}H]1α,25-$(OH)_2D_3$/[26,27-^{3}H]25-OH-D_3 tracers, which gave retention times of approximately 1-1.4 minutes after the UV_{265} peak due to the serial connectivity of the detectors. In some instances UV_{265} could not be used to directly identify the peak as a specific product, due to low amounts of substrate added (0.003 or 0.750μM in the transient transfection work), however the ^{3}H-peak could be compared to the chromatography from the cell lines studied in which 5-10 μM substrate was used, which gave co-migrating UV_{265} peaks. Most of the metabolites in the stable

cell line studies however, gave both UV_{265} and ^{3}H-peaks (Table 3.2). Alternatively, some metabolites, such as metabolites 8a and 9a were devoid of radioactivity due to the position of the tritium label, hence ^{3}H-chromatography could not be used as a criterion to identify these peaks as specific products (Table 3.2). Characteristic retention times on multiple chromatographic systems (Tables 2.1, Table 3.3) also helped to predict the identity of the products based on comparisons to previous work, facilitated by the availability of some synthetic standards, namely 1α,24*R*,25-$(OH)_3D_3$ and tetranor-1α,23-$(OH)_2D_3$.

LC-MS was used to help identify the various catabolites on the basis of molecular weight. Fractions containing the metabolite under investigation were collected using HPLC Systems A or B, and re-ran on HPLC System C, prior to direct injection into a triple quadrupole mass spectrometer (Table A2.3). The chromatography component, although providing less resolution than HPLC System A, provided an additional characteristic retention time, as well as a confirmation of UV spectral properties, prior to mass spectrometry. For each metabolite studied, the mass spectra gave a combination of characteristic ions including molecular ions $[M+H]^+$, dehydration products $[M+H-H_2O]^+$, $[M+H-2H_2O]^+$, and adducts $[M+Na]^+$, and $[M+NH_4]^+$, from which the molecular weight could be discerned, which matched the predicted molecular weight for each metabolite. The mass spectra for 1α,25-$(OH)_2D_3$ and its products are shown in Figure 3.6, and major characteristic ions detected for 1α,25-$(OH)_2D_3$, 25-OH-D_3 and their products are summarized in Table 3.3. In each case, the changes in the m/z ratios of the characteristic ions between metabolites matched the difference in molecular weight between the metabolites considered, for example 1α,25-$(OH)_2D_3$ (Mw 416) gave the characteristic ions m/z 417, 399, 381, 439, and the putative 1α,24*R*,25-$(OH)_3D_3$ (Mw 432) gave the ions m/z 433, 415, 397, 455 – all differing by 16, the difference in molecular weight between 1α,25-$(OH)_2D_3$ and 1α,24*R*,25-$(OH)_3D_3$. The presence of multiple characteristic ions for each metabolite, served as a 'mass fingerprint', which proved to be critical for ruling out contaminants possessing the same molecular weight as the metabolite of interest. For example, a spectrum containing a single m/z 361 ion, might be interpreted as tetranor-1α,23-$(OH)_2D_3$ (Mw 360), but the knowledge that products of 1α,25-$(OH)_2D_3$ give other ions on LC-MS (including the standards), would result in assigning the m/z 361 ion as a contaminant, in addition to considering the UV spectral properties.

Figure 3.3: Comparative metabolism of 1α,25-$(OH)_2D_3$ in V79-4 cells stably transfected with wild-type or A326G-modified hCYP24A1. V79-4-based stable cell lines were generated to facilitate a more quantitative comparison between wild-type CYP24A1(A,C,E,G) and A326G (B,D,F,H). The cell lines were incubated with four 1α,25-$(OH)_2D_3$ substrate concentrations (A,B;0.3, C,D;1.5, E,F;3.5, G,H; 9 μM). Note that on panels B,D,F and H, the wild-type and A326G chromatograms are displayed on the same plot to facilitate comparison between the chromatograms. The triplicate chromatograms are shown in each case. The aqueous phase chromatography is not shown. A quantitative analysis of the chromatography shown in this figure is presented in Table 3.2.

Peak identities:

1: 1α,25-$(OH)_2D_3$
2: 1α,24,25-$(OH)_3D_3$,
3: 24-oxo-1α,25-$(OH)_2D_3$,
4: 24-oxo-1α,23,25-$(OH)_3D_3$
5: tetranor-1α,23-$(OH)_2D_3$
7: 1α,23,25-$(OH)_3D_3$
7a: 23-oxo-1α,25-$(OH)_2D_3$
9: 1α,25-$(OH)_2D_3$-26,23-lactol
10: 1α,25-$(OH)_2D_3$-26,23-lactone.

Figure 3.4: Substrate concentration-dependent distribution of the products of 1α,25-$(OH)_2D_3$. The relative amounts of the individual products of the C24- and C23-hydroxylation pathways for the wild-type or the A326G mutant are plotted in panels A and B in order to highlight the flux from initial to terminal pathway products as the substrate concentration is decreased. The relative amounts of the various metabolites are expressed as a percentage of the total amount of product, however the substrate 1α,25-$(OH)_2D_3$, is expressed as the percentage of remaining 1α,25-$(OH)_2D_3$. The distribution of the total product in either pathway is presented in panels C and D. The colour-coded traces in panels A and B are defined in the reaction scheme, with the exception of peak 7a, identified as 23-oxo-1α,25-$(OH)_2D_3$.

Figure 3.5: Multi-sequence alignment and homology modeling analysis of wild-type and A326G-modified hCYP24A1. The location of residue 326 is indicated in the sequence alignment of the I-helix (residues 312-345) of selected CYP24A1 orthologs (A). In a homology modeling analysis, the structure of the substrate-binding cavity was compared between 1α,25-$(OH)_2D_3$ docked in an optimal orientation for either C24-hydroxylation (B) in the wild-type containing Ala326, with that docked in A326G optimized for C23-hydroxylation (C) [186]. We interpret this result to suggest that substitution of Ala with Gly at position 326 permits the side chain of 1α,25-$(OH)_2D_3$ to enter more deeply into substrate-binding pocket, positioning C23 instead of C24 above the heme for hydroxylation [186]. The sequence alignment and homology modeling work was conducted by Dr. David Prosser.

The limited ability of LC-MS to differentiate between isomers of identical molecular weight, resulted in the need to employ other techniques to conclusively identify peaks 2 and 7 as 1α,24*R*,25-$(OH)_3D_3$, 1α,23*S*,25-$(OH)_3D_3$, the initial products of the C24- and C23-hydroxylation pathways respectively. The scanning MS1 mass spectra from peaks 2 and 7 are plotted in Figure 3.7A and B, and highlight the major characteristic ions m/z 433, 415, 397 and 455. The spectra are qualitatively identical, with the exception of the ions m/z 359, 341, 322 detected for peak 7, which most likely corresponds to in-source fragmentation between C23 and C24 (in addition to subsequent dehydration products), which possesses the expected m/z ratio for a fragment containing a hydroxyl group at C23, as observed previously by Horst's group [176]. These structurally-informative ions were not observed in the fragment ion spectra (panels C&D), based on collision-induced dissociation using the primary dehydration products m/z 415 from either peaks 2 or 7 as the parent ion, yielding a common cis-triene cleavage fragment of m/z 135. Alternatively, we opted to treat the fractions with sodium m-periodate, which cleaves vicinal diols, including 1α,24*R*,25-$(OH)_3D_3$ (panels G & H, untreated controls panels E & F). Since peak 2 gave a mass spectrum containing a molecular ion of m/z 373 corresponding to a 24-carbon aldehyde (indicating cleavage), and the spectrum for peak 7 remained unchanged after periodate treatment indicating that the hydroxyls were not vicinal, we concluded that peak 7 was 1α,23*S*,25-$(OH)_3D_3$. Also, downstream C23-pathway products of 1α,23*S*,25-$(OH)_3D_3$ including 23-oxo-1α,25-$(OH)_2D_3$ (peak 7a), and 1α,25-$(OH)_2D_3$-26,23-lactol (peak 9) possessed identical molecular weights, and characteristic ions as 24-oxo-1α,25-$(OH)_2D_3$ and 24-oxo-1α,23,25-$(OH)_3D_3$ in the C24 pathway respectively, and required identification partially based upon metabolic context. For example, peak 8 was identified as a lactol, since it was often detected in the same chromatograms as the lactone (possessing a unique molecular weight), and peak 7a was identified as 23-oxo-1α,25-$(OH)_2D_3$, since it was detected in maximal amounts when 1α,23*S*,25-$(OH)_3D_3$ (confirmed by LC-MS and periodate treatment) was abundant. It should be noted that peaks 7a and 9 possessed distinct retention times on HPLC system A (Table 3.3). Peak 8, identified as 1α,23,25,26-$(OH)_4D_3$ (Table 3.3, Figure 3.6) was detected only in scaled-up preparations of metabolites for LC-MS analysis, and not in the analytical-scale assays, suggesting that it was only a minor component under the selected assay conditions. No analogous metabolite was detected when 25-OH-D_3 was used as a substrate (denoted as peak 8a). It should be noted that sufficient amounts of calcitroic acid could not be purified for LC-MS analysis in this study. The mass

spectrum of calcitroic acid presented in Figure 3.6 and listed in Table 3.3, is a representative spectrum acquired from incubations using V79-CYP24 cells.

3.3 SUMMARY

CYP24A1 catalyzes the degradation of 1α,25-$(OH)_2D_3$ via two catabolic routes, commencing with C24- or C23-hydroxylation and culminating in calcitroic acid or 1α,25-$(OH)_2D_3$-26,23-lactone. The degree to which 1α,25-$(OH)_2D_3$ is catabolized via the C24 or C23 hydroxylation pathway is species dependent, and we focused our studies on human (V79-CYP24 cells) and opossum (OK cells) CYP24A1, which were found to catabolize 1α,25-$(OH)_2D_3$ via primarily C24 or C23 pathway extremes. We set out to identify the molecular determinants of the unique C24 and C23-hydroxylase activity of hCYP24A1. Our sequence alignment analysis revealed that human and opossum CYP24A1 differ at only 80 amino acids, three of which in the human enzyme were prioritized for mutagenesis to the opossum form, which were selected on the basis of potential substrate contact in a homology model of human CYP24A1. The modification A326G, converted the human enzyme from a C24-hydroxylase, into a C23-hydroxylase, which closely resembled the pattern of metabolism observed in OK cells, using both 1α,25-$(OH)_2D_3$ and 25-OH-D_3 as substrates. Transient or stably transfected V79-4 cells were used to study the catabolism from 1α,25-$(OH)_2D_3$ through to calcitroic acid or 1α,25-$(OH)_2D_3$-26,23-lactone using a substrate-concentration dependent approach, where most of the intermediates from each pathway were identified on the basis of a number of criteria, including characteristic ions on LC-MS. In our homology model of CYP24A1, Ala326 is situated in the I-helix and abuts the side chain of 1α,25-$(OH)_2D_3$, and could control the depth of penetration of the side chain into the substrate-binding pocket. Substitution with Gly, as it is in opossum, allows 1α,25-$(OH)_2D_3$ to enter more deeply into the binding pocket to position C23, as opposed to C24, into an optimal orientation above the heme for hydroxylation, thus committing the catabolism of 1α,25-$(OH)_2D_3$ via 1α,23*S*,25-$(OH)_2D_3$ en route to 1α,25-$(OH)_2D_3$-26,23-lactone. We conclude that Ala326 is a major determinant of the regioselectivity difference observed between human and opossum CYP24A1.

Figure 3.6: LC-MS-based characterization of the products of 1α,25-$(OH)_2D_3$ in CYP24A1-containing cells. Molecular weight determination by LC-MS was one of the criteria used to help identify the products of the C23 or C24 hydroxylation pathways, catalyzed by CYP24A1. The major characteristic ions, including molecular ions $[M+H]^+$, sodium adducts $[M+Na]^+$ and dehydration products $[M+H-H_2O]^+$, $[M+H-2H_2O]^+$ are labelled in each mass spectrum. Note that the metabolite 23-oxo-1α,25-$(OH)_2D_3$ (peak 7a) is not shown in the C23 pathway scheme. Similar products were identified when 25-OH-D_3 was used as a substrate (not shown), where the corresponding product is denoted with 'a' in the pathway schema. All of the criteria used to help identify the metabolites are summarized in Table 3.3.

Figure 3.7: LC-MS, LC-MS/MS and sodium periodate cleavage analysis of the putative metabolites 1α,24*R*,25-$(OH)_3D_3$, and 1α,23*S*,25-$(OH)_3D_3$. A more rigorous approach was needed to help characterize 1α,24*R*,25-$(OH)_3D_3$, and 1α,23*S*,25-$(OH)_3D_3$, since they possess the same molecular weight. The techniques included an MS1 scan (A, B), a fragment ion scan (C, D) using the primary dehydration product $[M+H-H_2O]^+$ m/z 415 as the parent ion, and an MS1 scan after treatment with sodium m-periodate (E-H), where panels E and F are the untreated controls. The chromatographic shifts induced by periodate treatment are listed in Table 3.3. The sodium m-periodate study was conducted by Ms. Valarie Byford.

CHAPTER 4: MUTAGENESIS AND ACTIVITY STUDIES OF THE SUBSTRATE-BINDING POCKET OF CYP24A1

4.1 INTRODUCTION

Prior to the beginning of the work presented in this thesis, our knowledge of the structure of the substrate binding pocket of CYP24A1 was based upon inferences made from over 20 years of comparing the role of CYP24A1 in the catabolism of 1α,25-$(OH)_2D_3$ with a wide range of analogs of 1α,25-$(OH)_2D_3$ [119]. Results from the analog work focused on structural modifications to 1α,25-$(OH)_2D_3$ that altered the substrate specificity and overall activity of CYP24A1, site of hydroxylation in the side-chain, and catabolism via pathways of sequential intermediates. One such study involved a comparison of CYP27A1 and CYP24A1 activities using a series of 1α-hydroxylated and 1α,25-dihydroxylated analogs containing systematic additions of up to three carbons in the side chain [187]. The study concluded that the distance between the site of hydroxylation (C25, C27(minor)) and the end of the side-chain was an important determinant of the site of hydroxylation by CYP27A1, whereas the distance between the vitamin D nucleus and the hydroxylation site (C24, C23(minor)) is an important factor in hydroxylation site selection by CYP24A1 [187]. However, the specifics of the amino acid composition and substrate–contact points responsible for positioning the substrate within the active site continued to remain elusive due to the lack of a three-dimensional structure for CYP24A1. In 2000, Williams *et al*. reported the first crystal structure of a mammalian microsomal P450, rabbit CYP2C5 [188,189]. The determination of the crystal structures of 5 human enzymes quickly followed, including CYP2C8 [190], CYP2C9 [191], CYP3A4 [192,193], CYP2A6 [194], and CYP2D6 [195]. More recently, the crystal structure for a vitamin D_3 25-hydroxylase, CYP2R1 became available, and remains the only crystal structure of a vitamin D hydroxylase determined to date [196]. It became apparent that the wealth of rapidly-emerging crystallographic data could be used to generate a homology model to study the structure of CYP24A1.

In 2007, four homology model-based structures of CYP24A1 were published, including one from our laboratory focusing on the human enzyme [112,153,197,198] (Figure 4.1A). The model was based upon 13 prokaryotic and microsomal crystallographic templates including CYP119, CYP2B4, CYP51, CYP2C5, P450bm3, P450cam, P450eryF, P450terp, CYP2C8, CYP2C9, CYP3A4, CYP2A6 and CYP2D6. The structure possessed a typical cytochrome P450 fold, containing 14 α-helicies labeled A-L, A′ and B′, in addition to 5 β-sheets labeled 1-5, and various loops which surrounds a primarily hydrophobic

Figure 4.1: 1α,25-$(OH)_2D_3$-docked homology model of human CYP24A1: The overall topology of a homology model of hCYP24A1 is viewed looking down into the pw2a substrate access channel, containing 1α,25-$(OH)_2D_3$ situated above the heme, shown in yellow (A). A magnified view of the central core of the protein looking down the length of the I-helix, highlights the major secondary structures forming the putative substrate-binding site, including the B′-, F-, G-, I-helicies, the B/B′- and B′/C-loops, and the β-3a and β-5 sheets. Note that the B′-helix (which connects the B/B′- and B′/C-loops) has been removed to facilitate an unobstructed view of 1α,25-$(OH)_2D_3$. The residues prioritized for mutagenesis studies are also shown in green in panel B, in addition to alternative close-up views in panels C-H which feature selected amino acid substitutions presented in yellow. The hCYP24A1 homology model was created by Dr. David Prosser. This figure was generated using PyMOL files courtesy of Dr. Prosser.

substrate-binding site formed by residues of the B′-, F-, G-, I-helicies, the B/B′- ,B′/C- and F/G loops, and the β-3a and β-5a sheets [153] (Figure 1A,B). The substrate-binding cavity is situated above the heme group, positioned by conserved heme-binding residues. Carbon 24, or C23 of a 1α,25-$(OH)_2D_3$ molecule was docked in the in the substrate-binding site of the model using an approach based upon the average position of the hydroxylation-susceptible carbon in CYP crystal structures (described in Chapter 3.1), giving a distance of 3.55 Å between the C24*R*-hydrogen of 1α,25-$(OH)_2D_3$ and the heme iron [186]. The substrate-bound model of CYP24A1 formed the basis for prioritizing highly conserved and/or substrate-contact residues in the putative substrate binding pocket for site-directed mutagenesis in order to study the effects of the mutations on the catabolism of 1α,25-$(OH)_2D_3$ in stably transfected cells containing the mutant CYP24A1 proteins. The CYP24A1 mutations selected for the current study included L148A/F (B′/C-loop), I131A/F (B/B′-loop) M246L (F-helix), M252L/T(F-helix), M2523T (F-helix; denotes a M252T/M253T double mutant), S390G (β-3a sheet), V391L(β-3a sheet), M416T(β-3b sheet), G499V (β-5 sheet), and L501I/V (β-5 sheet) (Figure 1B-H). We also generated cell lines containing L148A/F, I131A/F, M252L/T, M2523T, V391L and M416T as double mutants with A326G. It was expected that insights into the role of the selected residue in the multi-step catabolism of 1α,25-$(OH)_2D_3$ could be discerned by comparing metabolic activities of the mutants with the wild-type human enzyme, as well as the A326G double mutants as compared with A326G alone where appropriate.

4.2 RESULTS

4.2.1 CATABOLISM OF 1α,25-$(OH)_2D_3$ BY Leu148-MODIFIED CYP24A1

Background. Leucine 148 is situated in the B′/C-loop, which forms the junction between the B′- and C-helicies situated above and below the plane of the heme (Figure 4.1 B,C,D). The B′/C-loop positions Leu148 above the heme propionates in a line that is essentially perpendicular to the I-helix and forms part of the side of the substrate binding cavity over the heme, and potentially contacts the side of the side chain of 1α,25-$(OH)_2D_3$. The position of the B′/C-loop is stabilized in-part by the conserved heme-binding residues Arg159 in the C-helix and Arg128 in B/B′-loop. Leu148 is conserved in 29/33 CYP24A1 proteins considered, and is conserved only within some CYP families suggesting a possible role for this residue in CYP-specific regioselectivity [153]. Hydrophobic-to-hydrophobic amino acid substitutions and activity

studies conducted at the analogous positions in P450bm3, CYP2D6, CYP2C9 and CYP2A6, resulted in a range of drastically altered enzymatic properties including novel ω-hydroxylation of laurate and myristate (F87V; P450bm3 [199]), conferring hydroxylation activity towards phenolic compounds (F87V; P450bm3[200]), loss of enantioselectivity (F120A, CYP2D6 [201]; F114L, CYP2C9 [202]) and changes in regioselectivity (F120A) in CYP2D6 [203], and reduced activity in CYP2A6 (V117A) [204]. Among the vitamin D-related CYPs, F147A/L substitutions in CYP27A1 were recently observed to enable novel 25-hydroxylation of the prodrugs 1α-OH-D_2 and DHT_2, containing vitamin D_2-type side chains (Figure 2.5)[205]. The homology modeling and mutagenesis work revealed that a steric clash between Phe147 and the C24-methyl (present in vitamin D_2-, but not vitamin D_3-type sidechains) was a likely cause of the characteristic inability of this enzyme to catalyze the 25-hydroxylation of 1α-OH-D_2, which was enabled by the F147A/L mutations which eliminated the apparent steric clash [205].

Results. We generated L148A and L148F mutants to slightly alter side chain contact with 1α,25-$(OH)_2D_3$, while maintaining the hydrophobic nature of the binding pocket. When 0.3 μM 1α,25-$(OH)_2D_3$ was incubated in cells stably expressing the Leu148 mutants, some notable differences from the wild type were observed (Figure 4.2A, 4.3A). Increased amounts of proximal pathway intermediates (peaks 2 and 4) were observed for L148A, as well as a decreased amount tetranor-1α,23-$(OH)_2D_3$, indicating a possible decrease in catabolism via the C24 pathway. Accordingly, a 2.6-fold increase in 1α,25-$(OH)_2D_3$-26,23-lactone as well as the presence of its precursors, indicated an increase in C23-pathway usage at the expense of C24 (Table A4.1). L148F exhibited no detectable lactone production, and otherwise differed from wild type by the appearance of some 1α,24,25-$(OH)_3D_3$ (Figure 4.2A), indicating a reduction in the extent of C23-pathway usage as compared with wild type. The amounts of the individual intermediates observed as determined by either ^{3}H-chromatography or UV_{265} measurements, and the corresponding C24/C23 ratios are summarized in Table A4.1. As the substrate concentration was increased (Figure 4.2 and 4.3 C,E,G), the distribution of products shifted from primarily terminal, to proximal pathway products as shown in Figure A4.1 A,C,E, (and Table A4.1) while continuing to retain the pathway selection trend initially observed at 0.3 μM. At 9 μM (Figure 4.3 G), L148A gave the greatest amount of 1α,23,25-$(OH)_3D_3$, followed by wild type and L148F (not detected). Conversely, L148A gave the least amount of 1α,24,25-$(OH)_3D_3$, followed by wild type and L148F, with similar amounts of substrate consumption between all

three enzymes (Table A4.1). The C24/C23 weighted activity ratios for wild type and L148A were of 8.9 and 3.6 respectively, where only C24 products were observed for L148F. The percentage of products in each pathway are presented for the Leu148 mutants in Figure A4.1. Overall, the mutations to Leu148 had only a modest impact on total enzyme activity, when considering the 9 μM UV_{265} measurements (Table A4.1).

In order to determine which modification (A326G or L148A/F) to the putative substrate binding site had the greatest impact on regioselectivity, L148A and L148F double mutants with A326G were created. The catabolic activity of L148A/A326G resembled the regioselectivity of A326G, giving ratios of 0-1.18, with an apparent 1.6-fold greater total enzyme activity compared to A326G alone (Table A4.1). The HPLC chromatograms in Figure 4.2 B,D,F,H representing L148A/A326G activity feature terminal C23 pathway products at 0.3 μM, maximal production of more proximal products from 1.5-3.5 μM, where peak 1α,23,25-$(OH)_3D_3$ was observed to be the major component by 9 μM. The overlay plots emphasize the common C23 pathway products among the modified CYP24A1 proteins that exhibited increased C23 pathway usage (L148A, L148A/A326G, A326G), which were observed in lower abundance or absent altogether in the wild-type chromatograms. The L148F/A326G-modified CYP24A1 exhibited no major change in regioselectivity compared to L148F alone, giving a primarily C24-pathway pattern of metabolism (Figure 4.3 B,D,F,H; Table A4.1). The introduction of A326G into L148F appeared to cause a dramatic loss of activity resulting in only 10% of total L148A activity (7% of wild type total activity), which was evident even at non-saturating 0.3 μM, where proximal pathway products were prominent, in contrast to the wild type, which had efficiently catabolized 1α,25-$(OH)_2D_3$ through to peak 5 (Figure 4.3 B). The distribution of metabolites over the substrate concentration range, as well as the percentage of total products in either the C24 or C23 pathways are plotted in Figure A4.1.

We conclude that Leu148 is also an important determinant of the regioselectivity of CYP24A1. Substitution with Ala or Phe shifted the regioselectivity towards C23- or C24-hydroxylation respectively. Given that Leu148 contacts the side of the 1α,25-$(OH)_2D_3$ side chain, the mutants likely cause a lateral shift in the position of 1α,25-$(OH)_2D_3$ towards the N-terminus of the I-helix for L148A, and towards the C-terminus of the I-helix for L148F; as compared with the longitudinal shift of 1α,25-$(OH)_2D_3$ towards the

Figure 4.2: HPLC analysis of the metabolism of 1α,25-$(OH)_2D_3$ by L148A-modified CYP24A1. Stably transfected V79-4 cells containing L148A (A,C,E,G) or L148A/A326G (B,D,F,H) were incubated with 0.3, 1.5, 3.5 and 9 μM 1α,25-$(OH)_2D_3$. The chromatograms generated from the corresponding wild-type controls are shown on each panel, in addition to A326G in panels B,D,F and H to facilitate comparisons among the different CYP24A1 proteins under investigation. Triplicate ^{3}H-chromatograms are shown for each condition, however the aqueous phase chromatography is not shown. A quantitative analysis of the chromatography shown in this figure is presented in Table A4.1.

Peak identities:

1: 1α,25-$(OH)_2D_3$
2: 1α,24,25-$(OH)_3D_3$,
3: 24-oxo-1α,25-$(OH)_2D_3$,
4: 24-oxo-1α,23,25-$(OH)_3D_3$
5: tetranor-1α,23-$(OH)_2D_3$
7: 1α,23,25-$(OH)_3D_3$
7a: 23-oxo-1α,25-$(OH)_2D_3$
9: 1α,25-$(OH)_2D_3$-26,23-lactol
10: 1α,25-$(OH)_2D_3$-26,23-lactone.

Figure 4.3: HPLC analysis of the metabolism of 1α,25-$(OH)_2D_3$ by L148F-modified CYP24A1. Stably transfected V79-4 cells containing L148F (A,C,E,G) or L148F/A326G (B,D,F,H) were incubated with 0.3, 1.5, 3.5 and 9 μM 1α,25-$(OH)_2D_3$. The chromatograms generated from the corresponding wild-type controls are shown on each panel, in addition to A326G in panels B,D,F,H and L148A on panels A,C,E,G to facilitate comparisons among the different CYP24A1 proteins under investigation. Triplicate ^3H-chromatograms are shown for each condition, however the aqueous phase chromatography is not shown. A quantitative analysis of the chromatography shown in this figure is presented in Table A4.1. Overall, our results suggested that Leu148 is an important side-chain contact residue, given that L148A shifted regioselectivity towards C23-hydroxylation (Figure 4.2, Table A4.1), and L148F shifted regioselectivity towards C24-hydroxylation.

Peak identities:

1: 1α,25-$(OH)_2D_3$
2: 1α,24,25-$(OH)_3D_3$,
3: 24-oxo-1α,25-$(OH)_2D_3$,
4: 24-oxo-1α,23,25-$(OH)_3D_3$
5: tetranor-1α,23-$(OH)_2D_3$
7: 1α,23,25-$(OH)_3D_3$
7a: 23-oxo-1α,25-$(OH)_2D_3$
9: 1α,25-$(OH)_2D_3$-26,23-lactol
10: 1α,25-$(OH)_2D_3$-26,23-lactone.

I-helix resulting from the mutation A326G. A lateral shift alone is not consistent with a change in regioselectivity *per se*, that would result from optimal positioning of C23 or C24 for hydroxylation. Rather, we propose that the role of Leu148 in regioselectivity is to form a baffle for the side of the 1α,25-$(OH)_2D_3$ side chain which laterally determines the point at which the end of the side can abut the I-helix as it enters completely into the substrate binding pocket. Substitution with Ala could permit the side chain to abut the I-helix slightly N-terminal to Ala326, where there are no intervening amino acid side chains, allowing deeper penetration into the groove of the I-helix which is consistent with the observed increase in the degree of C23-hydroxylation. The rate and degree of C23-hydroxylation was improved further with L148A/A326G by removing the amino acid side chain at Ala326. Alternatively, substitution with Phe, could permit the side chain to abut the I-helix backbone C-terminal to Ala326, preventing sufficient penetration into the binding pocket for C23-hydroxylation, rendering the position of 1α,25-$(OH)_2D_3$ in the L148F-mutated CYP24A1 independent of the residue at position 326. This proposal is consistent with our observation that the regioselectivity of L148F (a C24-hydroxylase) could not be shifted towards C23-hydroxylation by introducing an additional mutation, A326G.

4.2.2 CATABOLISM OF 1α,25-$(OH)_2D_3$ BY Ile131-MODIFIED CYP24A1

Background. The B/B′-loop connecting the B'- and B′-helicies is located adjacent to the B′/C-loop. These two loop structures are connected by the B′-helix above the heme [153]. The residue Ile131, located at the top of the B/B′-loop immediately preceding the B′-helix, is absolutely conserved across CYP24A1 species and could contact the A-ring/cis-triene of a 1α,25-$(OH)_2D_3$ molecule docked in the homology model [153] (Figure1B,C,D). Studies conducted at this position in other enzymes revealed substrate contact between Ile101 and CPI in CYP2B4 [206], substrate contact at Ile101 in CYP2B1 proposed to help mediate substrate entry/product egress [206], and altered regioselectivity was observed to result from an I112P mutation in CYP11B2 (corresponds to Glu130 in CYP24A1)[207]. Mutation of the corresponding residue in CYP27A1 (M97C) resulted in reduced substrate-binding and reduced total enzyme activity.

Results. The B/B′-loop mutants I131A and I131F, exhibited an apparent reduction in catabolism of 1α,25-$(OH)_2D_3$ via the C24-hydroxylation pathway at 0.3 μM (Figures 4.4A and 4.5A).

Most of the products observed from I131A/F comprised proximal pathway intermediates as opposed to terminal pathway metabolites produced by the wild type. The altered distribution of products was also manifested in the weighted activity measurements giving 0.54 (I131A) and 0.57 (I131F) of wild-type activity (Table A4.2). As the distribution of products produced by the wild type approached that of the mutants over the substrate concentration range, some regioselectivity differences among the CYP24A1 proteins became apparent. The I131A mutant gave a C24/C23 activity ratio of 2.6, as compared with 8.9 for the wild-type, indicating an increase in C23-hydroxylation. A more subtle regioselectivity shift was observed for I131F, giving a ratio of 5.4. As assessed at 9 μM (UV_{265}), the mutations I131A and I131F did not appear to have a major impact on total enzyme activity, suggesting that reduced progression through the intermediates of the C24-hydroxylation pathway, was not entirely due to differences in enzyme activity (Table A4.2), and most likely due to reduced catabolism of 1α,24,25-$(OH)_3D_3$ which accumulated at both saturating and non saturating substrate concentrations (Figure A4.2). When I131A/A326G and I131F/A326G double mutants were studied (Figure 4.4 and 4.5 B D F H), we observed a significant regioselectivity shift towards C23-hydroxylation similar to A326G, giving ratios of 0.06 and 0.05 at 9 μM respectively. The percentage of total product present in the C24 or C23 pathway were also similar to A326G (Figure A4.2). Despite an increase in total activity relative to A326G, the metabolite 1α,23,25-$(OH)_3D_3$ appeared to be poorly catabolized to downstream products, as indicated by the dominance of 1α,23,25-$(OH)_3D_3$ as the major product at all substrate concentrations considered (Figure A4.2).

In summary, our modifications to Ile131 in the B/B′-loop suggest that this residue is also involved in determining regioselectivity. Somewhat surprising was that our modification (I131A) of substrate contact at the distant A-ring of 1α,25-$(OH)_2D_3$ enabled a similar shift in regioselectivity, as did L148A, which is in direct proximity to the hydroxylation susceptible carbons in the side chain of 1α,25-$(OH)_2D_3$. It can be interpreted that B/B′-loop also acts as a baffle for the A-ring, or perhaps directs the side chain into a position that (with I131A) enhances the degree of C23-hydroxylation as it enters the substrate binding pocket. The modeled change in substrate contact at the A-ring, is consistent with a possible lateral shift in the 1α,25-$(OH)_2D_3$ molecule in the direction of the N-terminus of the I-helix, similar to the predicted effect of the modification L148A. A downward orientation of Phe substituted at position 131, might explain why

Figure 4.4: HPLC analysis of the metabolism of 1α,25-$(OH)_2D_3$ by I131A-modified CYP24A1. Stably transfected V79-4 cells containing I131A (A,C,E,G) or I131A/A326G (B,D,F,H) were incubated with 0.3, 1.5, 3.5 and 9 μM 1α,25-$(OH)_2D_3$. The chromatograms generated from the corresponding wild-type controls are shown on each panel, in addition to A326G in panels B,D,F and H to facilitate comparisons among the different CYP24A1 proteins under investigation. Triplicate ^{3}H-chromatograms are shown for each condition, however the aqueous phase chromatography is not shown. A quantitative analysis of the chromatography shown in this figure is presented in Table A4.2.

Peak identities:

1: 1α,25-$(OH)_2D_3$
2: 1α,24,25-$(OH)_3D_3$,
3: 24-oxo-1α,25-$(OH)_2D_3$,
4: 24-oxo-1α,23,25-$(OH)_3D_3$
5: tetranor-1α,23-$(OH)_2D_3$
7: 1α,23,25-$(OH)_3D_3$
7a: 23-oxo-1α,25-$(OH)_2D_3$
9: 1α,25-$(OH)_2D_3$-26,23-lactol
10: 1α,25-$(OH)_2D_3$-26,23-lactone.

Figure 4.5: HPLC analysis of the metabolism of 1α,25-$(OH)_2D_3$ by I131F-modified CYP24A1: Stably transfected V79-4 cells containing I131F (A,C,E,G) or I131F/A326G (B,D,F,H) were incubated with 0.3, 1.5, 3.5 and 9 μM 1α,25-$(OH)_2D_3$. The chromatograms generated from the corresponding wild-type controls are shown on each panel, in addition to A326G in panels B,D,F,H and I131A on panels A,C,E,G to facilitate comparisons among the different CYP24A1 proteins under investigation. Triplicate ^3H-chromatograms are shown for each condition, however the aqueous phase chromatography is not shown. A quantitative analysis of the chromatography shown in this figure is presented in Table A4.2. Even though I131A (Figure 4.4) and I131F resulted in altered regioselectivity, the main feature of these mutants was their ability to reduce progression through the C24-hydroxylation pathway primarily due to reduced catabolism of 1α,24,25-$(OH)_3D_3$. An analogous lack of catabolism of 1α,23,25-$(OH)_3D_3$ was observed in the C23-hydroxylation when the double mutants I131A/A326G (Figure 4.4) and I131F/A326G were considered.

Peak identities:

1: 1α,25-$(OH)_2D_3$
2: 1α,24,25-$(OH)_3D_3$,
3: 24-oxo-1α,25-$(OH)_2D_3$,
4: 24-oxo-1α,23,25-$(OH)_3D_3$
5: tetranor-1α,23-$(OH)_2D_3$
7: 1α,23,25-$(OH)_3D_3$
7a: 23-oxo-1α,25-$(OH)_2D_3$
9: 1α,25-$(OH)_2D_3$-26,23-lactol
10: 1α,25-$(OH)_2D_3$-26,23-lactone.

I131F illicited a modest shift towards C23-hydroxylation, rather than an extended orientation of Phe, positioned perpendicular to the B/B′-loop backbone causing a lateral shift of 1α,25-$(OH)_2D_3$ in the direction of the C-terminus of the I-helix. In additional to changes in regioselectivity, I131A/F reduced the extent of progression through the C24-hydroxylation pathway, that appeared to result from a reduction in catabolism of peak 2. We propose that I131A/F mutations either caused a suboptimal re-orientation of 1α,24,25-$(OH)_3D_3$ in the binding site in preparation for catabolism to 24-oxo-1α,25-$(OH)_2D_3$, or altered the re-access of 1α,24,25-$(OH)_3D_3$, since Ile131 is situated at the junction point of several purported substrate access channels, including pw2a, pw2b and pw2c [153]. Interestingly, the double mutants I131A/A326G and I131F/A326G completely adopted the regioselectivity characteristics of A326G, but retained the pathway progression properties of I131A/F alone, where there was an apparent reduction in degradation of 1α,23,25-$(OH)_3D_3$, through to downstream products in the C23-hydroxylation pathway, despite an increased total enzyme activity.

4.2.3 CATABOLISM OF 1α,25-$(OH)_2D_3$ BY M246L-MODIFIED CYP24A1

Background. The F-helix spans the top of the substrate-binding pocket, perpendicular to the centre of the I-helix (Figure 4.1B,H). Omdahl's group has studied several modifications to the F-helix, in the proximity of the A-ring and the cis-triene system of 1α,25-$(OH)_2D_3$ docked in a model of rCYP24A1 [207]. Met246 and Phe249 were observed to extend into the substrate binding site. The mutations F249T/A/Y resulted in decreased binding affinity to the protein, in addition to a reduced rate of catabolism of tetranor-1α,23-$(OH)_2D_3$ to calcitroic acid, where F249Y also exhibited a reduction in catabolism of 1α,24,25-$(OH)_3D_3$. Mutations to Phe 249 were believed to alter hydrophobic interactions with the cis-triene, necessary for optimal positioning of C24 for hydroxylation. M246F exhibited a reduction in substrate binding, however effects on 1α,25-$(OH)_2D_3$ catabolism were not determined due to poor expression levels. Other mutations including M245A, S247V and T248A located on the opposite side of the F-helix, reduced the rate of catabolism of tetranor-1α,23-$(OH)_2D_3$ to calcitroic acid without affecting substrate binding [197,207]. The group proposed that these residues could mediate interactions with the A′, B′, and G-helicies which might help form substrate access/product egress channels [197]. In CYP27A1, a

regioselectivity effect was observed to result from F248K, which selectively reduced the amount of C25-hydroxylation without altering C27-hydroxylation [154].

Results. In our model of hCYP24A1, Met246 points down from the F-helix towards the I-helix and is not likely a 1α,25-$(OH)_2D_3$-contact residue. The mutation M246L had a similar effect on the catabolism of 1α,25-$(OH)_2D_3$ as observed for I131A/F, where there was an apparent reduction in the catabolism of 1α,24,25-$(OH)_3D_3$ to downstream products without having a major impact on total enzyme activity as determined at 9 μM (Figure 4.6; Table A 4.3). This observation was consistent with the effects of mutations to Phe249 studied by Omdahl's group. Interestingly, M246L also had a major effect on regioselectivity, giving a C24/C23 activity ratio of 0.9 (as compared with 13 for wild type). Because of the significant degree of C23-hydroxylation, a block in the C23-hydroxylation pathway was identified to result in the reduced catabolism of peak 23-oxo-1α,25-$(OH)_2D_3$ as determined from the observed accumulation of this product (Figure 4.6; Table A 4.3, Figure A4.3).

Taken together, the effects of the modification M246L on 1α,25-$(OH)_2D_3$ catabolism seemed to suggest that this residue could be involved in helping to position 1α,25-$(OH)_2D_3$ for hydroxylation, given that this mutation had the second largest effect on regioselectivity among the single mutants (after A326G). After initial hydroxylation, we propose that M246L altered the ability of the intermediates 1α,24,25-$(OH)_3D_3$ and 23-oxo-1α,25-$(OH)_2D_3$ to optimally re-orient or access the active site for the subsequent catabolic step, resulting in their accumulation. These results were surprising, given that Met246 likely has no direct contact with the docked 1α,25-$(OH)_2D_3$ molecule, as compared with L148A/F and I131A/F which had less impact on regioselectivity than M246L despite direct contact with 1α,25-$(OH)_2D_3$. We speculate that Met246 acts indirectly via substrate contact residues in the F-helix including Phe249, which exhibited a minor deflection upon substrate docking. Mutations to Phe249 in rCYP24A1 resulted in reduced subsequent catabolism of the intermediates tetranor-1α,25-$(OH)_2D_3$ and 1α,24,25-$(OH)_3D_3$, similar to our observed points of pathway arrest at 1α,24,25-$(OH)_3D_3$ and 23-oxo-1α,25-$(OH)_2D_3$. The modifications M245A, S247V and T248A exhibited similar pathway arrest features as mutations to Phe249 and our M246L mutant, even though the side chains were extended away from the substrate binding cavity in the homology model of rCP24A1. The authors of the work proposed that Met245, Ser247 and Thr248 could help mediate substrate access/product egress channels. Due to the position of Met246 above the

Figure 4.6: HPLC analysis of the metabolism of 1α,25-$(OH)_2D_3$ by M246L-modified CYP24A1: Stably transfected V79-4 cells containing M246L (A,C,E,G) were incubated with 0.3, 1.5, 3.5 and 9 μM 1α,25-$(OH)_2D_3$. The chromatograms generated from the corresponding wild type control are shown on each panel, in addition to A326G in panels B,D,F and H to facilitate comparisons among the different CYP24A1 proteins under investigation. Triplicate ^{3}H-chromatograms are shown for each condition, however the aqueous phase chromatography is not shown. The accumulation of peaks 1α,24,25-$(OH)_3D_3$ and 23-oxo-1α,25-$(OH)_2D_3$ at all substrate concentrations considered, suggested that M246L blocked progression through the C24- and C23-hydroxylation pathways at these metabolites. The quantitative analysis of the chromatography shown in this figure (Table A4.3) suggested that the reduction in pathway progression was not due to major differences in total enzyme activity.

Peak identities:

1: 1α,25-$(OH)_2D_3$
2: 1α,24,25-$(OH)_3D_3$,
3: 24-oxo-1α,25-$(OH)_2D_3$,
4: 24-oxo-1α,23,25-$(OH)_3D_3$
5: tetranor-1α,23-$(OH)_2D_3$
7: 1α,23,25-$(OH)_3D_3$
7a: 23-oxo-1α,25-$(OH)_2D_3$
9: 1α,25-$(OH)_2D_3$-26,23-lactol
10: 1α,25-$(OH)_2D_3$-26,23-lactone.

centre of the I-helix, another possible explanation for the effects for M246L, is the disruption of the proton transfer function of Glu329 [153]. This possibility is less likely since there is no major loss of total enzyme activity exhibited by M246L.

4.2.4 CATABOLISM OF 1α,25-$(OH)_2D_3$ BY M252- and M253-MODIFIED CYP24A1

Background. The F/G-loop region (Figure 4.1A,H) exhibited the greatest route mean squared deviation (RMSD) in our homology model of hCYP24A1, attesting to the fact that these structures are highly variable between P450 families, and are likely determinants of substrate specificity [153] (Figure 4.1A,H). The F/G-loop forms the beginning of the pw2a substrate access channel, defined as a route of access or egress lined by the B′/C-loop, the B/B′-loop/B-helix and the F/G-loop [162]. Recent studies have highlighted the importance of the F/G-loop in substrate recognition and specificity. For example CYP3A7 and CYP3A4, possess 88% amino acid sequence identity but exhibit differences in substrate specificity. Substitution of selected F/G-loop residues of CYP3A7 with corresponding CYP3A4 residues, resulted in the mutated CYP3A7 adopting some of the catalytic properties of CYP3A4, including a loss of 16α-hydroxylation activity towards dehydroepiandrosterone, compared with high levels of activity observed with wild type CYP3A7 [208]. In a similar study focusing on CYP2C9, F/G-loop residues were substituted to those observed in CYP2C19, possessing 91% sequence identity with CYP2C9. The CYP2C9 mutants exhibited characteristic CYP3A7 activities including 4-hydroxylase activity towards diclofenac, and *p*-methylhydroxylase activity towards tolbutamide [209]. The residue Thr192 in the F/G-loop of P450cam has been implicated in recognition of camphor at the beginning of the substrate access channel on the surface of the enzyme [210]. Additional crystallographic work has revealed that the F/G-loop can undergo significant conformational change upon substrate or inhibitor binding, specifically the F/G-loops of; CYP3A4 upon ketoconazole or erythromycin binding [211], CYP2B4 upon 1-biphenyl-4-methyl-1*H*-imidazole binding [212], and CYP106A2 upon 11-deoxycortisol and progesterone binding (and mutational analysis), which the authors describe as a transition between an open and a closed active site conformation [213]. Residue Leu208 situated just before the F/G-loop has been identified as an important determinant of the orientation of phenytoin within the active site of CYP2C9 [214].

Results. We focussed on studying mutations at highly conserved residues at the end of the F-helix at the beginning of the F/G-loop, namely M252L, M252T, M2523T, in addition to double (or triple) mutants with A326G (Figure 4.1E). We selected the C-terminus of the F-helix for our mutagenesis studies since these residues were in proximity to the A-ring of the docked 1α,25-$(OH)_2D_3$ molecule, where we altered or disrupted hydrophobic contact by making mutations from Met to Leu or Thr. Overall, the M252L mutant exhibited a 2.4-fold increase in total enzyme activity and a change in regioselectivity towards C24-hydroxylation giving a C24/C23 activity ratio of 52 as compared with 13 for the wild type at 9 μM, which indicated only a minor shift in regioselectivity towards C24-hydroxylation (Figure 4.7; Table A4.4, Figure A4.4). The M252L/A326G double mutant catabolized 1α,25-$(OH)_2D_3$ via mainly C23-hydroxylation pathway products similar to A326G alone, giving a C24/C23 ratio of 0.07, as compared with 0.04 for A326G. The M252L mutation also had the same activity-enhancing effect on A326G as it did for the wild type, exhibiting 4-fold greater activity than A326G alone. Given the growing consensus that the F/G-loop is a mediator of substrate recognition and specificity, it is conceivable that altered hydrophobic contact between residue 252 and the A-ring of 1α,25-$(OH)_2D_3$ enabled enhanced access or transit of 1α,25-$(OH)_2D_3$ and its intermediates through the pw2a substrate access channel.

The M252T mutation (Figure 4.8) exhibited a drastic lack of flux through the C24-hydroxylation pathway, as indicated by the accumulation of proximal pathway intermediates, and the virtually identical distribution of the products at all substrate concentrations considered (Table A4.4, Figure A4.4). The M252T mutant had little effect on total enzyme activity at 9 μM, suggesting that the altered distribution of products relative to the wild type is indeed due to a lack of flux, and not due to a reduction in total enzyme activity. Pathway arrest seemed to occur most significantly due to a lack of catabolism of 1α,24,25-$(OH)_3D_3$, based upon its abundance. To a lesser extent, a reduction in pathway progression also seemed to occur via reduced 1α,25-$(OH)_2D_3$ catabolism to 1α,24,25-$(OH)_3D_3$, and 23-oxo-1α,23,25-$(OH)_3D_3$ to tetranor-1α,23-$(OH)_2D_3$, as indicated by the complete absence of tetranor-1α,23-$(OH)_2D_3$ (peak 5) in all of the chromatograms. Interestingly, the ability of M252T to arrest catabolism within the C24-hydroxylation pathway was observed more subtly with M246L, situated at the N-terminus of the F-helix, and I131A/F, also located near the beginning of the pw2a access channel. M252T also shifted regioselectivity towards C23-hydroxylation, giving a C24/C23 ratio of 3.7 as compared with 13 for wild type. This observation was

somewhat surprising, given that Met252 is predicted to interact with the substrate A-ring, distant from the hydroxylation susceptible carbons on the substrate side chain, but consistent with observations from CYP2C9 mutagenesis studies suggesting that access channel F/G-loop residues may be involved in optimal positioning of the substrate within the active site [214]. Mutation of both Met252 and the adjacent Met253 to Thr, resulted in a total loss of enzyme activity, suggesting that these residues are together essential for the proper functioning of the F/G-loop in the CYP24A1 catabolic cascade. In additional to potential contact with the substrate A-ring, Met253 could also interact with adjacent structures, including the β5-sheet. M252T/A326G resulted in catabolism of 1α,25-$(OH)_2D_3$ via the C23-hydroxylation pathway, similar to A326G, giving a C24/C23 hydroxylation ratio of 0.06, as compared with 0.04 for A326G (Table A4.4). As was the case with M252T in the C24 pathway, M252T/A326G caused a C23-pathway block characterized by a reduced catabolism of 1α,23,25-$(OH)_3D_3$ (Figure 4.8) despite increased total activity when compared to A326G. The activity-reducing effect of M2523T was not altered by introducing the A326G mutation .

In summary, we propose that Met252 and Met253 help mediate the entry and position of 1α,25-$(OH)_2D_3$ or its catabolites in the active site via contacts with the A-ring. The substitution M252L which altered hydrophobic contact with the A-ring, appeared to enable enhanced catabolism via C24-hydroxylation or C23-hydroxylation, as observed for M252L/A326G. We cannot rule out enhanced expression of M252L (RQ=1.91) and M252L/A326G (RQ=1.89) as a possible explanation for the apparent increase in activity as compared with the wild type (Table A2.2). Substitution of Met252 with polar Thr, resulted in C24-pathway arrest, observed as a reduction of 1α,25-$(OH)_2D_3$ conversion to 1α,24,25-$(OH)_3D_3$ (minor), the subsequent catabolism of 1α,24,25-$(OH)_3D_3$ (or 1α,23,25-$(OH)_3D_3$ by M252T/A326G; major) and the side-chain cleavage step to tetranor-1α,23-$(OH)_2D_3$ (minor). A detectable effect on regioselectivity also provided evidence to suggest that residue 252 could be involved in optimally positioning 1α,25-$(OH)_2D_3$ in the substrate binding pocket. Substitution with Thr may have disrupted hydrophobic interactions, potentially enabling hydrogen bonding with the catabolite functional groups upon entry or egress, reducing catabolism to the subsequent pathway product. Metabolites containing C23- and/or C24-hydroxyl groups appeared to be the most resistant to further catabolism, noting that peak 4, also containing a C23-hydroxyl group did not proceed to tetranor-1α,23-$(OH)_2D_3$ by M252T in the C24-pathway. Based

Figure 4.7: HPLC analysis of the metabolism of 1α,25-$(OH)_2D_3$ by M252L-modified CYP24A1. Stably transfected V79-4 cells containing M252L (A,C,E,G) or M252L/A326G (B,D,F,H) were incubated with 0.3, 1.5, 3.5 and 9 μM 1α,25-$(OH)_2D_3$. The chromatograms generated from the corresponding wild-type controls are shown on each panel, in addition to A326G in panels B,D,F and H to facilitate comparisons among the different CYP24A1 proteins under investigation. Triplicate ^{3}H-chromatograms are shown for each condition, however the aqueous phase chromatography is not shown. A quantitative analysis of the chromatography shown in this figure is presented in Table A4.4. The increased total activity exhibited by M252L is evident from the distribution of products at 3.5 and 9 μM which favoured the production of more terminal pathway products than the wild type. The activity-enhancing ability of M252L was also conserved in the C23-hydroxylation pathway as observed with the double mutant M252L/A326G.

Peak identities:

1: 1α,25-$(OH)_2D_3$
2: 1α,24,25-$(OH)_3D_3$,
3: 24-oxo-1α,25-$(OH)_2D_3$,
4: 24-oxo-1α,23,25-$(OH)_3D_3$
5: tetranor-1α,23-$(OH)_2D_3$
7: 1α,23,25-$(OH)_3D_3$
7a: 23-oxo-1α,25-$(OH)_2D_3$
9: 1α,25-$(OH)_2D_3$-26,23-lactol
10: 1α,25-$(OH)_2D_3$-26,23-lactone.

Figure 4.8: HPLC analysis of the metabolism of 1α,25-$(OH)_2D_3$ by M252T- and M2523T-modified CYP24A1. Stably transfected V79-4 cells containing M252T (A,C,E,G) or M252T/A326G (B,D,F,H) were incubated with 0.3, 1.5, 3.5 and 9 μM 1α,25-$(OH)_2D_3$. The chromatograms generated from the corresponding wild-type controls are shown on each panel, in addition to A326G in panels B,D,F and H and M252L on panels A,C,E,G to facilitate comparisons among the different CYP24A1 proteins under investigation. The M2523T and M2523T/A326G (dotted) mutants shown in grey, were observed to be inactive, based upon a lack of substrate consumption or product formation (shown instead of a control). Triplicate ^{3}H-chromatograms are shown for each condition, however the aqueous phase chromatography is not shown. A quantitative analysis of the chromatography shown in this figure is presented in Table A4.4.

Peak identities:

1: 1α,25-$(OH)_2D_3$
2: 1α,24,25-$(OH)_3D_3$,
3: 24-oxo-1α,25-$(OH)_2D_3$,
4: 24-oxo-1α,23,25-$(OH)_3D_3$
5: tetranor-1α,23-$(OH)_2D_3$
7: 1α,23,25-$(OH)_3D_3$
7a: 23-oxo-1α,25-$(OH)_2D_3$
9: 1α,25-$(OH)_2D_3$-26,23-lactol
10: 1α,25-$(OH)_2D_3$-26,23-lactone.

on crystallographic evidence demonstrating movement of the F and G helicies and the adjoining F/G-loop upon substrate binding for certain CYPs, we must also consider the possibility that the polar residue mutations altered wild type movement in the F/G-loop from an open to a closed conformation upon substrate binding, particularly in the case of M2523T which could alter contact with, and prevent movement with respect to the adjacent β-5 sheet.

4.2.5 CATABOLISM OF 1α,25-$(OH)_2D_3$ BY Ser390-, Val391- and Met416-MODIFIED CYP24A1

Background. The highly conserved β-3a sheet begins after the K-helix adjacent to the Thr330 in the I-helix and forms the side of the substrate binding site below the β-5 sheet. A bend in the β-3a sheet permits several potential substrate contact residues, including Val391 (Figure 4.1G). Subsequent residues Phe393 and Thr395 form the back of the substrate binding site below the entrance to the pw2a access channel [153]. The β-3a sheet ends near the B/B′-loop, after a conserved heme-binding residue, Arg396. The β-3a sheet is flanked by β-3b, containing Met 416 which also helps form the back of the substrate binding site [153]. Thr416 (rCYP24A1) has been implicated as a determinant of the regioselectivity differences between rat and human CYP24A1. A homology model of rCYP24A1 revealed Thr416 as a potential A-ring contact residue which was mutated to the human form (T416M) resulting in an increase in C23-hydroxylation, similar to human CYP24A1, as compared to rCYP24A1 which catalyzed only C24-hydroxylation [112]. Thr416 aligned with Thr409 in CYP27B1, which has also been implicated in substrate binding in that enzyme via a hydrogen bond with the 25-hydroxyl group [215]. We performed the inverse mutation (M416T) using the human enzyme to assess whether or not this residue was also a determinant of regioselectivity in the human enzyme. At the beginning of the β-3a sheet, we focused on V391L and S390G mutants. In rat CYP24A1, a V391A mutation was observed to reduce binding affinity to the enzyme and impaired the conversion of tetranor-1α,23-$(OH)_2D_3$ to calcitroic acid [197]. Ser390 is predicted to be an important structural link forming a hydrogen bond with the above β-5 sheet, and possibly the adjacent I-helix. Ser390 is most likely not a substrate contact residue.

Results. S390G resulted in reduction in total enzyme activity to one third of wild type, as well as a change in regioselectivity towards C23-hydroxylation giving a C24/C23 of 5.9, as opposed to 28 for the wild type (Figure 4.9, Table A4.5, Figure A4.5). Given the drastically different activities at 9μM, we

concluded that the altered distribution of products observed at 0.3 μM is due to a reduction in enzyme activity and not due to a block in the catabolic pathway resulting from a lack of catabolism of a particular intermediate.

A turn in the β-3a sheet potentially places the side chain of adjacent Val 391 into contact with C21 of 1α,25-$(OH)_2D_3$ (Figure 4.1G). Our V391L mutant exhibited an increase in total enzyme activity relative to the wild type (Table A4.6). The mutant enzyme was mainly a C24-hydroxylase, possessing a C24/C23 ratio of 38, as compared with 9 for the wild type. Progression of intermediates through the C24-hydroxylation pathway, appeared not to be drastically different than the wild type (Figure A4.5 C,E). When we compared the catabolism of 1α,25-$(OH)_2D_3$ by a V391L/A326G double mutant of CYP24A1, a characteristic shift in regioselectivity towards C23-hydroxylation was observed (Figure 4.10 B,D,F,H). Interestingly, the regioselectivity did not completely shift to C23-hydroxylation, as was observed for A326G (C24/C23 ratio 0.03) and most of the other double mutants, giving hydroxylation ratios of 0.58-1.0 over the substrate concentrations tested (Table A4.6, Figure A4.5). The V391L/A326G double mutant did not appear to be drastically different from the wild type in terms of total activity. Overall, the results suggested that Val391 is an important substrate contact residue, since substitution with Leu appeared to increase the degree of C24-hydroxylation. Even though this was a relatively subtle shift when compared to L148F (see Chapter 4.2.1), the potential role of Val391 as a determinant of C24-hydroxylation was manifested by the inability of this mutant to become completely converted to a C23-hydroxylase by introducing A326G as a double mutant. Val391 is not a determinant of species-based differences in CYP24A1 activity, since the amino acid sequence of the β-3a sheet (Pro389-Leu398) is invariable among the CYP24A1 sequences considered.

The M416T mutation in the β-3b sheet, located behind the β-3a sheet, resulted in an enzyme with only slightly less activity than the wild type at 9 μM. M416T was observed to have an effect on regioselectivity, and caused a shift in the C24/C23 hydroxylation ratio from 13 (wild type) to 27, in support of the hypothesis that Met416 could be a determinant of the regioselectivity differences observed between human and rat CYP24A1, given that Hamamoto *et al.* recently showed that a T416M substitution in rCYP24A1 shifted regioselectivity towards the degree of C23-hydroxylation observed with the human enzyme [112] (Figure 4.11, Table A4.7). The similar weighted activity measurements for M416T and wild

type at 9 μM (2221 pmol/2.4×10^6 cells/24 h; 2420 for wild type), are somewhat deceiving, given that twice as much substrate remained for the mutant when compared to the wild type, indicating relatively poor enzyme activity. This difference in substrate consumption is reflected in the non-weighted activity measurements (Table A4.7), giving 896 versus 1618 pmol/2.4×10^6 cells/24 h for M416T and wild type respectively. The reason for the discrepancy between substrate consumption and the weighted activity measurements is the remarkable degree of calcitroic acid production by M416T at 9 μM (Table A4.7), as well as the significant amount of metabolism through to tetranor-1α,23-$(OH)_2D_3$ (Figure 4.16 G), even though much less substrate was consumed. We propose that M416T hindered the access of 1α,25-$(OH)_2D_3$ to the substrate-binding site of CYP24A1, but once 1α,25-$(OH)_2D_3$ gained access, it was efficiently catabolized through to terminal pathway products. The low substrate concentrations studied revealed that Met 416 was particularly efficient at catalyzing the conversion of tetranor-1α,23-$(OH)_2D_3$ to calcitroic acid, yielding 6-fold more calcitroic acid than the wild type (Table A4.7, Figure A4.3). The M416T-modified CYP24A1 was converted into a C23-hydroxylase when the A326G substitution was introduced (C24/C23 ratio 0.06). The catabolic properties of M416T were also observed for M416T/A326G in the C23-hydroxylation pathway, however the pattern of reduced substrate consumption but enhanced degradation of intermediates was less prominent due to the inherently reduced efficiency of C23-hydroxylation and reduced systemic recovery of metabolites at the end of the C23-hydroxylation pathway. Since the introduction of A326G as a M416T/A326G double mutant resulted in C23-hydroxylation, we conclude that the presence of Ala at position 326 is a more important determinant of the regioselectivity characteristics of hCYP24A1 than Met 416 (Figure 4.11, Table A4.7, Figure A4.3).

Taken together, mutagenesis of the selected β-3a and β-3b residues resulted in quite diverse effects on the catabolic activity of CYP24A1. The homology modeling analysis revealed that Ser390 might play a structural role in linking the I-helix and the β-5 sheet. Our modification S390G resulted in reduced enzyme activity and a shift in regioselectivity towards C23-hydroxylation, suggesting that Ser390 might play a role in altering the position of 1α,25-$(OH)_2D_3$ in the substrate binding pocket by indirectly altering the integrity of the β-3a sheet, which defines the side and back of the substrate binding site. The residue Val391, in contact with C21 of 1α,25-$(OH)_2D_3$, appeared to be a general determinant of the optimal positioning of 1α,25-$(OH)_2D_3$ for C24 hydroxylation. V391L might act as a 'handle' on C21 to reduce

complete entry into the substrate binding pocket for C23-hydroxytlation. Even in the presence of A326G, much of the catabolism of 1α,25-$(OH)_2D_3$ proceeded via C24-hydroxylation. M416T slightly enhanced the degree of C24-hydroxylation, in agreement with a reciprocal study done with rCYP24A1 (T416M), suggesting that Met416 might be a determinant of the species-based difference in regioselectivity between human and rat CYP24A1. We observed a remarkable ability of M416T to catabolize C24- (or C23-) hydroxylation pathway intermediates, particularly tetranor-1α,23-$(OH)_2D_3$, despite reduced substrate consumption, which we interpret to indicate that M416T reduced access of 1α,25-$(OH)_2D_3$ to the substrate binding pocket, but was able to permit optimal orientation/access to the C24- or C23- hydroxylated intermediates. We propose that Met416 is involved in substrate access as well as regioselectivity.

4.3 SUMMARY

In the absence of a crystal structure of human CYP24A1, a homology model containing a docked 1α,25-$(OH)_2D_3$ molecule was generated [153]. The model was used to predict structures that enclose a putative substrate-binding cavity, and identify residues that could be involved in positioning 1α,25-$(OH)_2D_3$ in the substrate-binding pocket, as well as residues that might play an important structural role. To test this hypothesis, we compared the catabolism of 1α,25-$(OH)_2D_3$ by wild type hCYP24A1 with modified proteins containing mutations at selected highly-conserved residues in the B′/C-loop (L148A/F), B/B′-loop (I131A/F), F-helix (M246L, M252L/T, M2523T), β-3a sheet (S390G, V391L), β-3b sheet (M416T), and β-5 sheet (G499V, L501I/V; presented in Appendix 4.2.6). We also generated several double (or triple) mutants with the I-helix mutation A326G (Chapter 3), including L148A/F, I131A/F, M252L/T, M2523T, V391L and M416T.

Most of the CYP24A1 mutants under investigation in this chapter exhibited changes in wild type CYP24A1 activity, suggesting that they might play important roles in the multi-step catabolism of 1α,25-$(OH)_2D_3$ (summarized in Table 4.1). The substrate concentration-dependent approach used to assay the stably-expressed mutant CYP24A1 proteins revealed several recurring themes regarding the effect of the mutations on wild type activity, including alterations in (1) regioselectivity, (2) catabolic flux through several intermediates en route to calcitroic acid or 1α,25-$(OH)_2D_3$-26,23-lactone, and (3) total enzyme activity. Without question, the A326G mutation (I-helix) had the greatest impact on the regioselectivity of

CYP24A1, converting wild type CYP24A1 (mainly a C24-hydroxylase) into a C23-hydroxylase by increasing the depth of penetration of the side chain into the substrate-binding site which positions C23 instead of C24 above the heme for hydroxylation. Attesting to the importance of Ala326 in regioselectivity, was the observation that most of the mutants selected for double mutation (C24-hydroxylases) with A326G were converted to C23-hydroxylases. Also in predicted proximity to the hydroxylation susceptible carbons, Leu148 (B′/C-loop) also proved to be an important determinant of regioselectivity, where L148A increased the degree of C23-hydroxylation, and L148F almost completely abolished C23-hydroxylation in favour of C24-hydroxylation. Even though total enzyme activity of L148A/A326G was severely compromised, the regioselectivity of L148F could not be altered by A326G, resulting in a C24-hydroxylase. Altering the position of the side chain above the heme resulted in major losses in enzyme activity with A326G, as well as by combining opposing C23- and C24-enabling forces by generating a L148F/A326G double mutant. We cannot rule out increased protein expression as a reason for the apparent increase in activity caused by V391L, however it appeared to be an important determinant of C24-hydroxylation, that could not be completely reversed to C23-hydroxylation by A326G. In summary, modification of the residues predicted to contact the side chain of 1α,25-$(OH)_2D_3$ had the greatest impact on regioselectivity among the mutants presented, but exhibited no major changes in progression through the intermediates of either pathway. The changes in regioselectivity exhibited by A326G, L148A/F and the related A326G double mutants are consistent with the homology modeling-based prediction that these are side chain contact residues that determine the position of the side chain in the substrate binding pocket of CYP24A1.

The mutagenesis strategy also focused on studying the effects on catabolism of mutations to potential A-ring and cis-triene contact residues that define part of a putative substrate access channel. Somewhat surprisingly, we observed that many of these mutants, distant from the substrate side chain containing the target carbons, were able to cause changes in regioselectivity. These mutants included M246L, I131A, M252T, and to a lesser extent I131F and M416T, suggesting that predicted interactions with the substrate A-ring/cis triene effect changes in the position of the substrate side chain, although most of the changes in regioselectivity were less in magnitude than those observed for A326G and L148A/F. The main characteristic of mutations to A-ring/cis-triene contact residues was altered progression through

C24 or C23 pathway intermediates. The mutants I131A/F, M246L, M252T all exhibited a reduction in catabolism of peak 2 to downstream products in the C24-hydroxylation pathway, with M252T causing a complete block in side chain cleavage to tetranor-1α,23-$(OH)_2D_3$. M416T appeared to efficiently catalyze 1α,24,25-$(OH)_3D_3$ to calcitroic acid, even though significantly less substrate was consumed, paradoxically indicating a less active enzyme. We interpret that Ile131, Met246, Met252 and Met416 are involved in access and/or optimal positioning of intermediates in the substrate binding pocket, with Met416 specifically mediating the access of 1α,25-$(OH)_2D_3$. It is also possible that Met252 is also involved in substrate access since M252L enhanced total enzyme activity, and the double mutant M2523T completely abolished enzyme activity. When combined with A326G, these mutants exhibited parallel pathway flux properties in the C23-pathway, suggesting that the side chain- and A-ring/cis-triene-contact residues have independent but complimentary roles in determining the characteristic enzymatic properties of CYP24A1. The mutant M246L is particularly interesting because it did not appear to be in contact with the A-ring, cis-triene or side chain of 1α,25-$(OH)_2D_3$ and yet had the second greatest impact on regioselectivity (after A326G) and had a major impact on pathway flux, revealing reduced catabolism of 1α,24,25-$(OH)_3D_3$. Because of the almost equal usage of each catabolic pathway, a lack of catabolism of peak 23-oxo-1α,25-$(OH)_2D_3$ was identified as a pathway flux consequence of M246L in the C23-pathway. It appears as though Met246 is involved in both regioselectivity and intermediate access or egress, but the homology modeling did not necessarily predict this role. Possible reasons for this discrepancy include the high structural and sequence variability in this region among the crystallographic templates used to model hCYP24A1, as well as recent reports suggesting that the F-G helix-loop-helix is not a static entity and may undergo significant movement upon substrate recognition and binding [211-213]. If this is the case with CYP24A1 as well, it is conceivable that Met246 might be involved in substrate contact, in agreement with our experimental results.

Figure 4.9: HPLC analysis of the metabolism of 1α,25-$(OH)_2D_3$ by S390G-modified CYP24A1: Stably transfected V79-4 cells containing either wild type (A,C,E,G) or S390G (B,D,F,H) were incubated with 0.3, 1.5, 3.5 and 9 μM 1α,25-$(OH)_2D_3$. The chromatograms generated from the wild type are also shown on panels B,D,F and H to facilitate comparisons among the different CYP24A1 proteins under investigation. Triplicate ^{3}H-chromatograms are shown for each condition, however the aqueous phase chromatography is not shown. A quantitative analysis of the chromatography shown in this figure is presented in Table A4.5.

Peak identities:

1: 1α,25-$(OH)_2D_3$
2: 1α,24,25-$(OH)_3D_3$,
3: 24-oxo-1α,25-$(OH)_2D_3$,
4: 24-oxo-1α,23,25-$(OH)_3D_3$
5: tetranor-1α,23-$(OH)_2D_3$
7: 1α,23,25-$(OH)_3D_3$
7a: 23-oxo-1α,25-$(OH)_2D_3$
9: 1α,25-$(OH)_2D_3$-26,23-lactol
10: 1α,25-$(OH)_2D_3$-26,23-lactone.

Figure 4.10: HPLC analysis of the metabolism of 1α,25-$(OH)_2D_3$ by V391L-modified CYP24A1. Stably transfected V79-4 cells containing V391L (A,C,E,G) or V391L/A326G (B,D,F,H) were incubated with 0.3, 1.5, 3.5 and 9 μM 1α,25-$(OH)_2D_3$. The chromatograms generated from the corresponding wild-type controls are shown on each panel, in addition to A326G in panels B,D,F and H to facilitate comparisons among the different CYP24A1 proteins under investigation. Triplicate ^{3}H-chromatograms are shown for each condition, however the aqueous phase chromatography is not shown. A quantitative analysis of the chromatography shown in this figure is presented in Table A4.6. The mutation V391L appeared to shift the regioselectivity of CYP24A1 towards C24-hydroxylation, and could not be completely converted into a C23-hydroxylase by a V391L/A326G double mutant.

Peak identities:

1: 1α,25-$(OH)_2D_3$
2: 1α,24,25-$(OH)_3D_3$,
3: 24-oxo-1α,25-$(OH)_2D_3$,
4: 24-oxo-1α,23,25-$(OH)_3D_3$
5: tetranor-1α,23-$(OH)_2D_3$
7: 1α,23,25-$(OH)_3D_3$
7a: 23-oxo-1α,25-$(OH)_2D_3$
9: 1α,25-$(OH)_2D_3$-26,23-lactol
10: 1α,25-$(OH)_2D_3$-26,23-lactone.

Figure 4.11: HPLC analysis of the metabolism of 1α,25-$(OH)_2D_3$ by M416T-modified CYP24A1. Stably transfected V79-4 cells containing M416T (A,C,E,G) or M416T/A326G (B,D,F,H) were incubated with 0.3, 1.5, 3.5 and 9 μM 1α,25-$(OH)_2D_3$. The chromatograms generated from the corresponding wild-type controls are shown on each panel, in addition to A326G in panels B,D,F and H to facilitate comparisons among the different CYP24A1 proteins under investigation. Triplicate ^{3}H-chromatograms are shown for each condition, however the aqueous phase chromatography is not shown. A quantitative analysis of the chromatography shown in this figure is presented in Table A4.7.

Peak identities:

1: 1α,25-$(OH)_2D_3$
2: 1α,24,25-$(OH)_3D_3$,
3: 24-oxo-1α,25-$(OH)_2D_3$,
4: 24-oxo-1α,23,25-$(OH)_3D_3$
5: tetranor-1α,23-$(OH)_2D_3$
7: 1α,23,25-$(OH)_3D_3$
7a: 23-oxo-1α,25-$(OH)_2D_3$
9: 1α,25-$(OH)_2D_3$-26,23-lactol
10: 1α,25-$(OH)_2D_3$-26,23-lactone.